東京都立大学　博士（理学）学位論文（課程博士）

論 文 名：**$BiCh_2$系層状超伝導体における物性に関する研究**

著　者：星　和久

審査担当者

主　査：水口　佳一　准教授

委　員：青木　勇二　教授

委　員：柳　和宏　教授

上記の論文を合格と判定する

年　　月　　日

東京都立大学大学院理学研究科教授会

研究科長

DISSERTATION FOR A DEGREE OF
DOCTOR OF PHILOSOPHY IN SCIENCE
TOKYO METROPOLITAN UNIVERSITY

TITLE：**Studies of physical properties for $BiCh_2$-based layered superconductors**

AUTHOR: Kazuhisa Hoshi

EXAMINED BY

Examiner in chief: Yoshikazu Mizuguchi

Examiner: Yuji Aoki

Examiner: Kazuhiro Yanagi

QUALIFIED BY THE GRADUATE SCHOOL OF SCIENCE
TOKYO METROPOLITAN UNIVERSITY

Dean

Date

Contents

1. Introduction

1.1. History of superconductivity

Since the discovery of superconductivity for mercury by Onnes, superconductivity studies have been intensively developed for over 100 years [1, 2]. Until the beginning of the 1980s, conventional superconductors, where Cooper pairs are basically formed by the attractive interaction of the electron-phonon interaction, had been central targets for the superconductivity study [3–5]. The superconducting transition temperatures T_c were below 30 K. The superconducting-gap structure for the conventional superconductors is expected to be fully gapped *s*-wave superconductivity. Generally, the fully gapped *s*-wave superconductivity mediated by the electron-phonon coupling is called conventional superconductivity [6]. However, a significant breakthrough occurred in 1986: the discovery of cuprate superconductors by Bednorz and Müller [7]. The T_c for the cuprate superconductors first exceeded the liquid-nitrogen temperature T = 77 K [8]. Thus, the cuprate allows us to open the door to the possibility of the application for superconducting cable. Superconductors that exceed the cuprate's T_c under ambient pressure have not been discovered until Today. The superconducting gap structure of cuprate has been investigated in detail and the momentum-dependent gap structure $d_{x^2-y^2}$-wave state by magnetic (spin) fluctuation is suggested [9]. Such superconductors with the momentum-dependent gap structure are called anisotropic or unconventional superconductors. Furthermore, an interesting normal state: the Mott insulator, which is not a band insulator but an insulating state by the electronic correlation, is realized in the normal states [9]. In 1994, Sr_2RuO_4, which has a similar crystal structure (perovskite) to the cuprate superconductors, was found by Maeno *et al*. [10]. Several studies have suggested that the time-reversal symmetry breaking and the spin-triplet superconductivity can occur in Sr_2RuO_4 and thus intriguing chiral spin-triplet $p_x \pm ip_y$-wave state can be realized [11]. Therefore, Sr_2RuO_4 has been extensively studied until now. Recent experimental work exhibited that the spin-triplet superconductivity is not suitable for Sr_2RuO_4 [12]. In 2001, MgB_2 was found by Nagamatsu and Akimitsu *et al*. [13]. The superconducting pairing mechanism is expected to be conventional superconductivity by the electron-phonon coupling, and the $T_c \approx 39$ K has been the highest in the conventional superconductors under ambient pressure. Moreover, MgB_2 exhibits multigap superconductivity from the multi-orbital nature of the π and σ bunds [14]. In 2008, Kamihara and Hosono *et al*. found a new high-T_c family distinct from the cuprate superconductors: iron-based superconductors [15]. Before the discovery of iron-based superconductors, many researchers considered that the magnetic elements contribute negatively to superconductivity, so the systems give superconductivity researchers a significant impact. The highest T_c has been recorded to be 56 K [16]. The iron-based superconductors have high T_c, but the electronic

states differ from the cuprate. Multi-orbital nature of Fe-3*d* orbitals plays an essential role in the electronic states, but a single orbital of Cu-$d_{x^2-y^2}$ orbital. Normal states are metal or semimetal for iron-based systems but Mott insulators for cuprate superconductors. The superconducting gap structure has not been completely revealed, but the orbital degrees of freedom are essential in superconductivity [17, 18]. In recent studies, iron-chalcogenide compounds are the primary targets, and intriguing phenomena have been observed, such as electronic nematicity, BCS-BES (BCS: Bardeen–Cooper–Schrieffer. BES: Bose-Einstein Condensation) crossover, and topological superconductivity [18]. In 2015, Eremets *et al*. found that sulfur hydride shows superconductivity at T_c = 203 K under extremely high pressure [19]. The significant phonon frequency of hydrogen leads to such high T_c. After the discovery, the studies aiming for room-temperature superconductivity by the hydride and huge pressure have been intensively studied. In 2020, room-temperature superconductivity [T_c = 288 K (~15 C˚)] for carbon-sulfur hydride was reported [20]. However, unfortunately, this article was retracted in September 2022 due to several doubtful data. Thus, humankind has not reached room-temperature superconductivity, although it has been over 100 years since the discovery of superconductivity. I summarize the history of T_c for several superconductors in Fig. 1.1. Except for the above superconductors, there are many intriguing superconductors, such as heavy-fermion superconductors, including 4*f* or 5*f* electrons near the Fermi level [21, 22] and two-dimensional (2D) superconductivity of atomic-layer systems [23]. Furthermore, another way has been paved for the application of superconductors: this is topological superconductivity [24]. Majorana fermion, which can open the possibility of quantum computing, can be realized in topological superconductors.

Theoretical work has fulfilled essential contributions to understanding superconductivity. Especially, BCS theory has played a crucial role [25]. The theory microscopically describes superconductivity as the condensation of Cooper pairs which is basically based on almost all superconductors. The formation of the Cooper pairs can occur in the presence of an attractive interaction (the strength of the interaction is not important). The theory reveals the existence of the superconducting gap as well. Several studies of the isotope effect revealed that the electron-phonon interaction is reasonable for forming the pairs [26, 27]. An isotropic (fully gapped *s*-wave) superconducting gap emerges if the interaction is independent of momentum. Furthermore, the Ginzburg–Landau (GL) theory is helpful for the macroscopic behavior of superconductors, particularly in applying magnetic fields such as the intermediate state in the type-I superconductors and the mixed states in the type-II superconductors [28]. There is spatial inhomogeneity under such magnetic fields; thus, the microscopic theory is unsuitable for describing the state. The GL theory gives us the effective formula of upper critical fields, so call the orbital limit (I introduce this formula in Chapter 3).

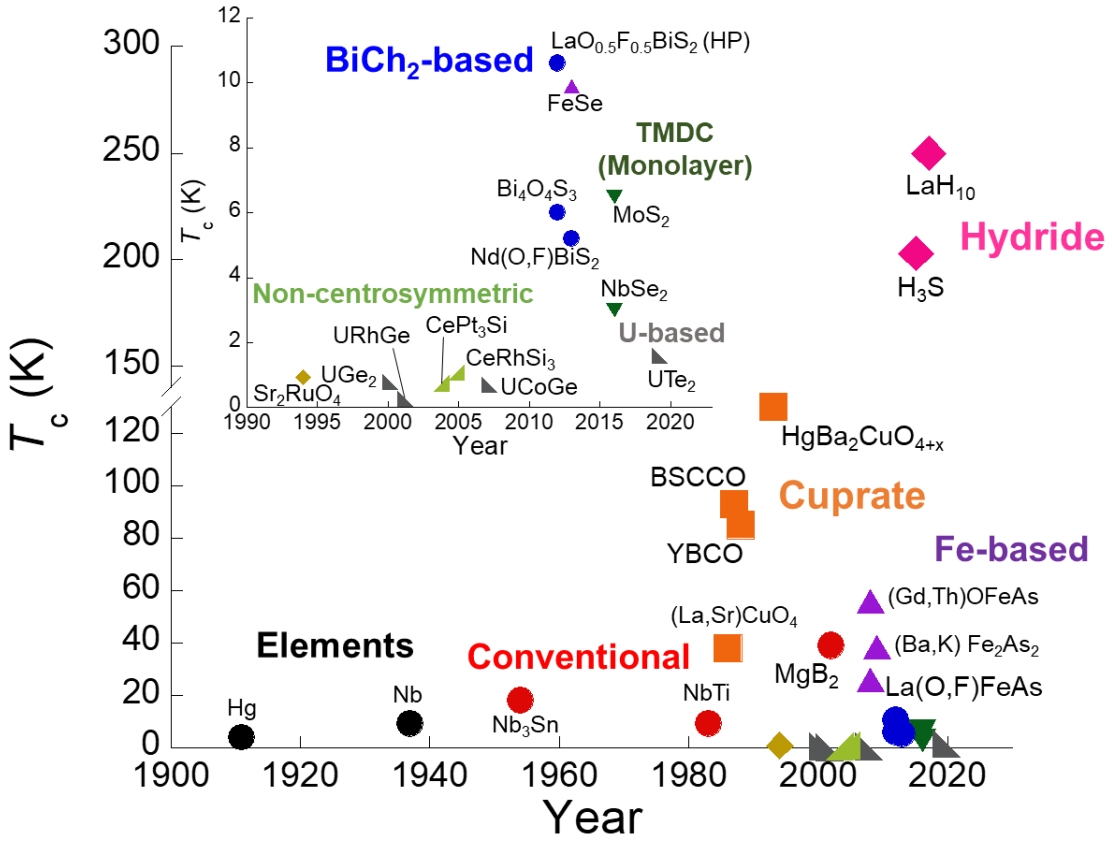

Fig. 1.1. History of superconducting transition temperature T_c for several superconductors. The inset shows the enlarged figure for the low-temperature region. These references for the T_c and year are displayed in 16.4.

1.2. Layered superconductors

Layered superconductors, such as Cuprate, Sr_2RuO_4, MgB_2, and iron-based superconductors, have played significant roles in superconductivity studies because of material variation, relatively high T_c (except for Sr_2RuO_4), and unconventional superconductivity [7, 8, 10, 13, 15, 18]. Figure 1.2 shows the crystal structure of the several layered superconductors. My target materials, $BiCh_2$-based (Ch: S, Se) superconductors, have layered crystal structures composed of the blocking layers and conducting layers as well. I will introduce the $BiCh_2$-based superconductors in the next chapter.

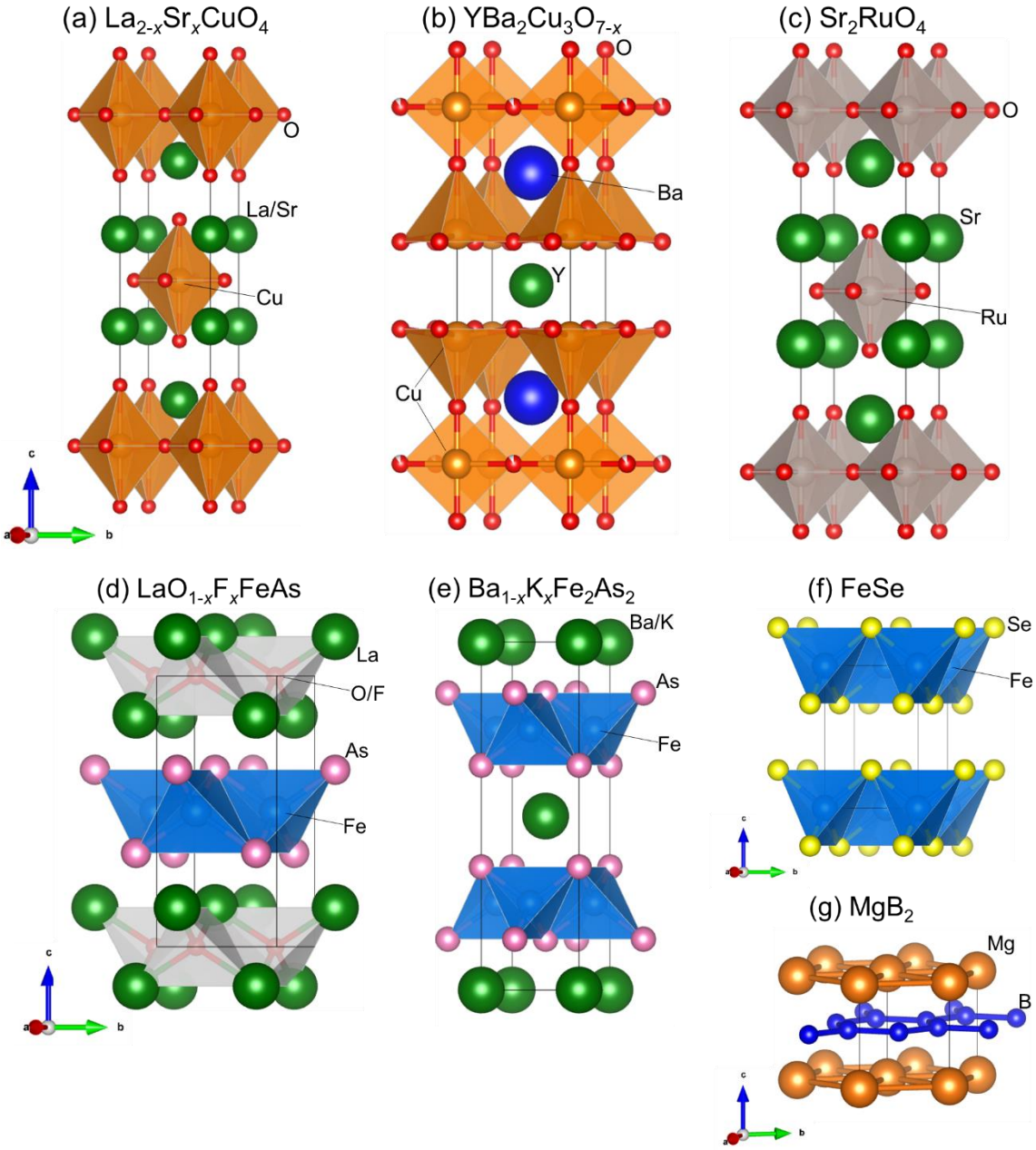

Fig. 1.2. Crystal structure of several layered systems of (a) $La_{2-x}Sr_xCuO_4$, (b) $YBa_2Cu_3O_{7-x}$, (c) Sr_2RuO_4, (d) $LaO_{1-x}F_xFeAs$, (e) $Ba_{1-x}K_xFe_2As_2$, (f) FeSe, and (g) MgB_2. These crystal structures are drawn by VESTA [29].

2. $BiCh_2$-based (Ch = S, Se) superconductors

2.1. Material development

$BiCh_2$-based layered superconductor was discovered by Mizuguchi *et al*. in 2012 and has been extensively studied since the layered structure is similar to that of cuprate and iron-based superconductors [30, 31]. The first $BiCh_2$-based superconductor is $Bi_4O_4S_3$, and the T_c is roughly 6 K [30]. The crystal structure comprises $BiCh_2$ conducting layers and $Bi_4O_4(SO_4)_{0.5}$ blocking layers, and the space group is tetragonal $I4/mmm$ (No. 139, D_{4h}). First-principles calculations show that the conduction band mainly originating from Bi-6p_x/6p_y orbitals cross the Fermi level E_F, which indicates that the Bi orbitals play a significant role in the electronic properties of $Bi_4O_4S_3$ and thus this compound has relatively strong spin-orbit coupling (SOC) [32]. After the discovery of $Bi_4O_4S_3$, the most typical $BiCh_2$-based system was found: (RE/AE)(O/F)$BiCh_2$-type (RE: La, Ce, Pr, Nd, Sm, Gd, Yb and AE: Ca, Sr, Eu) compounds [31, 33]. Figure 2.1(a) shows the typical crystal structure of the (RE/AE)(O/F)$BiCh_2$-type compound, and the space group is tetragonal $P4/nmm$ (No. 129, D_{4h}), which is different from $Bi_4O_4S_3$ while the tetragonal structure is the same. There is much material variation for the (RE/AE)(O/F)$BiCh_2$-type compounds because we can easily perform the elemental substitution. The parent compounds of $REOBiCh_2$ or $AEFBiCh_2$ are band insulators (band gap is below 1 eV), and $LaOBiS_{2-x}Se_x$ or $SrFBiS_{2-x}Se_x$ are monoclinic structures $P2_1/m$ (No. 11, C_{2h}) [34–37]. The substitution of F^- for O^{2-} sites (RE^{3+} for AE^{2+} in the $AEFBiCh_2$-type system) leads to electron-carrier doping, and superconductivity emerges at low temperatures. The carrier-doping way is similar to the iron-pnictide compounds [15]. Moreover, electron-carrier doping in the $BiCh_2$-based system stabilizes the tetragonal structure [38, 39]. The RE sites can be substituted by La, Ce, Pr, Nd, Sm, and Yb and cause the difference in superconducting properties. In particular, Ce has a mixed-valence state of Ce^{3+} and Ce^{4+} and thus may cause self-carrier doping and ferromagnetism due to 4*f* electron [40, 41]. For $EuFBiS_2$, possible charge-density-wave (CDW) formation was observed by transport properties, probably due to the mixed-valence state of Eu^{2+} and Eu^{3+} and 4*f* electron [42]. The possibility of CDW to the $BiCh_2$-based system will be discussed in Section 2.4 and Chapter 9. In addition, we can successfully control from BiS_2-type to BiSSe-type (or $BiSe_2$-type) layers by the Ch-site substitution [37, 43]. The elemental-substitution effects for RE and Ch sites are considered chemical pressure. I will describe the chemical-pressure effect in the next section. The single-crystal-growth method was first found by Nagao *et al*. in 2013 [44]. The single-crystal samples were grown by the high-temperature flux method. Alkali metal chlorides are used as the flux, and those can be easily removed by pure water [45]. The obtained single crystals have plate-like shapes which reflect the tetragonal structure [see Fig. 7.4]. Studies of pairing mechanisms and superconducting-gap structures have been developed using single crystals. I will discuss them in Section 2.3.2. Until now,

I have shown two-layer-type $BiCh_2$-based compounds. At the end of this section, I briefly introduce four-layer- and one-layer-type superconductors, including similar Bi-based layers. Four-layer-type compound $LaOBiPbS_3$ was first discovered by Sun *et al*. in 2014 [46]. The crystal structure is composed of La_2O_2 blocking layers and $BiPbS_3$ conducting layers. We can regard the crystal structure as the rock-salt-type layers are intercalated into Van-der-Waals gaps between $BiCh_2$ bilayer for $REOBiCh_2$-type compounds. $LaOBiPbS_3$ shows semiconductor-like behavior of temperature-dependent resistivity and does not show superconductivity in ambient pressure, although band calculations predicted that the band gap is close to zero. The reason metallic behavior and superconductivity in ambient pressure do not emerge has not been revealed. In contrast, the (Ag,Bi)S-rock-salt-type $La_2O_2Bi_3AgS_6$ exhibits superconductivity at $T_c \approx 0.5$ K in ambient pressure [47]. After discovering $La_2O_2Bi_3AgS_6$, various types of $La_{1-x}RE_xOM_4S_6$ were found, and the maximum T_c is 4.1 K in ambient pressure at the present stage [48]. In addition, applying high-pressure increases the T_c to $T \approx 10$ K for four-layer systems [49]. One-layer-type $Bi_3O_2S_2Cl$ was discovered by Ruan *et al*. in 2019 [50]. The crystal structure consists of alternatively stacking BiS_2Cl conducting layers and BiO blicking layer. Superconductivity emerges at $T_c \approx 3$ K by the sulfur vacancies. There has not been any other report for the one-layer-type compound until now. The layered structures for four-layer-type and one-layer-type compounds are similar to the two-layer-type compounds, but the electronic states differ. Thus, these new-type systems have promising potential. Further investigation using single crystals is necessary for revealing the pairing mechanisms and superconducting-gap structures for four-layer-type and one-layer-type superconductors. Note that I use "$BiCh_2$-based" for the typical two-layer-type system (especially $REOBiCh_2$-type compounds) below.

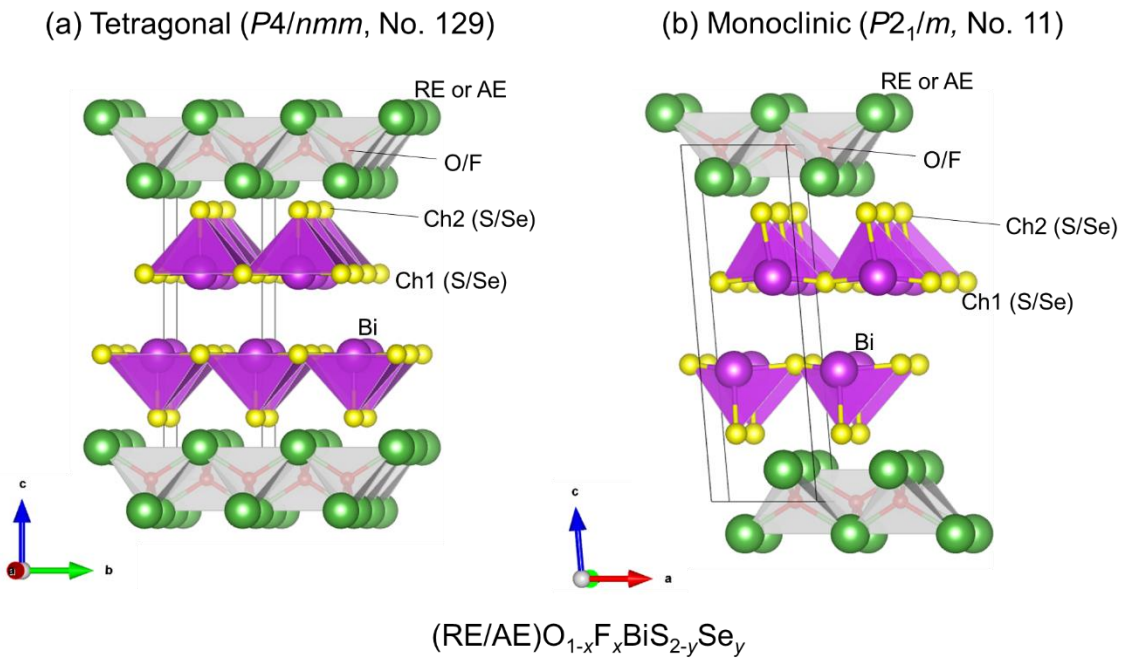

Fig. 2.1. Crystal structures of the $BiCh_2$-based (two-layer-type) compounds for (a) tetragonal *P*4/*nmm*, (No. 129, D_{4h}) and (b) monoclinic $P2_1/m$ (No. 11, C_{2h}) structure. These crystal structures are drawn by VESTA [29].

2.2. Chemical-pressure and high-pressure effect

2.2.1. Chemical-pressure effect

The chemical-pressure effect is significant for enhancing the superconducting properties of $BiCh_2$-based compounds [31]. Chemical pressure basically means that the lattice volume is controlled by isovalent substitution. In the $BiCh_2$-based systems, there are two types of chemical pressure of RE and Ch sites. RE-site substitution with the different ionic radius of RE^{3+} is a powerful tool for applying chemical pressure. The superconducting property is enhanced with decreasing RE^{3+} ionic radius. Bulk superconductivity emerges (shielding volume fraction is roughly 100%) by the substitution of small ionic-radius RE^{3+} while $LaO_{0.5}F_{0.5}BiS_2$ is a filamentary superconducting phase (shielding volume fraction is less than 10%) [51]. Another chemical pressure effect is Se substitution for S sites. Se is selectively substituted at the in-plane Ch1 sites [52]. The Se substitution leads to lattice expansion because of the larger ionic radius of Se than S, which is different from the case of RE substitution. The Se substitution seems to be negative chemical pressure. However, the bonding of the RE(O/F) layer is more robust than that of the $BiCh_2$ layers. Thus, the lattice constant *a* does not largely expand, which causes the chemical pressure effect in the RE(O/F)$BiCh_2$ system. The essence of the chemical

pressure is the suppression of local disorder at the Ch1 sites [37, 53, 54]. Anisotropic atomic displacement parameters U_{ii} are effective for investigating the local disorder. The U_{11} is estimated by Rietveld refinement using synchrotron X-ray diffraction data (RETAN-FP software [55] are often used for the Rietveld refinements). U_{11} for Ch1 sites gradually suppressed with decreasing RE ionic radius and increasing Se concentration, implying that the in-plane local disorder can be diminished with increasing chemical pressure [37, 51]. Moreover, extended X-ray absorption fine structure (EXAFS) reveals that the local distortion within the $BiCh_2$ plane is suppressed by Se substitution for $LaO_{0.5}F_{0.5}BiS_{2-x}Se_x$ [53]. Therefore, the chemical-pressure effect plays a vital role in adjusting the local crystal structure in the $BiCh_2$ plane.

2.2.2. High-pressure effect

The high-pressure effect is essential for improving the superconducting properties of $BiCh_2$-based compounds as well as the chemical-pressure effect. For $LaO_{0.5}F_{0.5}BiS_2$, the T_c steeply increases from $T \approx 3$ K to $T \approx 10$ K around critical pressure $P \approx 0.8$ GPa [56]. The X-ray diffraction under high pressure shows that the T_c jumping accompanies the crystal-structural transition from tetragonal (*P*4/*nmm*, No.129) to monoclinic ($P2_1$/m, No.11) symmetry [56, 57]. Therefore, the quasi-one-dimensional Bi-Ch zigzag chains are probably crucial for the high-T_c phase in the $BiCh_2$-based compounds. The high-T_c (monoclinic) phases under undoped compounds emerge in both high-pressure annealing and applying high pressures. In contrast, F-free $LaOBiCh_2$ also exhibits a monoclinic structure [36, 37]. However, F-substitution leads to a structural transition from monoclinic to tetragonal and stabilizes the tetragonal structure by increasing the F-doing level [38, 39]. Therefore, there is a dilemma in obtaining the high-T_c phases under ambient pressure. If we successfully synthesize optimally F-doped monoclinic compounds under ambient pressure, we will probably realize the high-T_c phase without high-pressure effects.

2.3. Pairing mechanisms of superconductivity and superconducting gap structure

2.3.1. Conventional pairing mechanism and superconducting gap structure

Electron-phonon coupling, a conventional pairing mechanism of superconductivity, is first discussed [32]. McMillan formula helps discuss conventional electron-phonon coupling [58, 59]. This formula is given by

$$T_c = \frac{\omega_{\log}}{1.2} \exp\left[\frac{-1.04(1+\lambda_{SC})}{\lambda_{SC} - \mu^*(1+0.62\lambda_{SC})}\right] \quad (2.1)$$

where λ_{SC} is the electron-phonon coupling constant, $\omega_{\log}$ is the logarithmic frequency average, and

μ^* is the Coulomb coupling constant. Basically, μ^* is approximately estimated to be 0.1 [58, 59]. From theoretical calculations, λ_{SC} is estimated to be 0.5–0.85 for $LaO_{0.5}F_{0.5}BiS_{2-x}Se_x$ (x = 0 and 1), and the ω_{log} is in the order of 100 K [60]. The T_c estimated from the theoretical expectations are same order as the experimentally observed T_c = 2–10 K. The results indicate that the $BiCh_2$-based compounds are conventional phonon-mediated superconductors. In contrast, a theoretical calculation by density-functional theory for superconductors (SCDFT) showed T_c = 0.4 K with λ_{SC} = 0.5 and μ^* = 0.16, which implies that the $BiCh_2$-based superconductors cannot be explained by the electron-phonon coupling [61]. However, this calculation was performed with a tetragonal structure assumed while high-T_c phases ($T_c \approx$ 10 K) are in a monoclinic structure. Therefore, the SCDFT calculation under the monoclinic phase may generate $T_c \approx$ 10 K. We have not concluded whether the pairing mechanism of superconductivity is the conventional electron-phonon coupling or others (e.g., charge/orbital fluctuation and/or spin fluctuation) at the present stage.

The superconducting-gap structure is the most important property for investigating whether one superconductor is conventional fully gaped *s*-wave or unconventional anisotropic [18]. In the former cases, bulk physical quantities associated with low-energy quasiparticle excitations exhibit exponential temperature dependence at low temperatures. In the latter cases, the superconducting gap is dependent on momentum $\boldsymbol{k}$ due to the presence of nodes, and the physical-quantity behavior at low temperatures exhibits the power-law behavior. Therefore, the low-temperature measurements of bulk physical quantities sensitive to low-energy-quasiparticle excitations are necessary for clarifying the superconducting-gap structure. Here, I introduce experimental results which suggest conventional fully-gapped *s*-wave superconductivity: magnetic penetration depth, thermal conductivity, and specific heat measurements [62–65].

First, let me show the magnetic penetration depth measurements. The temperature dependence of the London penetration depth $\lambda\ (T)$, which directly reflects the low-energy-quasiparticle excitations (the number of superconducting electrons), is a bulk probe for revealing pairing symmetry. In fully gapped *s*-wave superconductors, the change of the magnetic penetration depth, $\Delta\lambda\ (T) = \lambda(T) - \lambda(0)$, is exponential temperature dependence at low temperatures. In contrast, $\Delta\lambda\ (T)$ is proportional to T (T^2) at low temperatures in line (point) nodes. For $BiCh_2$-based superconductors, magnetic penetration depth measurements were first performed by tunnel diode oscillator technique for the $Bi_4O_4S_3$ polycrystalline sample by Srivastava and Patnaik [62]. The $\Delta\lambda\ (T)$ at low temperatures shows an exponential temperature dependence, which indicates the fully gaped *s*-wave superconductivity. They estimated the superconducting gap ratio of $2\Delta(0)/k_BT_c$ ~ 6.7 by fitting the data of $\Delta\lambda\ (T)$. This value is much larger than the weak-coupling value of 3.53, which implies that a strong-coupling nature is expected for $Bi_4O_4S_3$. They also estimated the normalized superfluid density. The superfluid density data is in good agreement with a single *s*-wave equation for $2\Delta(0)/k_BT_c$ ~ 7.2, which again indicates the strong-coupling scenario for $Bi_4O_4S_3$. They finally confirmed that a two-gap model, which was

suggested by Muon-spin rotation and relaxation (μSR) measurements (I will introduce the μSR measurements later) [66–68], is not suitable for the explanation of their data and thus concluded that $Bi_4O_4S_3$ is a fully gapped *s*-wave superconductor with the strong coupling. Next, Jiao *et al*. measured magnetic penetration depth using the tunnel diode oscillator for $NdO_{1-x}F_xBiS_2$ single crystals (x = 0.3 and 0.5) [63]. The $\Delta\lambda\ (T)$, after subtracting the paramagnetic contributions of Nd^{3+} ions, also exhibits exponential temperature dependence at low temperatures, which provided evidence of nodeless superconductivity for $NdO_{1-x}F_xBiS_2$. The temperature dependence of the normalized superfluid density further supported the emergence of fully gapped *s*-wave superconductivity. The estimated superconducting gap ratio is $2\Delta(0)/k_BT_c$ ~ 4.3, which is larger than the weak-coupling value but smaller than that of Srivastava *et al.*'s result for $Bi_4O_4S_3$. In summary, these magnetic penetration depth measurements suggested that fully gapped *s*-wave superconductivity with strong coupling is realized in $Bi_4O_4S_3$ and $NdO_{1-x}F_xBiS_2$.

Thermal conductivity (κ) is also a powerful probe for investigating the superconducting gap, which is sensitive to low-energy-quasiparticle excitations. The temperature dependence of κ has the quasiparticle and phonon contributions in superconducting states. The κ/T in the zero-temperature limit presents important information for revealing the superconducting-gap structure. For conventional fully gapped superconductors, κ/T in the zero-temperature limit always vanishes since the phonon term is also zero. In contrast, the presence of nodes in the superconducting gap causes the finite κ/T in the zero-temperature limit, κ_0/T. Magnetic field dependence of κ also provides information on whether a fully gapped or nodal superconductivity is plausible for the superconducting states. In conventional fully gapped *s*-wave superconductors, κ is almost independent of the low magnetic fields and steeply increases near the upper critical field since low-energy-quasiparticle excitations do not exist, and vortex cores are overlapped with increasing magnetic fields. On the other hand, nodal superconductors have delocalized quasiparticles owing to the presence of low-energy quasiparticle excitations. The supercurrent around the vortices induced by magnetic fields affects the quasiparticle energy spectrum by the Doppler-shift mechanism. The Doppler shift leads to an initial increase in low magnetic fields. For $BiCh_2$-based superconductors, Yamashita *et al*. carried out measurements of κ for $NdO_{0.71}F_{0.29}BiS_2$ single crystals [64]. The absence of residual κ_0/T was observed. The low-field $\kappa/T\ (B)$ did not largely change and steeply increased above B^*, which implies the absence of Doppler-shifted quasiparticles. They proposed that B^* is much lower than the upper critical field due to the presence of large gap modulation in the two-dimensional Fermi surface (FS). They finally concluded that $NdO_{0.71}F_{0.29}BiS_2$ is a conventional fully gapped *s*-wave superconductor since the resistivity measurement also indicates that the superconductivity is robust against impurities due to a dirty superconductor.

Heat capacity is the most fundamental thermodynamic quantity that can also examine the low-energy-quasiparticle excitations in superconducting states. The temperature dependence of electronic

specific heat C_e divided by temperature shows exponential dependence in fully gaped superconductors while it shows power-law behavior in nodal superconductors. For $BiCh_2$-based superconductors, it was challenging to discuss the superconducting-gap structure using single crystals due to the relatively lightweight of a single crystal (less than 1 mg) and low electronic specific-heat coefficient γ while the bulk nature of superconductivity by specific heat measurements had been reported in several polycrystalline and single crystal samples. To overcome the situation, Kase *et al*. examined the superconducting gap structure for $LaO_{0.5}F_{0.5}BiSSe$ single crystal with their handmade sensitive calorimeter [65]. The C_e/T (T) data shows exponential temperature dependence at low temperatures, comparable to a fully gapped *s*-wave scenario. They estimated the superconducting gap ratio $2\Delta(0)/k_BT_c$ = 4.5, which implies the strong-coupling nature. Moreover, the ratio of the specific heat jump $\Delta C_e/\gamma T_c$ was obtained to be 2.3. The value supports strong-coupling superconductivity for $LaO_{0.5}F_{0.5}BiSSe$ as well. The field dependence of the specific heat also provides us with necessary information about superconducting-gap structure as well as thermal conductivity. The C_e/T (B) data shows the B-linear dependence on the applied magnetic fields, which indicates fully-gapped superconductivity. In nodal superconductors, C_e/T (B) steeply increases at low fields as proportional to $\sqrt{B}$ dependence. The observed result is clearly distinct from nodal superconductivity behavior. They also confirmed that the multigap nature, as discussed in μSR measurements (I will introduce the next paragraph), was not observed in the specific heat measurements. Therefore, they concluded that $LaO_{0.5}F_{0.5}BiSSe$ is a fully gapped *s*-wave superconductor with strong-coupling nature.

At the end of this section, I briefly introduce μSR measurements. μSR is a unique probe for examining superconducting gap structure and magnetic ordering characteristics. An advantage of μSR measurement is the easiness of experiments on a polycrystalline sample. Zero-field (ZF) μSR has revealed the magnetic-order phase and the possible time-reversal-symmetry-breaking superconductivity in several unconventional superconductors. Transverse-field (TF) μSR provides a way to estimate the magnetic penetration depth (λ), which allows us to investigate the superconducting gap structure. Lamura *et al*. performed ZF- and TF-μSR measurements for the high-pressure (high-pressure-synthesized) phase of $LaO_{0.5}F_{0.5}BiS_2$ with a monoclinic structure [66]. The time dependence of the ZF-μSR was well fitted by a Kubo-Toyabe model, which indicates the presence of small and broad static magnetic fields on the muon site only due to randomly oriented nuclear magnetic dipole moments. Thus, static magnetism of an electronic origin and the indication of time-reversal-symmetry-breaking superconductivity were not detected in the high-pressure phase of $LaO_{0.5}F_{0.5}BiS_2$. TF-μSR measurements were performed by field cooling in the mixed state. They estimated the normalized superfluid density obtained from the magnetic penetration depth and proposed the *s*-wave character with a possible anisotropic gap (but no nodes) for the high-pressure phase of $LaO_{0.5}F_{0.5}BiS_2$. The calculated superconducting ratio is $2\Delta(0)/k_BT_c$ = 3.4–3.7, which is almost consistent with the weak-

coupling value. At almost the same time as Lamura *et al.*'s study, Biswas *et al.* revealed the temperature dependence of the magnetic penetration depth for $Bi_4O_4S_3$ polycrystalline by μSR measurement [67]. The ZF-μSR data ultimately ruled out the presence of any magnetic anomaly in the superconducting state for $Bi_4O_4S_3$ as well as high-pressure-phase $LaO_{0.5}F_{0.5}BiS_2$. The temperature dependence of λ^{-2} obtained from TF-μSR data is more compatible with a two-gap *s*-wave model for $Bi_4O_4S_3$, although a single-gap model cannot be eliminated. They finally concluded the fully gapped superconductivity with possible two gaps for $Bi_4O_4S_3$. Moreover, Zhang *et al.* performed μSR measurements for the polycrystalline of the ambient-pressure-phase $LaO_{0.5}F_{0.5}BiS_2$ [68]. They revealed no signature of magnetic order and the possibility of two-gap superconductivity (*s* + *s*-wave) or anisotropic *s*-wave superconductivity (but no nodes). Therefore, the presence of the nodes was not observed from the three μSR measurements. In contrast, the possible anisotropic superconducting gap (but no nodes) and two-gap superconductivity were indicated for the polycrystalline of the high-pressure- and ambient-pressure-phase $LaO_{0.5}F_{0.5}BiS_2$ and $Bi_4O_4S_3$, respectively. I have introduced the theoretical and experimental results which suggested conventional superconductivity. In the following, I will present the possibility of unconventional superconductivity.

2.3.2. Unconventional pairing mechanism and superconducting gap structure

Several theoretical studies investigated the possibility of unconventional superconductivity originating from the Coulomb repulsions [60]. Usui *et al.* first proposed that the extended *s*-wave and *d*-wave superconductivity can be realized in $BiCh_2$-based superconductors. After this pioneering work, several candidates of unconventional superconductivity, such as $d_{x^2-y^2}$-wave, d_{xy}, and g-wave states have been reported [60, 69, 70]. FS topology is essential for determining superconducting gap structure. In the $REO_{1-x}F_xBiCh_2$-type compounds, electron pockets exist around *X* points up to the doping level $x \approx 0.45$ [71]. With increasing carrier doping, Lifshitz transition occurs around $x \approx 0.45$, and hole pockets emerge around Γ and *M* points [71]. Agatsuma and Hotta suggested that the superconducting gap structure changes from the $d_{x^2-y^2}$-wave to the extended *s*-wave state with the Lifshitz transition [72]. Moreover, Suzuki *et al.* showed that unconventional pairing could be realized by focusing on the orbital degrees of freedom only with an attractive interaction such as the electron-phonon coupling [60]. They considered the Bi-6p_x/6p_y-orbital degrees of freedom in the $BiCh_2$-based system and proposed that the d_{xy}- or extended *s*-wave states as unconventional pairing mechanisms can emerge. In summary, various theoretical calculations have suggested unconventional pairing mechanisms for the $BiCh_2$-based superconductor, although several experimental results indicated the fully gapped *s*-wave state, as discussed in Section 2.3.1. In the following, I will show the experimental results suggesting unconventional superconducting states: anisotropic superconducting gap structure and absent or weak phonon-mediated pairing.

For unconventional superconductors, the superconducting gap is expected to have a dependence on momentum $\boldsymbol{k}$, which sometimes has nodes in a specific $\boldsymbol{k}$ direction. Angle-resolved photoemission spectroscopy (ARPES) is a powerful tool to directly examine the electronic state and superconducting gap structure. The initial ARPES works revealed the basic electronic band structure in the normal states for the $BiCh_2$-based compounds [73]. It was found that FSs for $NdO_{1-x}F_xBiS_2$ are smaller than those expected from the nominal composition, which implies that the actual F concentration (electron-carrier concentration) is lower than the nominal values for the compound [74]. It was challenging to directly observe the superconducting gap for the $BiCh_2$-based superconductors in ambient pressure by ARPES due to relatively low $T_c < 5$ K. However, Ota *et al*. revealed the superconducting gap structure for $NdO_{0.71}F_{0.29}BiS_2$ by a laser ARPES apparatus that achieves the maximum energy resolution of 70 μeV and the lowest temperature of 1.5 K [75]. They found that a strongly anisotropic superconducting gap and the nodelike minima were observed for $NdO_{0.71}F_{0.29}BiS_2$. The result is not contradictory to unconventional superconducting states such as the d- or g-wave scenarios introduced above. Note that in this context, d_{xy}-wave superconductivity is assumed as the d-wave state. The superconducting-gap nodes of the d-and g-wave superconductivity are categorized into symmetry-protected nodes, and the positions of the nodes are strictly decided on the FSs. Thus, such nodes should be detected by the bulk probes. However, several bulk measurements proposed that nodeless superconductivity is realized in $NdO_{1-x}F_xBiS_2$ [63, 64]. A possible way to reconcile the contrary situation is to bring the *s*-wave superconductivity with accidental nodes. When the nodes are not symmetry-protected but accidental, the superconducting gap changes to nodal to nodeless (fully gapped) states by nonmagnetic impurity effect [76]. Such disorder of atomic defects was reported for $NdO_{1-x}F_xBiS_2$ single crystals [77]. Moreover, Ichikawa and Hotta theoretically suggested that the nodes in the nodal *s*-wave state, as discussed in the ARPES, are easily lifted by nonmagnetic impurities [78]. Thus, the bulk measurements, such as magnetic penetration depth and thermal conductivity measurements, may detect the nodeless behavior for the accidental nodes with the disordered crystals. In contrast, if $d_{x^2-y^2}$-wave superconductivity is realized in $NdO_{0.71}F_{0.29}BiS_2$, the disconnected FSs below $x \approx 0.45$ lead to a nodeless state. That is because the nodal lines of the $d_{x^2-y^2}$-wave state are along the $k_x = \pm k_y$ directions and do not cross the FS curves [78]. Thus, we cannot rule out the nodeless $d_{x^2-y^2}$-wave superconductivity if the anisotropic superconducting gaps observed by ARPES are just node-like minima (put differently, the APRES spectra do not imply the presence of the distinct nodes). However, a sign change occurs between the gaps on the disconnected FSs curves if the nodeless $d_{x^2-y^2}$-wave state is realized. Therefore, a nonmagnetic impurity effect by using a high-purity single crystal is necessary to completely determine the superconducting gap structure in the future.

Electron-phonon interaction plays a crucial role in Cooper-pair formation for conventional superconductors [26, 27]. The isotope effect provides us with information on whether the phonon is essential for the Cooper-pair formation of the superconductivity or not. The isotope effect exponent α

is defined as $T_c \propto M^{-\alpha}$, where M is the isotope mass, and $\alpha \approx 0.5$ is expected from the electron-phonon interaction [26, 27]. In many superconductors, α is close to 0.5, which indicates that the electron-phonon interaction is necessary for the pairing mechanisms of the superconductivity. In contrast, a remarkably deviates from 0.5 in unconventional superconductors like copper-oxide and iron-based superconductors [79, 80]. In these superconductors, spin fluctuation and/or orbital/charge fluctuation are suggested as their pairing mechanisms of superconductivity. In the $BiCh_2$-based superconductors, I performed a selenium isotope effect for the polycrystalline sample of $LaO_{0.6}F_{0.4}Bi(S,Se)_2$ using ^{76}Se and ^{80}Se isotopes [81]. The Se substitution leads to in-plane chemical pressure and suppression of local in-plane distortion in $LaO_{0.5}F_{0.5}BiS_{2-y}Se_y$: y = 1.0 can be regarded as a phase with less local distortions in the Bi–Ch plane [37, 53, 54]. In addition, T_c in $LaO_{1-x}F_xBiSSe$ does not remarkably change for x = 0.3–0.5, which implies that T_c is not mainly sensitive to the F concentration [37]. Therefore, $LaO_{0.6}F_{0.4}BiSSe$ is a phase suitable for investigating the isotope effect in the $BiCh_2$-based superconductors. I selected selenium isotopes since Se is included in the conducting $BiCh_2$-layer, and Bi has no stable isotope other than ^{209}Bi. The Se concentration, linked to the T_c, is successfully controlled within y = 1.09–1.14 in $LaO_{0.6}F_{0.4}BiS_{2-y}Se_y$. The T_c of ^{76}Se- and ^{80}Se-containing samples was estimated from magnetization and electrical resistivity measurements. The T_c does not mainly change between ^{76}Se and ^{80}Se, as shown in Fig. 2.2. Thus, the isotope effect exponent α_{Se} is close to zero ($|\alpha_{Se}| < 0.04$), which indicates that the electron-phonon coupling may not be primarily crucial for the Cooper-pair formation of $LaO_{0.6}F_{0.4}Bi(S,Se)_2$. Moreover, Jha and Mizuguchi examined the sulfur isotope effect for tetragonal $Bi_4O_4S_3$ [82]. The space group, *I*4/*mmm* (No. 139, D_{4h}) for $Bi_4O_4S_3$, differs from *P*4/*nmm* (No.129, D_{4h}) for $LaO_{0.6}F_{0.4}Bi(S,Se)$, but it has the same tetragonal structure. The sulfur isotope effect for $Bi_4O_4S_3$ allows us to investigate the influence of both Ch1 and Ch2 sites (see Fig. 2.1) while Se in $LaO_{0.6}F_{0.4}BiSSe$ is almost substituted at the Ch1 sites [52]. The unconventional behavior $|\alpha_S| < 0.1$ was observed for $Bi_4O_4S_3$, implying that the electron-phonon interaction is not primely significant for the compound. Unfortunately, we cannot perform the Bi isotope effect as discussed above. Although the Bi-site phonon may play a crucial role in Cooper-pair formation, at least both Ch1- and Ch2-site phonon does not primarily affect it. A straightforward way to understand the reason for remarkably varying from $\alpha \approx 0.5$ is to consider the substantial contribution of the Coulomb repulsion. Given the possibility of anisotropic gaps by the ARPES study also, we can expect the spin-fluctuation scenario originating from the repulsive Coulomb interaction. However, several bulk measurements indicate that fully gapped *s*-wave superconductivity, i.e., attractive interaction such as electron-phonon coupling, is necessary for the $BiCh_2$-based superconductors. A possible way to reconcile these contradictory results may be to bring the scenario which suggests that the anisotropic superconducting gap structure can emerge by considering the Bi-orbital degrees of freedom only with the attractive interaction [60]. The anisotropic superconducting-gap structure predicted from this scenario is consistent with the ARPES work. The Bi-orbital degrees

of freedom may cause a checkerboard-stripe-type charge ordering (probably CDW) observed by scanning tunneling spectroscopy/microscopy (STM/STS) [77, 90]. Thus, the orbital/charge fluctuation originating from the Bi-orbital degrees of freedom is possibly essential for the pairing mechanism for the $BiCh_2$-based superconductors.

Given these theoretical calculations and experimental results, extended *s*-wave superconductivity with accidental nodes or node-like minima (the point group is A_{1g} even in both cases) by the attractive interaction is reasonable as the superconducting-gap structure and the pairing mechanism for the $BiCh_2$-based superconductors. However, we cannot completely rule out the nodeless $d_{x^2-y^2}$-wave scenario below the doping level of $x \approx 0.45$ because there are disconnected electron pockets around *X* points in the doping level. Furthermore, we cannot conclude that the pairing interaction is electron-phonon interaction or orbital/charge fluctuation at the present stage. The Bi-orbital degrees of freedom are probably significant in any case of phonon-mediated pairing or orbital/charge fluctuation. The non-magnetic impurity effect using high-purity single crystals is adequate to determine the superconducting-gap structure. I hope that studies considering FS topology will be developed in the future. Finally, I summarized these experimental results suggesting both conventional and unconventional superconductivity in Table 2.1.

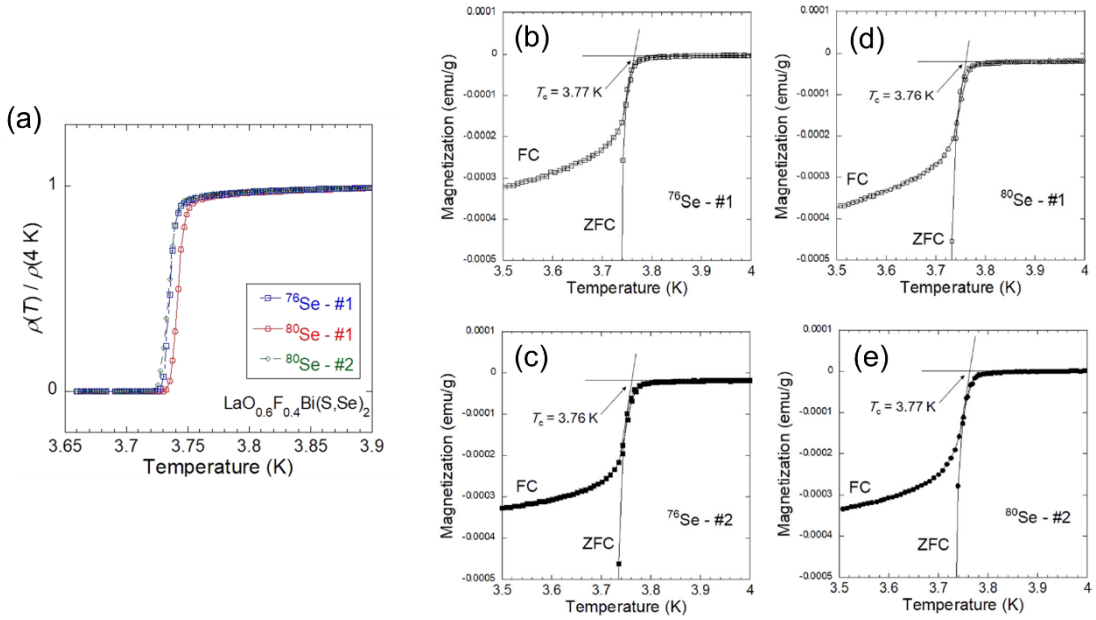

Fig. 2.2. (a) Temperature dependence of the resistivity around superconducting transitions for ^{76}Se- and ^{80}Se-isotope polycrystalline samples. (b)–(e) Temperature dependence of the magnetization for ^{76}Se- and ^{80}Se-isotope polycrystalline samples.

Table 2.1. Summary of experimental results for the superconducting-gap structures and pairing mechanisms for the $BiCh_2$-based superconductors.

Measurement	Compound	T_c (K)	Superconducting gap structure or pairing mechanisms	$2\Delta(0)/k_BT_c$
Magnetic penetration depth [62]	$NdO_{1-x}F_xBiS_2$ (x = 0.3 and 0.5) (Single crystals)	4.4-4.7	Fully gapped s-wave (Strong coupling)	4.3
Magnetic penetration depth [63]	$Bi_4O_4S_3$ (Polycrystalline)	5.3	Fully gapped s-wave (Strong coupling)	7.2
Thermal conductivity [64]	$NdO_{0.71}F_{0.29}BiS_2$ (Single crystals)	5	Fully gapped s-wave	—
Specific heat [65]	$LaO_{0.5}F_{0.5}BiSSe$ (Single crystals)	3.9	Fully gapped s-wave (Strong coupling)	
ARPES [75]	$NdO_{0.71}F_{0.29}BiS_2$ (Single crystals)	5	Anisotropic (Extended s-wave)	—
Isotope effect [81]	$LaO_{0.6}F_{0.4}BiSSe$ (Polycrystalline)	3.7-3.8	Weak phonon contribution	—
Isotope effect [82]	$Bi_4O_4S_3$ (Polycrystalline)	4.7	Weak phonon contribution	—
Isotope effect [158]	$Sr_{1-x}La_xFBiS_2$ (under high pressure) (Polycrystalline)	9.7-10.4	Strong phonon contribution	—
μSR [68]	$LaO_{0.5}F_{0.5}BiS_2$ (Polycrystalline)	2.9	Two-gap (s+s-wave) or anisotropic s-wave	$2\Delta_1(0)/k_BT_c = 7.6$ and $2\Delta_2(0)/k_BT_c = 1.8$ for two-gap case $2\Delta_{an}(0)/k_BT_c = 4.2$ for anisotropic case
μSR [66]	$LaO_{0.5}F_{0.5}BiS_2$ (under high pressure) (Polycrystalline)	10	Fully gapped s-wave or anisotropic s-wave	$2\Delta_{iso}(0)/k_BT_c = 3.4$ for isotropic case $2\Delta_{an}(0)/k_BT_c = 3.7$ for anisotropic case
μSR [67]	$Bi_4O_4S_3$ (Polycrystalline)	4.8	Two-gap (s+s-wave)	$2\Delta_1(0)/k_BT_c = 4.7$ and $2\Delta_2(0)/k_BT_c = 0.4$ for two-gap case
STM/STS [84]	$NdO_{0.5}F_{0.5}BiS_2$ (Single crystals)	4.8 (T^* = 20 K)	Two-gap (superconducting gap and another gap)	$2\Delta_{Tc=4.8}(0)/k_BT_c = 16.8$ $2\Delta_{Tc=20}(0)/k_BT_c = 4.06$

2.4. Possible exotic superconducting states

At the end of Chapter 2, I briefly introduce other exotic states: superconducting fluctuation (strong coupling), multiorbital-electronic states (multi-gap superconductivity), CDW, and quantum critical point (QCP). First, I show the possibility of superconducting fluctuation and strong coupling. It is known that superconductivity can survive even above T_c as thermal fluctuation. The superconducting fluctuations basically emerge just above T_c and are well understood in terms of the standard Gaussian fluctuation theorem. However, high-temperature superconductor cuprate is expected to have strong superconducting fluctuations due to strikingly high T_c, and the effect is closely related to the pseudogap formation [9]. In iron-selenide superconductors, giant superconducting fluctuations were observed and are obviously distinct from conventional superconductors [83]. The pseudogap formation is expected to be related to the BCS-BEC crossover [18, 83]. In $BiCh_2$-based superconductors, Liu *et al*. observed giant superconducting fluctuation far above T_c for $NdO_{0.5}F_{0.5}BiS_2$ [84]. A reduction in normal-state resistivity (T^* ~ 20 K) above the superconducting transition (T_c = 4.8 K) was observed, which is an indication of superconducting fluctuation. The Nernst effect and STM results support the superconducting-fluctuation scenario. Furthermore, similar behavior of the reduction above superconducting transition was observed in $Bi_4O_4S_3$ polycrystalline [85]. Liu *et al*. also found the two-gap nature by STM and the smaller gap, which is related to the superconducting transition, shows the extremely high gap ratio $2\Delta(0)/k_BT_c$ ~ 17 under T_c = 4.8 K observed by resistivity measurements. The ratios observed from magnetic penetration depth, specific heat, and μSR measurements are also large values, while these are much smaller than 17. Therefore, I believe that the strong-coupling

scenario is plausible for $BiCh_2$-based superconductors, while I cannot determine how strong the coupling is.

Hall resistivity measurements detected multiband-like behavior for several polycrystalline samples [40, 86, 87]. Field dependence of the Hall resistivity shows nonlinear behavior in a magnetic field, although a single-band system exhibits *B*-linear dependence. Under multi-band systems, multi-gap superconducting states can be realized, such as MgB_2 and iron-based superconductors [14, 18]. Indeed, the magnetic penetration depth estimated from μSR measurements indicated the multi-gap superconductivity for polycrystalline samples of $Bi_4O_4S_3$ and $LaO_{0.5}F_{0.5}BiS_2$ under ambient pressure [67, 68]. Moreover, the temperature dependence of the in-plane upper critical fields for single crystal samples of $LaO_{0.5}F_{0.5}BiS_2$ was well-fitted by the two-gap model [155]. These results exhibit that the multi-gap scenario is reasonable for the $BiCh_2$-based superconductors. However, a simple question is whether the multi-gap superconductor can really emerge even in relatively simple FS topology for the $BiCh_2$-based compounds compared with the iron-based and MgB_2 superconductors. The FSs are mainly composed of the Fe-d_{xy}, d_{xz}, and d_{yz} orbitals for the iron-based compounds and of the σ and π bands for MgB_2, respectively [14, 18]. In contrast, the FSs for the $BiCh_2$-based systems mainly consist of the Bi-p_x and p_y orbitals and these orbitals should degenerate in the tetragonal phase. If the multi-gap superconductivity was observed in monoclinic phases [high-pressure applying (or high-pressure-annealing/synthesized) or much-poor F-doped samples], the scenario would be compelling. However, the multi-gap nature was reported in the tetragonal phase synthesized under ambient pressure and optimal F-doped regions. Therefore, it does not seem easy to realize the multi-gap superconductivity in $BiCh_2$-based systems. In addition, the polycrystalline samples were used in the Hall resistivity and μSR measurements, suggesting the multi-band nature. $BiCh_2$-based compounds have quasi-two-dimensional electronic states and large electronic anisotropy between the *ab* plane and *c* axis [44, 45]. Indeed, single-band nature has been observed in our single crystals (see Chapter 9). Of course, I do not try to rule out the two-gap scenario for the $BiCh_2$-based compounds, but we need to use single crystals to investigate the physical properties in detail. Possibly, the local monoclinic distortion can lead to lifting the degeneracy of the Bi-6p_x and 6p_y orbitals and may generate a multi-band nature.

The existence of the CDW phase was predicted by theoretical calculations from the early stage [60, 88, 89]. FS nesting at the wave vector (π, π) expected in $x = 0.5$ can lead to the one-dimensional CDW nature along the in-plane Bi-Bi directions. The STM/STS studies for $NdO_{0.7}F_{0.3}BiS_2$ and $LaO_{0.5}F_{0.5}BiSe_2$ directly observed the checkerboard stripe along the Bi-Bi directions, which indicates the CDW formation [77, 90]. Moreover, recent X-ray diffraction studies using single-crystal samples suggested the presence of CDW phases for $NdO_{0.7}F_{0.3}BiS_2$ and $LaO_{0.5}F_{0.5}BiS_2$ [91, 92]. The CDW formations occur in $T \approx 120$ K and $T \approx 260$ K for $NdO_{0.7}F_{0.3}BiS_2$ and $LaO_{0.5}F_{0.5}BiS_2$, respectively. Furthermore, the Supplemental Materials in Ref. 92 showed a possible signature of the CDW from the

temperature dependence of the electrical resistivity and magnetic susceptibility. In addition, transport properties for a polycrystalline sample of $EuFBiS_2$ indicated that the CDW transition occurred around $T \approx 280$ K, at which the anomaly of electrical resistivity and Hall coefficient was observed [93]. These results give us solid evidence of CDW formation. In future work, I expect the relationship between the CDW and superconductivity will be clear. I will discuss that the CDW phases may exist for $LaO_{1-x}F_xBiS_{2-y}Se_y$, and the states can be suppressed by Se substitution in Chapter 9.

Higashinaka *et al*. investigated transport properties for $CeOBiS_2$ and suggested the possibility of a quantum critical point (QCP) [94]. The -log T divergence of the specific heat was observed at low temperatures in zero field, which indicates the existence of quantum critical fluctuations of 4*f* magnetic moments near a QCP. Furthermore, the -log T divergence of the specific heat was basically reported in numerous *f*-electron-based strongly correlated electron systems. To realize a QCP in the *f*-electron-based compounds, we need to adjust the balance between Kondo and Ruderman-Kittel-Kasuya-Yoshida (RKKY) interactions by chemical doping and pressure. However, the temperature dependence of the *ab*-plane electrical resistivity for $CeOBiS_2$ showed semiconducting behavior, which implies that the Kondo effect cannot be realized since it is the interaction between conduction electrons and *f* electrons in the *f*-electron-based systems. Finally, they proposed that non-doped $CeOBiS_2$ is positioned at an unconventional QCP among geometrically frustrated nonmetallic magnets. Although they observed no superconductivity for $CeOBiS_2$ up to $T \approx 2$ K, other gropes exhibited zero resistivity around $T \approx 1.2$ K for the same composition [41], which may support the QCP scenario since superconductivity has often been observed near a QCP [17]. As described above, the mother compound $REOBiS_2$ is a band insulator; hence, carrier-doping is necessary for obtaining the superconducting phase. Therefore, the fact that superconductivity emerges in $CeOBiS_2$ gives us the possibility of the mixed-valence state between Ce^{3+} and Ce^{4+}. The remaining questions are how the mixed-valence state is associated with the QCP-like behavior for $CeOBiS_2$ and whether this state can tune by applying pressure or isovalent-elemental substitution (without F substitution).

3. Local inversion symmetry breaking

3.1. Non-centrosymmetric superconductors

Non-centrosymmetric superconductors have been extensively studied where the crystal structure lacks the inversion center [95, 96]. In these superconductors, antisymmetric spin-orbit interaction (SOI) plays a significant role in the superconducting properties. Rashba-type SOC (RSOC), where a lack of a mirror plane perpendicular to the *c* axis removes inversion symmetry, such as the C_{4v} point group, is one of the most typical antisymmetric SOC. The SOI by the antisymmetric SOC can lead to lifting the spin degeneracy, i.e., a spin-split state can emerge by the inversion symmetry breaking. This state can cause profound consequences on the superconducting properties, such as the mixture of spin-singlet and spin-triplet components, huge upper critical fields due to the suppression of the paramagnetic pair-breaking effect, Helical phase parallel to the plane, and topological superconductivity [95, 96]. Furthermore, in respect of superconducting gap structures, the singlet-triplet mixing can cause the superconducting-gap nodes, which are not symmetry-protected (Of course, this should be called unconventional superconductivity). This section briefly introduces several non-centrosymmetric superconductors, mainly focusing on the upper critical fields. In this paper, I basically consider the Rashba-type SOI (RSOI) as the antisymmetric spin-orbit interaction.

Before cutting to the chase to introduce the non-centrosymmetric superconductors, I explain two distinct pair-breaking effects for Cooper pairs under magnetic fields: the paramagnetic pair-breaking effect and the orbital pair-breaking effect. The former mechanism originates from spin polarization due to the Zeeman effect, which competes with the antiparallel-spin formation of the Cooper pairs in the spin-singlet superconductor. Therefore, the paramagnetic pair-breaking effect is significant in the spin-singlet superconductivity. The limiting field by the paramagnetic pair-breaking effect can be evaluated by comparing the superconducting condensation energy with the Zeeman energy. The paramagnetic pair-breaking limiting field B_{p} is given as

$$B_{\mathrm{p}} = \frac{\sqrt{2}\Delta(0)}{g\mu_B\sqrt{1-\frac{\chi_s}{\chi_n}}}, \tag{3.1}$$

where $\Delta(0)$ is the superconducting gap at zero temperature, g is g-factor, μ_B is the Bohr magneton, and χ is the spin susceptibility (χ_s exhibits superconducting states and χ_n normal states). If we assume g = 2 for free electrons and the spin-singlet superconductivity with weak-coupling value $\Delta(0) = 1.76k_BT_c$, where k_B is the Boltzmann constant, we can find the well-known formula

$$B_{\mathrm{p}} = 1.86\,T_c \tag{3.2}$$

since χ_s disappears at zero temperature. This limiting field is the so-called Pauli-Clogston-Chandrasekhar limit or simply the Pauli limit. When the Cooper pairs comprise parallel spins, i.e., the spin-triplet superconductivity, the paramagnetic pair-breaking effect depends on the directions of the

d vector, which is generally used to describe the spin-triplet superconductivity. The paramagnetic pair-breaking effect is significant when the magnetic field is parallel to the ***d*** vector (Eq. 3.2 is valid). On the other hand, the paramagnetic pair-breaking effect is absent when the magnetic field is perpendicular to the ***d*** vector [χ_s do not affect by superconducting transition ($\chi_s = \chi_n$) and thus Eq. 3.1 yields $B_p \to \infty$). Hence, the paramagnetic pair-breaking effect depends on the pairing symmetry of the Cooper pairs.

In non-centrosymmetric superconductors, the paramagnetic pair-breaking effect is either absent or depressed by the magnetic field directions. For non-centrosymmetric superconductors, the spin degeneracy is lifted even in a zero field. Put differently, spin-band splitting can occur. By RSOI, the spins are aligned along the in-plane direction, and the spin direction depends on the momentum ***k***. The paramagnetic pair-breaking effect occurs only in magnetic fields parallel to the spin directions. Thus, the paramagnetic pair-breaking effect is partial along the *ab*-plane magnetic fields and is absent along the *c*-axis magnetic fields since all spin directions are aligned along the *ab*-plane. Strictly speaking, the behavior of the paramagnetic pair-breaking effect for non-centrosymmetric superconductors originates from Van-Vleck susceptibility. The Van-Vleck susceptibility arises from the interband hopping, while the intraband contribution gives rise to the Pauli susceptibility. The superconducting transition hardly affects the Van-Vleck susceptibility when the band splitting owing to the antisymmetric SOI is much larger than the superconducting gap. On the other hand, Pauli susceptibility for the spin-singlet superconductor is suppressed by the superconducting transition, and the value disappears at zero temperature, as described above. For the Rashba-type superconductors, the in-plane susceptibility is determined by both Pauli and Van-Veleck contributions, while the out-of-plane susceptibility is determined only by the Van-Vleck contribution. Therefore, the paramagnetic pair-breaking effect is absent along the out-of-plane directions, although partial along the in-plane direction.

Next, I introduce the orbital pair-breaking effect. The orbital pair-breaking effect can be written as

$$B_{\mathrm{orb}}(T) = \frac{\Phi_0}{2\pi\xi^2(T)}, \tag{3.3}$$

where the Φ_0 is the flux quantum, and the ξ is the GL coherence length. Small coherence length leads to large upper critical fields. There is the following relationship among the GL coherence length, Pippard coherence length ξ_0, and mean free path ℓ

$$\frac{1}{\xi} = \frac{1}{\xi_0} + \frac{1}{\ell}. \tag{3.4}$$

In clean superconductors ($\ell \gg \xi_0$), the GL coherence length is comparable to the Pippard coherence length $\xi_0 = 0.18\hbar v_F/k_B T_c$ where the $\hbar$ is Plank constant and v_F is Fermi velocity. Fermi velocity is inversely proportional to the effective mass ($v_F = \hbar k_F/m^*$ where k_F is Fermi wave number and m^* is effective mass). Thus, the conference length is essentially small in heavy fermion systems, and thus

the orbital limit is greatly enhanced. Furthermore, the Werthamer–Helfand–Hohenberg (WHH) model is familiar as the fitting function for the orbital pair-breaking effect [97, 98]. The WHH model can be described as

$$B_{\mathrm{orb}}(0) = -AT_c \left.\frac{dB_{c2}(0)}{dT}\right|_{T=T_c}, \tag{3.5}$$

where the A is 0.73 in the clean limit and 0.69 in the dirty limit. The initial slope of B_{c2} (T) is significant in the orbital limit (Indeed, GL theory is suitable for temperatures close to T_c). The orbital pair-breaking effect is independent of the pairing symmetry of the Cooper pairs.

$CePt_3Si$ is the first non-centrosymmetric heavy fermion superconductor [99]. The space group is tetragonal $P4mm$ (No. 99, C_{4v}), where the inversion symmetry is broken along the c-axis direction, leading to RSOC [95, 96]. Unconventional superconducting states, i.e., the presence of superconducting-gap nodes, were observed by several bulk measurements, such as magnetic penetration depth, thermal conductivity, and specific heat measurements. The observed upper critical fields vastly exceed the Pauli-paramagnetic limiting field, and the Knight shift remains constant below T_c for all crystallographic directions of the magnetic fields. These results indicate the significance of the RSOI. However, the anisotropy of the upper critical fields between the ab plane and c axis is small, and the upper critical fields for both directions exceed the Pauli limit. If the RSOI is essential for the superconducting state, the upper critical field should be significantly enhanced only along the c-axis direction. Consequently, the constant Knight shift should also be observed in this direction. Thus, given the difficulties of synthesizing high-quality single crystals as well, it is a challenging task to ultimately determine the pairing mechanisms and superconducting gap structures.

Next, CeTX_3-type (T = transition metal, X = Si or Ge) compounds are also attractive non-centrosymmetric superconductors [95, 96, 100]. In this system, superconductivity is indeed by applying high pressure. The space group in the CeTX_3 is $I4mm$ tetragonal (No. 107, C_{4v}). A remarkable feature in the CeTX_3 superconductors is the extremely high c-axis B_{c2} (T) and the large anisotropy, distinct from the weak anisotropy of $CePt_3Si$. For example, B_{c2} (0) for $CeRhSi_3$ exceeds 30 T along the c axis even though the T_c is in the order of 1 K, which strongly indicates that RSOI plays a significant role in the superconducting properties. The high B_{c2} (T) in the c-axis direction and large anisotropy contribute to the anisotropic paramagnetic pair-breaking effect by RSOI. That is because the orbital limit is also primarily enhanced in the heavy-Fermion electronic states, and thus the upper critical fields can be limited by the paramagnetic pair-breaking effect. Indeed, the much sizeable initial slope of the B_{c2} (T) was observed in the CeTX_3 compounds. Therefore, the $B_{c2}(T)/T_c$ is remarkably high in all superconductors (see Fig. 3.1) because of the suppression of both paramagnetic pair-breaking and orbital pair-breaking effects.

Finally, I introduce 2D superconductors transition metal dichalcogenides such as monolayer $NbSe_2$ and MoS_2 [23, 101, 102]. The inversion symmetry is broken in the surface; thus, RSOC exists in this

system. For these systems, the in-plane B_{c2} (T) is strikingly enhanced, but the out-of-plane is much smaller than the plane. Considering the RSOC, explaining the huge in-plane B_{c2} (T) may be challenging. However, there is another critical feature in the monolayers for MoS_2 and $NbSe_2$: in-plane inversion symmetry is broken. This symmetry breaking can cause *c*-axis-direction spin splitting, so-called Zeeman-type spin polarization, which is different from the Rashba-type spin polarization (*ab*-plane-direction spin splitting). The singlet Cooper pairs under this spin texture can be locked along the out-of-plane direction and protected against the in-plane magnetic field. Such Cooper-pair formation is called Ising pairing. Therefore, the in-plane paramagnetic pair-breaking effect is primarily suppressed in these systems. The orbital limit should also be enhanced to observe the highly high in-plane B_{c2} (T). For the layered superconductors, the B_{c2} (T) and the coherence length have the anisotropy between the in-plane and the out-of-plane direction. Thus, the following formula gives the B_{c2} (T) for layered superconductors [28],

$$B_{\mathrm{orb}}^{\parallel}(T) = \frac{\Phi_0}{2\pi\xi_{\parallel}(0)\xi_{\perp}(0)}\left(1-\frac{T}{T_c}\right), \tag{3.6}$$

$$B_{\mathrm{orb}}^{\perp}(T) = \frac{\Phi_0}{2\pi{\xi_{\parallel}}^2(0)}\left(1-\frac{T}{T_c}\right). \tag{3.7}$$

$\xi_{\parallel}$ and $\xi_{\perp}$ are in-plane and out-of-plane coherence lengths, respectively. Therefore, the out-of-plane coherence length becomes short when the electronic states have a quasi-two-dimensional nature (superconducting anisotropy is large). Furthermore, when the effective thickness of superconductivity d_{SC} is smaller than the out-of-plane coherence length, such as 2D systems, the in-plane B_{c2} (T) is written as

$$B_{\mathrm{orb}}^{\parallel}(T) = \frac{\Phi_0\sqrt{12}}{2\pi\xi_{\parallel}d_{SC}}\sqrt{1-\frac{T}{T_c}}. \tag{3.8}$$

Under this condition, the orbital pair-breaking effect is largely suppressed. In order to show solid evidence that 2D superconductivity is realized, the angular dependence of the upper critical fields should be comparable to the 2D Tinkham model (see Chapter 10). Indeed, the angular variations of the B_{c2} (T) for the monolayers of $NbSe_2$ and MoS_2 are well-fitted by the 2D Tinkham model. Because of the suppression of both orbital pair-breaking and paramagnetic pair-breaking effects, the in-plane B_{c2} (T) is largely enhanced for these monolayers. As introduced so far, high upper critical fields have been observed in non-centrosymmetric superconductors due to the presence of antisymmetric SOC (Rashba-type SOC and Zeeman-type SOC). On the other hand, local inversion symmetry breaking leads to significant contributions of superconductivity attributed to a staggered ASOC, even in centrosymmetric systems. In the following, I will introduce how the local inversion symmetry breaking affects superconductivity with respect to theoretical (Section 3.2) and experimental (Section 3.3) studies.

At the end of this section, I show the upper critical fields for several superconductors (see Fig. 3.1).

Uranium compounds and non-centrosymmetric heavy-fermion compounds can exhibit huge upper critical fields due to the suppression of both paramagnetic and orbital pair-breaking effect (For several uranium compounds, the paramagnetic pair-breaking effect is absent due to the spin-triplet pairing). Therefore, we need to focus on the crystal structure, electronic band structure (the kind of orbitals near the Fermi level), and pairing symmetry to realize high upper critical fields despite low T_c. In addition, recently discovered $CeRh_2As_2$ with locally non-centrosymmetric crystal structure, which is the same crystal structure as my target material $BiCh_2$-based superconductors, also shows high upper critical fields. In the next section, I will introduce the locally non-centrosymmetric systems.

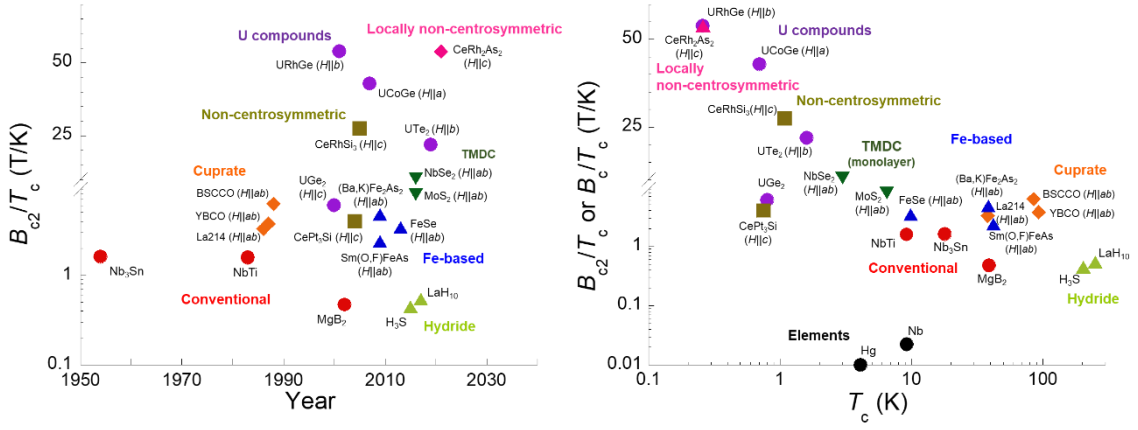

Fig. 3.1 (a) History of upper critical fields divided by superconducting transition temperatures T_c for several superconductors. (b) T_c dependence of upper critical fields or critical fields divided by T_c for several superconductors. These references of the upper critical fields, critical fields, T_c, and year are displayed in 16.4.

3.2. Local inversion symmetry breaking and superconductivity: theoretical aspect

As introduced in Section 3.1, non-centrosymmetric superconductors show intriguing superconducting properties, especially extremely high upper critical fields, and have been a central research topic for a long time. Recently, several theoretical studies suggested that the local inversion symmetry breaking in the sublattice structure can cause interesting physical properties even when global inversion symmetry is possessed (centrosymmetric systems) [103, 104]. All symmetry-distinct sites in the unit cell, captured by the concept of Wycko positions, have their symmetry group, the so-called site symmetry group. The site symmetry group is a subgroup of the bulk point group with transformations that leave the specific site invariant. Consequently, we can build a sublattice from such sites with lower symmetry so that this sublattice lacks symmetries of the whole crystal structure, such as inversion. When a crystal structure is composed of two sublattices that lack inversion symmetry, but the point group of the crystal contains inversion symmetry (which exchanges the

sublattices), we call such crystal structures locally non-centrosymmetric systems [104]. There are several examples of locally noncentrosymmetric crystal structures. The most typical cases are layered structures, in which each layer lacks the mirror plane perpendicular to the *c* axis, but the layers are connected by interlayer coupling so that global inversion symmetry is possessed. In such layered structures, the staggered RSOC can exist in each layer. Because my target materials, $BiCh_2$-based superconductors, have a layered structure, I consider the RSOI contribution below. The studies using thin films are familiar with the locally non-centrosymmetric systems. Artificial superlattices of heavy-fermion multilayers [105–107] and bilayer (and trilayer) systems [108, 109] have been studied as the layered structure with local inversion symmetry breaking. In bulk systems, the crystal structure of the recently discovered $CeRh_2As_2$ superconductor has tetragonal $P4/nmm$ (No. 129, D_{4h}), and the Ce site lacks the inversion symmetry with the C_{4v} site point group [110]. The experimental results for these systems are introduced in the next section. My target compounds $LaO_{1-x}F_xBiS_{2-y}Se_y$ also belong to the space group $P4/nmm$ (No. 129, D_{4h}), the Bi and Ch sites lack the inversion symmetry with the C_{4v} site point group, and I describe the physical properties in detail later. Note that the F-free compounds $LaOBiS_{2-y}Se_y$ have monoclinic structures [36, 37, 39], but F substitution (electron-carrier doping) leads to the stabilization of the tetragonal structure [38, 39, and Chapter 8]. In these layered structures, the staggered RSOC dependent on each layer can emerge and lead to spin polarization. If we assume a bilayer system, the sign of the RSOC is inverse between the layers. In non-centrosymmetric superconductors, mixed-parity pairing can occur in the superconducting states. Locally non-centrosymmetric superconductors can also emerge in the mixed-parity states similar to the glocal inversion symmetry breaking. In the locally non-centrosymmetric case, the superconducting order parameters largely depend on each layer owing to the staggered RSOC. The relative amplitude of the RSOC and the interlayer coupling (hopping) between the sublattice is essential for the local inversion symmetry breaking to play an important role in the electronic states. A crossover from conventional superconductivity to non-centrosymmetric (global inversion symmetry breaking) superconductivity can be realized by controlling the ratio of the RSOC to the interlayer hopping. The spin susceptibility in the superconducting states, which is significant in the non-centrosymmetric systems, depends on the relative strength of RSOC and interlayer coupling. The spin susceptibility does not disappear at zero temperature, even with spin-singlet states predominant when the RSOC contribution is significant. The spin susceptibility is close to the spin-triplet case by increasing the RSOC term even in the predominant spin-singlet states. This non-zero spin susceptibility can lead to the depression of the paramagnetic pair-breaking effect. This layer-dependent RSOC causes exotic superconducting states under magnetic fields. I introduce the two distinct cases: (I) Pair-density wave (PDW) in magnetic fields parallel to the out-of-plane direction and (II) Complex stripe (CS) phase to Helical phase in magnetic fields perpendicular to the out-of-plane direction. I briefly summarize the two phases below.

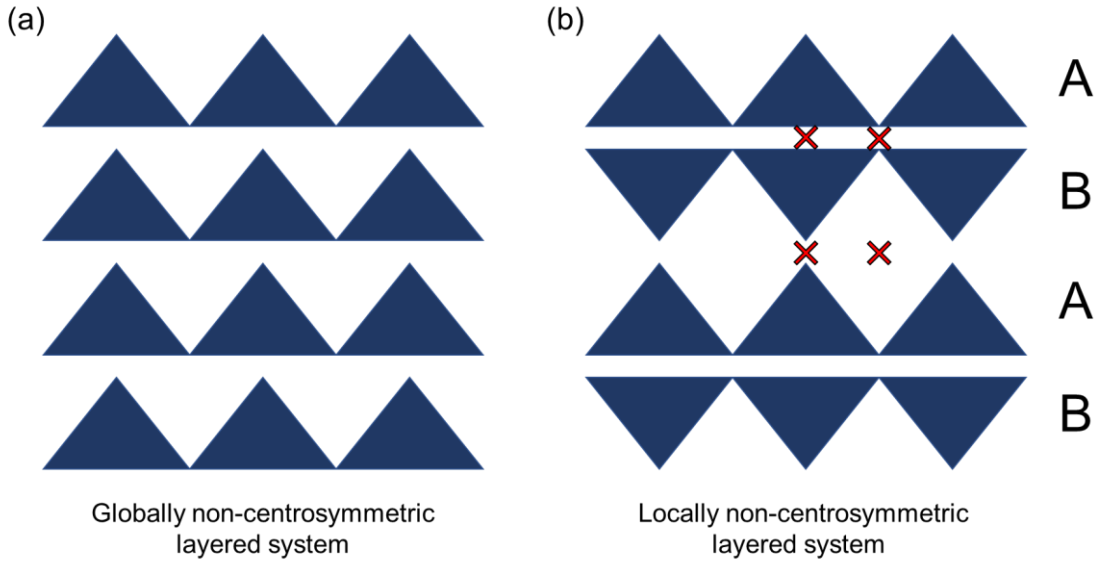

Fig. 3.2. Schematic images of (a) globally and (b) locally (staggered) non-centrosymmetric systems as the example of the layered structure. The red crosses in (b) represent the global inversion centers. Two sublattices (structures) of A and B in (b) lack inversion symmetry, while the global inversion symmetry is possessed with the inversion centers.

(I). Pair-density wave (PDW) state in magnetic fields parallel to the *c* axis [103, 111]

We consider a pure spin-singlet (or spin-singlet state is predominant) bilayer system, where the individual layer lacks local inversion symmetry, and the applied magnetic field is parallel to the *c* axis. The sign of the RSOC is inverse between the bilayer. In the zero-magnetic field, the superconducting order parameter is the same in both layers (uniform superconducting parameter is realized in both layers). In low-field regions, superconductivity is suppressed against the applied magnetic field owing to the paramagnetic pair-breaking effect. This state from zero-field to low-field regions is called the BCS state compared with the PDW state (the interlayer coupling can realize the uniform BCS state). Interestingly, with further increasing magnetic fields, the superconducting order-parameter changes between the layers (see Fig. 3.3). This state is called the PDW state because the order parameter modulates on the length scales of the crystal lattice. The stability of the PDW can be understood by considering the spin susceptibility [112]. When the RSOC contribution is stronger than interlayer coupling, the Cooper pairs for both BCS and PDW states can form in the intraband. The PDW state is more robust against the paramagnetic pair-breaking effect than the BCS state since Van-Vleck susceptibility, which is predominant in the susceptibility for the PDW state, originates from the interband contribution and is hardly affected by the superconducting transition. Note that the spin-band splitting by RSOI and interlayer coupling contributions gives rise to Van-Vleck susceptibility, which is much larger than the superconducting gap. However, the BCS state is stabilized by the

interlayer coupling in the zero-field and low-filed regions. Therefore, the phase transition from the BCS to the PDW state can occur by applying magnetic fields. The paramagnetic pair-breaking effect must be dominant to observe the PDW state. In other words, the orbital pair-breaking effect should be neglected or weak. Non-centrosymmetric superconductors do not exhibit such field-induced phase transition; thus, this is unique physics in the locally non-centrosymmetric system. Furthermore, the PDW state is categorized as odd-parity superconductivity [113]. In the locally non-centrosymmetric superconductor $CeRh_2As_2$, the field-induced phase transition has been observed, and the high-filed region is called the odd-parity state [110]. I will introduce the $CeRh_2As_2$ in the next section. I have introduced the bilayer system, but trilayer systems and more have been extensively investigated. These results are similar to the bilayer system, but a slightly different behavior was suggested since the center layer does not have inversion symmetry breaking. I would like you to refer to the following papers Refs. 103, 111, and 112 to understand more-layer cases.

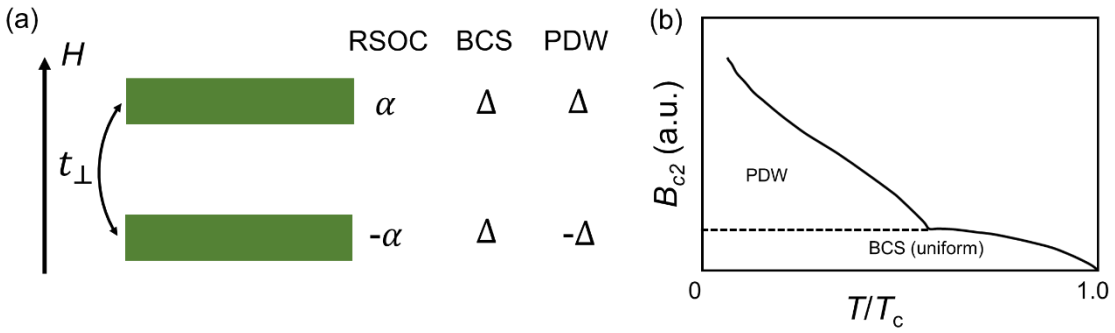

Fig. 3.3. (a) Schematic figure of the bilayer system for PDW state parallel to the out-of-plane direction. The green bars represent the 2D conducting layers. The structure of staggered RSOC and superconducting order parameters in BCS and PDW states are shown on the right-hand side of the figure. The presence of interlayer coupling ($t_\perp \neq 0$) is shown on the left-hand of the figure. Applied magnetic fields are perpendicular to the plane. (b) Example of the T-B_{c2} phase diagram for the PDW state. The solid and dashed curves show the second- and first-order phase transition. These images were described based on Ref. 111.

(II). Complex stripe (CS) phase to Helical phase in magnetic fields parallel to the *ab*-plane [103, 109, 114, 115]

Next, I introduce the CS phase. It is the case for the magnetic field parallel to the in-plane direction. I consider the bilayer system as well as the PDW case. First, if we neglect the interlayer coupling and make the layers completely decoupled, i.e., we consider the pure RSOC effect in the individual layer, magnetic fields parallel to the plane can induce a helical phase, which has finite center-of-mass momentum $\boldsymbol{q}$ pairing. Such a finite-momentum pairing (Helical phase) is expected in non-

centrosymmetric superconductors [95, 96]. Owing to the opposite sign of RSOC, the wave vectors of the superconducting order parameter have opposite signs in the two layers. When the interlayer coupling is effective, the complex order parameters between two layers can mix (see Fig. 3.4). This is called the CS phase because of a complex phase with a strip structure. This state is unique in the locally non-centrosymmetric system. The CS phase is stabilized in the magnetic field due to the finite center-of-mass momentum $\boldsymbol{q}$ and the interlayer coupling, while the BCS state exists at zero field. The orbital pair-breaking effect is not considered so far because the weak in-plane hopping, which is proportional to the Fermi energy E_{F}, is assumed compared with the RSOC, i.e., the paramagnetic pair-breaking effect is predominant. The orbital pair-breaking effect can give rise to the CS phase as well. When the orbital pair-breaking effect is dominant (strong in-plane hopping), the CS phase is induced by quantized vortices penetrating between the layers. The vortex-induced CS phase is regarded as the Josephson vortex phase. Moreover, with further increasing magnetic fields, the interlayer coupling δ is weakened (δ approaches zero with increasing the in-plane magnetic fields), and thus Helical phase can emerge (independent superconducting states are stabilized). Hence, there are two kinds of CS phases by the paramagnetic or orbital pair-breaking effects. Furthermore, intriguing superconducting phases can be realized by competition of the two CS phases (moderate in-plane hopping) by paramagnetic pair-breaking effect (RSOI) and orbital pair-breaking effect (Josephson vortex): this is the PDW state even in the in-plane magnetic-field direction. In order to provoke the PDW state along the in-plane direction, the sign of the center-of-mass momentum $\boldsymbol{q}$ needs to be inverse between the two CS phases by paramagnetic and orbital pair-breaking effects. Under this condition, we may call the CS phase induced by the paramagnetic pair-breaking effect the antivortex phase (basically, the sign of the center-of-mass momentum $\boldsymbol{q}$ depends on the band structure and the sign of RSOC). When these two CS phases by the paramagnetic and orbital pair-breaking effects are in balance, the interlayer coupling stabilizes the uniform superconducting states, and thus the center-of-mass momentum $\boldsymbol{q}$ becomes zero. The sign of the superconducting order parameter is inverse between the layers as well as the *c*-axis magnetic field case. Consequently, the balance of the paramagnetic (RSOI) and orbital (Josephson vortex) pair-breaking effects can lead to the PDW state in magnetic fields parallel to the *ab*-plane direction.

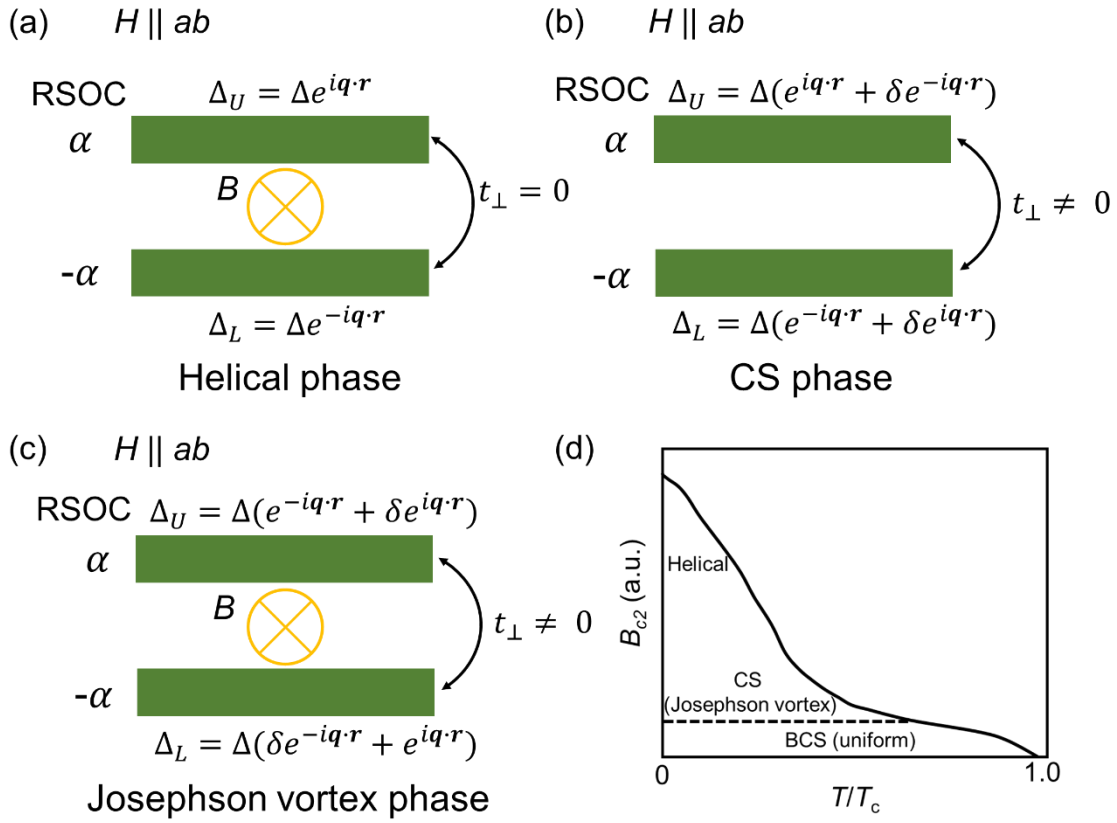

Fig. 3.4. (a-c) Schematic figures of bilayer system for (a) the Helical, (b) the complex-strip (CS) phases, and (c) the Josephson vortex phase. The Josephson vortex phase is a kind of CS phase. The green bars represent the 2D conducting layers. The structures of the staggered RSOC are described on the left-hand side of the green bars. The superconducting order parameters for the upper and lower layers are shown on the top and bottom of the green bars, respectively. In the case of the Helical phase, the interlayer coupling is neglected ($t_\perp = 0$), and the orbital pair-breaking (Josephson vortex) is assumed. In the case of the CS (antivortex) and Josephson vortex phases, the finite interlayer coupling is assumed ($t_\perp \neq 0$). Applied magnetic fields are parallel to the planes for all cases. In the Helical and Josephson vortex phases, the quantized vortex is described between the superconducting layers. (d) Example of the T-B_{c2} phase diagram for the CS and Helical phases. The solid and dashed curves show the second- and first-order phase transition, respectively. These images were described based on Refs. 109 and 114.

3.3. Local inversion symmetry breaking and superconductivity: experimental aspect

Experimental studies for local inversion symmetry breaking have been developed in 2D compounds. The orbital pair-breaking effect along the *ab*-plane magnetic field is suppressed in the 2D systems, as explained in Section 3.1. Consequently, we can naively investigate the paramagnetic pair-breaking

effect using 2D compounds. The first example of the locally non-centrosymmetric superconductors is artificial superlattices composed of heavy-fermion superconductor $CeCoIn_5$ and normal metal $YbCoIn_5$ (block layers), where the inversion symmetry is locally broken at the interface between the $CeCoIn_5$ layer [105–107]. However, the global inversion symmetry is present for the whole lattice. Thus, the staggered RSOC can emerge due to the local inversion symmetry breaking along the out-of-plane direction. The RSOI can lead to the weakening of the paramagnetic pair-breaking effect. Moreover, in this system, the RSOC can be tuned by the modulation of both $CeCoIn_5$ and block layers. They revealed the change of the pair-breaking nature from the angular dependence of the B_{c2} (T) by modulating the layers. The cusp-like behavior of the angular dependence of B_{c2} (T) around the plane [put differently, the 2D-Tinkham model (Eq. 10.2) is effective] exhibits the orbital pair-breaking effect is predominant, which indicates that the paramagnetic pair-breaking effect is diminished due to the RSOI. On the other hand, the suppression of the cusp shows that the paramagnetic pair-breaking effect is predominant [the 3D-GL model (Eq. 10.1) is effective], which implies that the modulation of the layers weakens the RSOC. Unfortunately, the PDW state in the *c*-axis-field direction and the CS phase in the *ab*-plane-field direction has not been observed in the artificial superlattice. However, we expect that the local RSOI plays an essential role in the electronic state from these results.

I introduced the monolayer of MoS_2 as the non-centrosymmetric (global inversion symmetry breaking) 2D superconductor. In contrast, the MoS_2 bilayer (2H-MoS_2) has global inversion symmetry, while the inversion symmetry within the individual layers is locally broken [108]. In the monolayer of these transition-metal dichalcogenides, the Zeeman-type SOI, by the lack of in-plane inversion symmetry, generates the Ising pairing, which leads to the protection from the departing of the Cooper pairs against the in-plane magnetic field. The interlayer Josephson coupling between the layers exists in the bilayer system. The Zeeman-type SOC and the interlayer Josephson coupling can be controlled by tuning the carrier concentration in the individual layers. The in-plane B_{c2} (T) can be depressed below the conventional Pauli limit in the bilayer system, which implies that the Ising protection is strongly weakened by the enhancement of the interlayer Josephson coupling (orbital pair-breaking effect by conventional Abrikosov vortices may be predominant).

The CS phase in the magnetic field parallel to the plane was observed in the thin films stacked by Pb and Sb [109]. In this system, the coupling strength between the Pb monolayer films was controlled by changing the thickness of the Sb spacer layer. They investigated the bilayer and trilayer systems. The observed in-plane B_{c2} (T) is similar to the theoretically predicted phase diagram in magnetic fields parallel to the *ab*-plane for locally non-centrosymmetric superconductors. The interlayer Josephson coupling favors the BCS state with a uniform order parameter, denoted as BCS in Ref. 109, in zero and low fields parallel to the plane ($\boldsymbol{q} = 0$). With increasing magnetic fields, the CS phase with a finite center-of-mass momentum emerges ($\boldsymbol{q} \neq 0$). As introduced above, the CS phase can originate from the staggered RSOI (the paramagnetic pair-breaking effect is predominant) and the Josephson vortex

state between the layers (the orbital pair-breaking effect is predominant). This case exhibits the latter: the CS phase is induced by the quantized vortices penetrating the Sb spacer layer. Interestingly, by further increasing magnetic fields, the transition from the CS phase to the helical phase was observed, which results from the interlayer Josephson coupling δ between the layers being effectively weakened by the magnetic fields (δ approaches zero). Thus, this Helical phase has a finite center-of-mass momentum $\boldsymbol{q}$ and almost zero interlayer Josephson coupling. The upturn behavior of the B_{c2} (T) was observed in the high-field regions, and they suggested that the upturn corresponds to the transition from the CS phase to the Helical phase.

I have introduced 2D systems so far; however, studies of bulk single crystals for heavy-fermion superconductor $CeRh_2As_2$ have been extensively developed [110]. The crystal structure of $CeRh_2As_2$ has a centrosymmetric tetragonal $CaBe_2Ge_2$-type structure [the space group is $P4/nmm$ (No. 129, D_{4h})]. However, the Ce site lacks local inversion symmetry with the C_{4v} site-symmetry group. (The crystal structure of our target materials is the same as the $CeRh_2As_2$, and Bi and Ch sites lack the local inversion symmetry with the C_{4v} site point group.) Therefore, we can regard that there are two local non-centrosymmetric layers of Ce per unit cell. The obtained c-axis B_{c2} is approximately 14 T, even at T_c = 0.26 K, which vastly exceeds the Pauli limit. The orbital pair-breaking effect is also suppressed due to the heavy-fermion electronic states. Moreover, they suggested that the c-axis B_{c2} (T) behavior exhibits a phase transition from even parity to odd parity. The superconducting phase diagram is similar to the theoretical prediction about the PDW state in the c-axis magnetic field. They named the high-field superconducting state odd parity because the PDW is categorized as odd-parity superconductivity, as introduced above [113]. Such multiphase superconducting states were limited, such as UPt_3. However, this study proposed that odd-parity superconducting states can be created by increasing magnetic fields even if the superconducting order parameter belongs to the even-parity and spin-singlet superconductivity in the zero and low fields. Note that the mixture of spin-singlet and spin-triplet is not so significant, but the relative magnitude of the RSOC and the interlayer coupling is essential to generate the odd-parity (PDW) state in the magnetic fields. Moreover, the odd-parity superconductor is a promising candidate for topological superconductors [113, 116]. Therefore, the locally non-centrosymmetric superconductors can create a new way to explore topological superconductors.

4. Weak antilocalization (WAL)

4.1. Weak localization (WL) and weak antilocalization (WAL)

Localization has been the central topic of condensed matter physics for a long time. The pronounced impact of the localization study is the prediction of the Anderson localization, which suggests that the localization state of the conduction electron can occur in disordered systems [117, 118]. Anderson predicted the Andeson localization in 1958, but it took about 20 years to significantly develop the study [119]. Originally, the usual Boltzmann theory neglects interferences between the scattered partial waves. The momentum of the electron wave exponentially disappears by the impurity scattering after the time τ. Thus, the Boltzmann theory simply leads to the simple Drude formula for the conductivity

$$\sigma = \frac{ne^2\tau}{m}, \tag{4.1}$$

where m and n exhibit the mass of the electron and the density of the electrons. However, the neglected interference really plays a significant role in the disordered metal system [119]. We consider the electron wave in the distribution of the impurities such as disordered metal systems [see Fig. 4.1 (a)]. The electron wave is continuously scattered at the impurities, and there is backscattering. If time-reversal symmetry is preserved in the system, i.e., without magnetic impurities and magnetic field, there is a time-reversal path for the backscattering. The two paths of the backscattering are constructive to each other, and thus the two waves interfere. As a consequence, the probability of the backscattering is enhanced, and the conductance reduces. That is caused by quantum correction to the conductance, often called quantum interference. The quantum correction to the conductance in the 2D systems is given as

$$\Delta\sigma = -\left(\frac{e^2}{\pi^2\hbar}\right)\log\left(\frac{L}{\ell}\right), \tag{4.2}$$

where L and ℓ present the sample size and mean free path of the electron. A scaling theory and Kubo formula give rise to quantum correction. I would like you to refer to the following papers in detail [120, 121]. The phenomenon is called weak localization (WL) because of a precursor of localization. WL occurs in one-, two-, and three-dimensional materials. However, the 2D system is the most famous experimental investigation since the localization inevitably occurs in the 2D systems regardless of the magnitude of the impurity scattering. We can easily see the quantum-interference effect in the 2D systems in the magnetic field perpendicular to the plane. Indeed, many experimental WL studies have been performed using 2D materials [119, 122, 123]. In the experimental work, it is significant to investigate magnetoresistance (MR). Applying magnetic fields suppresses the quantum interference since the time-reversal symmetry is broken, and a phase shift is realized in the wave function. Therefore, the resistance decreases with applying magnetic fields, called negative MR [see Fig.4.1

(b)]. The existence of negative MR is necessary for experimentally suggesting the WL (Anderson localization). I have not mentioned spin-orbit coupling so far. Interestingly, the presence of the SOC causes the sign change of the quantum correction to the conductance [124]. The strong spin-orbit scattering leads to destructive interference, and thus the resistance decreases compared with the WL case at the zero field. Thus, the MR behavior also changes the sign, which is generally called weak antilocalization (WAL) [see Fig. 4.1(c)]. The 2D magnetoconductance (MC) behavior by the WAL is well described by the Hikami-Larkin-Nagaoka (HLN) model [124]

$$\Delta G = \frac{\alpha e^2}{2\pi^2 \hbar}\left[\psi\left(\frac{1}{2}+\frac{\hbar}{4el_\phi^2 B}\right) - \ln\left(\frac{\hbar}{4el_\phi^2 B}\right)\right], \tag{4.3}$$

where the α is prefactor, l_ϕ is the phase coherence length, and ψ is the digamma function. The α is -0.5 in a single surface (channel) without magnetic impurities and with spin-orbit coupling [124]. The HLN theory has also been used for analyzing WL [125, 126]. In the case of the WL, the sign of α changes, and thus we may regard the α as the type of localization (WL or WAL) [126]. Thus, the α has been used as the phenomenological parameter in the experimental studies [126, 127]. The phase coherence length l_ϕ is where the WL or WAL occurs by the scattering. When the phase coherence length l_ϕ is smaller than the magnetic length l_B, which is the length that the localization of WAL or WL is kept under the magnetic fields, the WL or WAL dominates. Note that Ref. 119 suggests that the HLN theory does not describe the high-field MR data so well. Therefore, we should analyze the low-field data by the HLN theory. Indeed, the HLN theory has been used for low-field experimental data in several experimental studies [127–129]. We can estimate the characteristic fields from the phase coherence length l_ϕ by the relation $B_\phi = \hbar/4el_\phi^2$. When the applied magnetic fields exceed the B_ϕ, the WL or WAL are suppressed. HLN theory is assumed in the spin-orbit coupled impurities (spin-orbit scattering), but the HLN theory has been used for the materials with strong SOC lattice in nature, such as a gold film, and there is good agreement with the theory and the experiments [119]. Nowadays, the HLN theory has been developed to analyze whether the surface state has the presence of topological surface conduction channels and how these parameters change with altering temperature, thickness, and doping level [126–128]. I will introduce several examples of WAL in the next section.

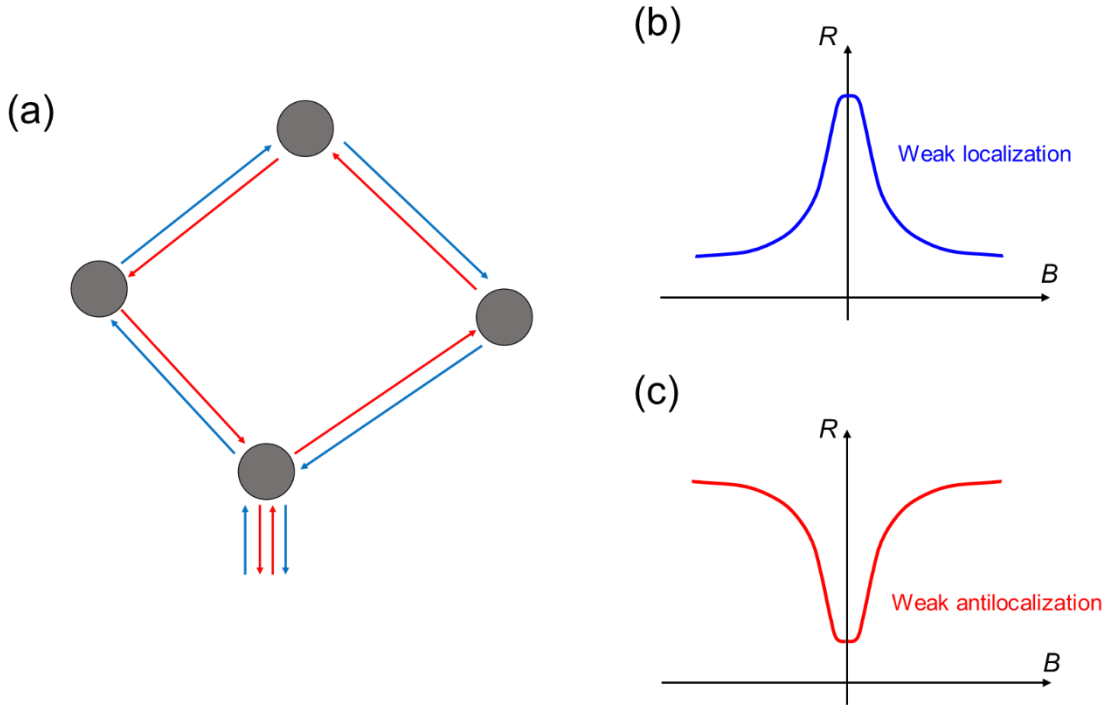

Fig. 4.1. (a) Schematic figure of weak localization (antilocalization) effect in 2D disordered conductors. Gray closed circles show non-magnetic impurities and/or defects. The red and blue paths (electron waves are assumed) have a time-reversal relationship. Weak (strong) spin-orbit coupled impurities lead to constructive (destructive) interference, which exhibits weak localization (weak antilocalization). (b,c) Conceptional figures of the field dependence of the resistance for (b) weak localization and (c) weak antilocalization.

4.2. Material examples of WAL

In this section, I briefly introduce the material examples of WAL. WAL studies have been intensively investigated by using HLN theory in 2D materials. When building the HLN theory, the WAL effect was investigated by single-element thin films such as Mg, Cu, Bi, and Au [119]. The thin Mg film was examined as the weak SOC element. The MR data of the Mg film exhibit negative MR in entire temperature regions, which indicates that the constructive interference is suppressed and the WL state emerges. When 1% Au layers, which have a strong SOC, are introduced to Mg layers, the MR increases at low temperatures and low fields [125]. Strong spin-orbit coupled impurities (spin-orbit scatterings) lead to destructive interference: this is the WAL state. A Cu film, regarded as a moderate SOC, is investigated. The MR behavior of the Cu film is different from the pure Mg. The SOC contribution is significant at low temperatures and low fields, and the WAL emerges at low fields. In other words, the phase coherence length l_ϕ is larger than the spin-relaxation length l_{SO}, which is the characteristic length of spin-orbit scattering and can also be estimated from the HLN theory or the

Iordanskii, Lyanda-Geller, and Pikus (ILP) theory, where inversion asymmetry is considered [129–132]. With increasing magnetic field, the magnetic length is less than the spin-orbit scattering length, and the WAL behavior is suppressed. In addition, in high-temperature regions, the SOC contribution is small, and the WAL behavior disappears at low fields. A gold film regarded as a strong SOC is also examined, and the MR data show the WAL behavior at low fields in the broad-temperature region [133]. The negative MC (positive MR) is kept up to relatively high fields, probably due to the strong SOC of Au. These observed MC and MR data agree with the HLN theory. Therefore, it is essential to have strong SOC lattices or spin-orbit coupled impurities that cause destructive interference at zero field to realize the WAL at low fields.

In recent topics, the WAL has been developed in topological materials. A promising topological-insulator candidate of Bi_2Se_3 and its related materials has also been extensively studied in the WAL context [126, 128]. The surface state is significant in topological materials. Therefore, it is necessary to investigate whether the surface contribution is predominant in the compounds or bulk. As introduced above, the α is -0.5 for a single surface (channel) in the HLN theory in the WAL state. In these compounds, there are two surface states on the top and bottom surfaces, and then $\alpha \approx$ -1 has been observed. Note that the origin of this WAL for the topological materials is distinct from the spin-orbit scattering by the strong spin-orbit coupled impurities or the materials with the strong SOC in nature. In topological insulators, the Berry phase of π leads to the WAL [128, 134]. A similar WAL has been observed in Graphen [135]. Thus, in these topological materials, the Berry phase π leads to destructive interference. Given the weak SOC of carbon atoms, we can understand that the mechanism is clearly different from the conventional WAL due to the spin-orbit scattering by strong spin-orbit coupled impurities or strong SOC lattice, while the Bi_2Se_3 and its related compounds have a strong SOC from the Bi-6p_x/6p_y orbitals.

The WAL studies have been performed in the transition metal dichalcogenides as well. Various transition metal dichalcogenides, such as WTe_2, $MoTe_2$, WSe_2, $TaSe_2$, $PtTe_2$, MoS_2, and VSe_2, show the WAL in low-filed regions [129–131, 136–139]. Basically, the strong SOC is expected to be the role that causes the WAL. However, MoS_2 and VSe_2 exhibit the WAL behavior in the low-field regions even in relatively weak SOC [130, 139]. The enhancement of WAL by the quantum confinement in the 2D limit or π-Berry phase may make the observation of the WAL effect possible in these systems [130, 139]. However, the origin is still unclear. In addition, other intriguing physical properties, such as Zeeman-type SOI due to the in-plane symmetry breaking and CDW formation, and these relationships between the WAL have been investigated for these systems.

A crossover from WAL to WL has been observed in several materials by controlling temperature, carrier concentration, thickness, and elemental substitution [126, 129, 135, 139]. Whether the origin of WAL is the strong SOC or the Berry phase depends on the kind of material. However, in any case, the crossover state can be realized by changing the constructive to destructive interference by several

parameters. I have introduced 2D systems so far. In bulk 3D systems, the α becomes much larger than in 2D systems [162–164]. I will show the results in Chapter 9.

5. Nematic superconductivity

5.1. Nematic electronic states

The word “nematic” (“nematicity” in the noun), originating from the research field of liquid crystals, exhibits the states with the spontaneous rotational symmetry breaking of the bar-shaped liquid crystal molecules but without breaking the translational symmetry. Nowadays, this word is extended to solid-state physics, and the electronic state shows the spontaneous rotational symmetry breaking without breaking the rotational symmetry in the crystal structure. Electronic nematicity has been studied in several unconventional superconductors such as cuprate, iron-based, and ruthenate superconductors [9, 18, 140]. Significantly, the iron-chalcogenide system is the main target for studying electronic nematicity [18]. So I briefly show the studies about this system as a representative of electronic nematicity. The iron-chalcogenide FeSe has a tetragonal structure at room temperature and shows superconductivity at $T_c \approx 9$ K. FeSe also exhibits nematic (structural) transition $T \approx 90$ K, and the nematic transition is suppressed by pressure and vanishes around 2 GPa.The nematic state means the orbital ordering, in which the degeneracy of d_{xz} and d_{yz} of Fe 3*d* orbitals is lifted. On the other hand, FeSe exhibits a spin-density-wave state, a stripe-type long-range antiferromagnetic order in applying pressure (from ~2 GPa to ~6 GPa), while no magnetic order in the ambient pressure. The antiferromagnetic order breaks the rotational symmetry of the tetragonal lattice. Thus, given the analogy of the iron-pnictide systems where the antiferromagnetic order always accompanies the nematicity, we can deduce that the magnetic order (spin contribution) leads to the nematic states in the FeSe as well. However, it has been suggested that applying pressure can induce antiferromagnetic order by changing the FS topology. Therefore, it is difficult to determine whether the driving force of the electronic nematicity is the orbital or spin degrees of freedom because of the entangled situation. In contrast, sulfur substitution strongly suppresses the antiferromagnetic fluctuation and thus makes the magnetic contribution weak. In the S-substituted $FeSe_{1-x}S_x$, the nematic susceptibility, evaluated from the elasto-resistivity measurements using a piezoelectric device, diverges at $x \approx 0.17$, indicating that there is a nematic QCP around $x \approx 0.17$. Therefore, we can expect that the orbital ordering is essential for the nematic state in the iron-chalcogenide systems. Moreover, the temperature dependence of the resistivity at $x \approx 0.17$ presents the linear behavior, implying the non-Fermi liquid behavior, which is an indication of the QCP. It was reported that the superconducting gap structure could change when crossing the nematic QCP, suggesting that the nematic state probably correlates with superconductivity. The nematic transition in the iron-chalcogenide system may be regarded as the structural transition from tetragonal to orthorhombic. However, it is believed that the electronic contribution is the origin of the nematicity because the crystal (orthorhombic) distortion is tiny (~0.5%) below the nematic transition.

5.2. Nematic superconductivity

In recent studies, nematic superconductivity has been investigated in the topological superconductor candidate dope-Bi_2Se_3 systems as the target material [141]. The rotational symmetry breaking on the basal plane for doped-Bi_2Se_3 compounds was observed in various probes, such as NMR Knight shift, specific heat, and MR in the superconducting states [142–144]. Nematic superconductivity is distinct from electronic nematicity in normal states such as iron-based superconductors. In nematic superconductivity, the superconducting gap amplitude spontaneously breaks the rotational symmetry of the lattice as a consequence of the superconducting order parameter. On the other hand, the orbital and/or spin degrees of freedom cause the electronic nematicity above T_c in the normal states. According to theoretical calculations, nematic superconductivity occurs even in the fully gapped *s*-wave state by the uniaxial strain [145, 146]. In the doped-Bi_2Se_3 systems, odd-parity superconductivity is expected as the superconducting state and categorized as topological superconductivity [147]. In the odd-parity state, a two-component superconductor (multi-dimensional irreducible representation E_u) is suggested for the doped-Bi_2Se_3 superconductor. (Note that, for example, the fully gapped *s*-wave state is categorized in single-component A_{1g}.) The counterpart in the two-component superconductivity can cause the nematic state. The two superconducting components are called the Δ_{4x} and Δ_{4y}. Ordinally, the two components form a complex linear combination to satisfy the rotational symmetry of the lattice, such as $p_x \pm ip_y$. However, in the present case, the strong spin-momentum locking forces a non-unitary superconducting state, i.e., the complex linear combination does not occur, and the counterpart of Δ_{4x} or Δ_{4y} states is selected [141]. Whether the Δ_{4x} is favorable or Δ_{4y} has not been completely determined, and also it is suggested that the two states almost degenerate. However, a recent uniaxial strain experiment revealed that the Δ_{4y} state is stabilized under the uniaxial stress [148].

Given this discussion, multi-component superconductivity is a promising candidate for the nematic superconductor. Indeed, the two-fold symmetric behavior of the thermal conductivity in the superconducting states was observed in UPt_3 (trigonal crystal structure), which has multi-component superconductivity [149], which may be considered a consequence of nematic superconductivity. However, there are few studies about nematic superconductivity because such multi-component superconductivity is rare. More recently, in kagome superconductor CsV_3Sb_5, in-plane rotational-symmetry breaking was observed in the superconducting states, indicating the nematic superconductivity [150]. On the other hand, *s*-wave superconductivity is suggested as the pairing state from the magnetic penetration depth measurements [151]. The *s*-wave state is categorized as single-component superconductivity, so nematic superconductivity cannot be realized without strain. In CsV_3Sb_5, it is proposed that CDW formation may be related to the nematic-like behavior [150].

6. Motivation for this study

The motivation for this study is to reveal the physical properties in both normal and superconducting states of $LaO_{1-x}F_xBiS_{2-y}Se_y$ (x = 0.2 and 0.5, y = 0–1) by using single crystals. The Se-substitution effect in the $BiCh_2$-based system was mainly examined by using polycrystalline samples. However, it is not easy to clarify the physical properties in detail using polycrystalline samples because $BiCh_2$-based compounds have quasi-two-dimensional electronic states from Bi-6p_x/p_y orbitals and thus large anisotropy between the *ab* plane and *c* axis. The reasons why I selected $LaO_{1-x}F_xBiS_{2-y}Se_y$ (x = 0.2 and 0.5, y = 0–1) in many kinds of $BiCh_2$-based compounds are below.

(I). The systems do not have 4*f* electrons in the RE sites and any magnetic elements. Thus, we can purely investigate the normal electronic and superconducting properties.

(II). We can easily synthesize Se-substituted samples from y = 0 to y = 1 in $LaO_{1-x}F_xBiS_{2-y}Se_y$. Thus, we can examine the Se-substitution effect in the wide Se-concentration regions.

(III). We can easily obtain relatively large single-crystal samples (*ab*-plane ~1 mm^2) by a high-temperature-flux method. Thus, we can efficiently perform transport properties by using bulk single crystals.

I mainly focus on two intriguing natures of the $BiCh_2$-based compounds. The first topic is the local inversion asymmetry in the $BiCh_2$ conducting layer. As introduced in Chapter 3, studies about locally non-centrosymmetric systems have been intensively developed for other systems. The F-doped (electron-carrier-doped) $BiCh_2$-based compounds belong to tetragonal *P*4/*nmm* (No. 129, D_{4h}), which has the inversion center. However, the $BiCh_2$ layer locally lacks the inversion symmetry with the C_{4v} site point group of Bi and Ch sites. The local inversion symmetry breaking can lead to the presence of the modulated RSOC. Theoretical calculations show that hidden spin polarization can exist in the $BiCh_2$-based systems [152], and the spin polarization was experimentally observed in spin-ARPES (SARPES) [153]. However, studies about local inversion asymmetry have not been extensively developed until now. That justifies the study focusing on the locally non-centrosymmetric nature of $BiCh_2$-based compounds. In particular, I expected that upper critical fields could be enhanced by the local RSOI analogous to global non-centrosymmetric compounds. Hence, I have performed the resistivity measurements under magnetic fields between the *ab* plane and *c* axis and discussed the behavior of upper critical fields (Chapter 10). In addition, I have investigated the crystal structure for non- and poor F-doped samples (Chapter 8) because it is significant to discuss the local inversion symmetry breaking. I used polycrystalline samples to examine the crystal structures since I performed powder X-ray diffraction (XRD). The second topic is localization. In previous work, electrical resistivity increases with decreasing temperatures even in optimally F-doped $LaO_{0.5}F_{0.5}BiS_2$ and La-doped $Sr_{0.5}La_{0.5}BiS_2$ [154–156]. The parent compounds $LaOBiS_2$ and $SrFBiS_2$ are band insulators, but the electron-carrier-doping level should be enough to become metal [60]. Moreover, $LaO_{0.5}F_{0.5}BiS_2$

and $Sr_{0.5}La_{0.5}BiS_2$ exhibit superconductivity at low temperatures under ambient pressure despite the slight increase in resistivity [57, 154–156]. Interestingly, the Se-substitution effect can suppress the increase of resistivity [154]. Sakai *et al*. suggested that the weak increase in resistivity is probably related to Anderson localization (WL) [156]. However, MR measurements were not performed. Thus, I devised an idea focusing on the localization-like behavior and performed MR measurements using single crystal samples of $LaO_{1-x}F_xBiS_{2-y}Se_y$ (Chapter 9). Finally, I investigated the in-plane anisotropy of MR in the normal and superconducting states to further reveal the physical properties of $BiCh_2$-based compounds.

7. Synthesis and physical properties measurements

7.1. Single-crystal growth

The target materials $LaO_{1-x}F_xBiS_{2-y}Se_y$ (x = 0.2, 0.5, y = 0, 0.25, 0.5, 0.75,1.0 as nominal values) single crystals were grown using a high-temperature flux method in an evacuated quartz tube [44, 45]. First, polycrystalline samples of $LaO_{1-x}F_xBiS_{2-y}Se_y$ were prepared by the solid-state-reaction method using starting materials of La_2O_3 (99.9%), La_2S_3 (99.9%), BiF_3 (99.9%), Bi_2S_3, and Bi_2Se_3. La_2O_3 has water-absorbing properties and thus becomes $La(OH)_3$ in the air for about two weeks. Therefore, I performed pre-annealing it at 700 ˚C for 15 h and confirmed that the peak pattern of powder XRD was consistent with pure La_2O_3 (ICSD data) before using it. The precursors of Bi_2S_3 and Bi_2Se_3 are synthesized by grains of Bi (99.999%), S (99.999%), and Se (99.999%). In evacuated quartz tubes, the annealing condition is at 700 ˚C for 15 h. I also confirmed that the peak patterns of Bi_2S_3 and Bi_2Se_3 are consistent with previous studies (ICSD data). Mixtures of these starting materials with nominal ratios of $LaO_{1-x}F_xBiS_{2-y}Se_y$ were mixed, pressed into a pellet, and annealed at 700 ˚C for 20 h in an evacuated quartz tube. The obtained polycrystalline samples are black pellets. The polycrystalline samples were pulverized, and I checked the XRD patterns using the powders (see Chapter 8). The polycrystalline powders of $LaO_{1-x}F_xBiS_{2-y}Se_y$ (0.4 g) were mixed with flux (5.0 g), and the mixtures were sealed into an evacuated quartz tube under ~10^0 Pa. I used the mixture of CsCl and KCl as the flux, and the molar ratio is 5 : 3 (the melting point is roughly 615 ˚C). The tubes were heated at 900 ˚C for 10 h and slowly cooled to 600 ˚C at a rate of -2.0 ˚C/h (175 h), followed by furnace cooling to room temperature. At room temperature, the quartz tube was opened under an air atmosphere, and the product was filtered and washed with pure water. The obtained single crystals are like silver plates [see Figs. 7.1(b) and 7.2] and stable in the air. The actual atomic ratios of the single-crystal samples for the physical properties measurements were estimated by energy-dispersive X-ray spectroscopy (EDX) with a scanning electron microscope (SEM) TM-3030 (Hitachi High-Tech). These values were almost consistent with the nominal composition.

7.2. X-ray diffraction (XRD)

XRD is one of the most important experiments to analyze crystal structures, from powders to single crystals. XRD techniques identify crystalline phases of various materials, and we can quantitatively analyze the phase. The physical properties depend on the crystal structures. Therefore, we need to analyze the crystal structures to reveal their physical properties. All crystals are arranged with translational symmetry. The scattered X-rays from the sample interfere with each other either constructively or destructively, which means that detectors can observe a signal only at angles where constructive interference occurs. The incident X-ray wave is scattered at different planes of the

material [see Fig. 7.1(a)]. Therefore, the diffracted X-rays have different optical path lengths to travel. The magnitude of this path length depends on the distance between the crystal planes and the incident angle θ of the X-ray beam. That is summarized in the famous Bragg's formula given as

$$n\lambda = 2dsin\theta, \quad (7.1)$$

where d is the length between diffraction planes, n is any integer, and λ is the wavelength of the X-ray beam. This equation means that constructive interference occurs only when the path difference (given by $2dsin\theta$) is a multiple (n = 1,2,…) of the wavelength of the X-ray beam. The use of the equation allows us to determine the distance between the lattice planes of the material since the wavelength in XRD experiments is known, such as Cu Kα (Cu Kα1: 1.5405 Å, Cu Kα2: 1.5443 Å), and the angles (the phase difference), at which constructive interference occurs, are measured. The obtained diffraction patterns are plotted by X-ray intensity on the vertical axis versus the angle 2θ (2θ is defined as the angle between the incident and the diffracted beam) on the horizontal axis. We can qualitatively analyze the XRD patterns compared with the previous studies in databases (e.g., ICSD). When we need to quantitatively analyze the XRD patterns, i.e., estimate the lattice parameters, the Rietveld refinement is a powerful tool for analyzing powder XRD data. The Rietveld method uses the least squares approach to refine a theoretical line profile until it matches the experimental data. I used RIETAN-FP software [55] to estimate the lattice constants of polycrystalline samples in this study. I performed XRD for single crystal samples with those put on the sample holders [see Fig. 7.1(b)]. In this case, only 00*l* peaks are observed, and I used PDIndexer software to estimate the *c*-axis lengths for single crystal samples [157]. Assuming a rock-salt-type crystal structure, we can estimate the *c*-axis lengths for single crystal samples from the 00*l* peaks. In this study, I performed two types of powder XRD: conventional laboratory system (Cu Kα X-ray, Rigaku) and synchrotron X-ray at the beamline BL02B2 of SPring-8 (Research proposals No. 2019A1114 (λ = 0.496197 Å) and 2019B1195 (λ = 0.496391 Å).

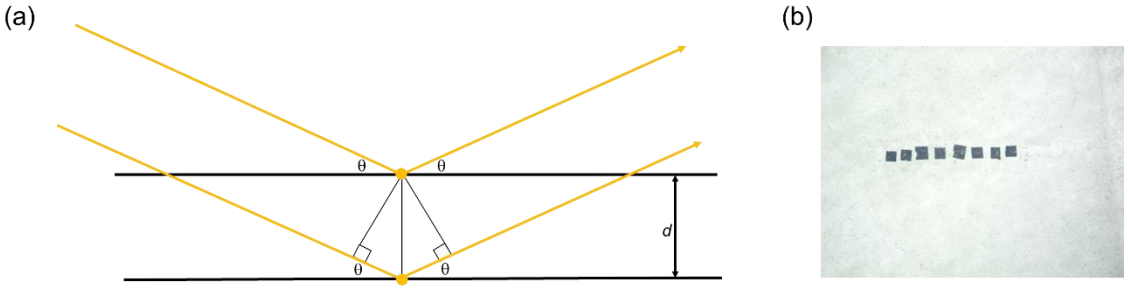

Fig. 7.1. (a) Schematic image of XRD. Black bars exhibit the lattice planes of the material. Yellow lines show X-ray beams. The d and θ represent the spacing between diffraction planes and incident angle. (b) Photo of the experimental setup of XRD for single-crystal samples. Several crystals are arrayed on the sample holder and fixed with a small amount of vacuum grease.

7.3. Resistivity measurements

I performed a four-terminal method for resistivity measurements in this study. The four-terminal method is useful for measuring small-resistivity samples such as metal. In the four-terminal geometry, two leads pass a current through the sample, and two separate leads measure the potential drop (voltage) across a sample section. The voltage leads ideally bring very little or no current. Therefore, the current through the sample and potential drop (voltage) across the sample can be known to a high degree of accuracy. Ohm's law can be used to calculate the resistance of the sample for the region between the two voltage leads. The setup removes the effects of lead contact resistance from the measurement results. The resistance is calculated using Ohm's law

$$V = RI, \tag{7.2}$$

where V is the measured potential drop (voltage) across the sample, R is the resistance of the sample, and I is the current through the sample. Resistivity ρ can be calculated from the R given by

$$\rho = R\frac{S}{\ell}, \tag{7.3}$$

where ℓ is the voltage lead separation and S is the cross-sectional area through which the current is passed. It is essential to configure the leads correctly to obtain exact resistivity. The current leads are typically located at the edge of the sample, while the voltage leads lie between them. An electric field is created when current is passed through the sample. The voltage leads should be adjusted to measure a potential drop across a region where the electric field lines are relatively straight. That is achieved by putting the voltage leads in line with the current leads or separating them by a small distance compared to their distance from the current leads. It is also significant for an accurate four-terminal measurement that the current and voltage leads do not contact the sample at the same place. Otherwise, the resistance will include the sample contact resistance. Figure 7.2(a) shows the sample configuration for the resistivity measurements of a single crystal sample of $LaO_{0.8}F_{0.2}BiS_{1.76}Se_{0.24}$ as the representative. I used gold wires and silver paste for mounting the samples.

I also performed four-wire Hall resistivity measurements by changing the geometry. When charged particles move perpendicular to a magnetic field, a force (Lorentz force) emerges on them perpendicular to both the magnetic field and the direction of particle motion (current). The force $\boldsymbol{F}$ can be exhibited as

$$\boldsymbol{F} = q\boldsymbol{v} \times \boldsymbol{B}, \tag{7.4}$$

where q is the charge of the electron or hole, $\boldsymbol{v}$ is the velocity of the charge, and $\boldsymbol{B}$ is the magnetic field. This transverse force can often allow the charge carriers to increase on one edge of a sample, which causes a potential difference across the sample. This potential difference is called the Hall voltage V_H. The sign of the V_H basically implies the sign of the charge carriers, and the absolute value of the V_H is related to the density of charge carriers in the sample. The Hall coefficient, R_H, describes these two properties and is defined as

$$R_H = \frac{E_{\mathrm{H}}}{jB} = \frac{V_{\mathrm{H}} S}{I \ell_{\perp} B}, \tag{7.5}$$

where E_{H} is the Hall field and j is the current density. For a well-defined geometry, the current density is equal to I/S where I is current, and the Hall field is equal to $V_{\mathrm{H}}/\ell_{\perp}$. Here, the $\ell_{\perp}$ is the distance between a set of transverse voltage leads used to measure the Hall voltage [see Fig. 7.2(b)]. It can be shown that the $R_H = (nq)^{-1}$ under the single-band model, where n is the carrier density. To measure the Hall voltage, we need to arrange the voltage leads perpendicular to both current and field directions. Figure 7.2(b) exhibits the sample configuration for the four-terminal Hall resistivity measurements of a single crystal sample of $LaO_{0.8}F_{0.2}BiS_{1.28}Se_{0.72}$ as a representative. I performed Hall resistivity measurements by such geometries under magnetic fields perpendicular to the planes. In order to remove the MR contribution, the Hall resistivity was modified and defined as

$$\rho_H(B) = \frac{\rho^+(+B) - \rho^-(-B)}{2}, \tag{7.6}$$

where ρ_H is $\rho_H = \frac{V_{\mathrm{H}} S}{I \ell_{\perp}}$ and $\rho^+(+B)$ $[\rho^-(-B)]$ is Hall resistivity in positive [negative] magnetic fields. In this study, the electrical resistivity, Hall resistivity, and MR measurements on the single-crystalline samples were performed by a conventional four-terminal method (see Fig. 7.2) in a physical properties measurement system (PPMS, Quantum Design) in Tokyo Metropolitan University and University of Amsterdam, a GM refrigerator (AXIS) in Tokyo Metropolitan University, pulsed magnet system at Solid State Physics (ISSP) at the University of Tokyo, and superconducting magnet at Institute for Materials Research (IMR) at Tohoku University.

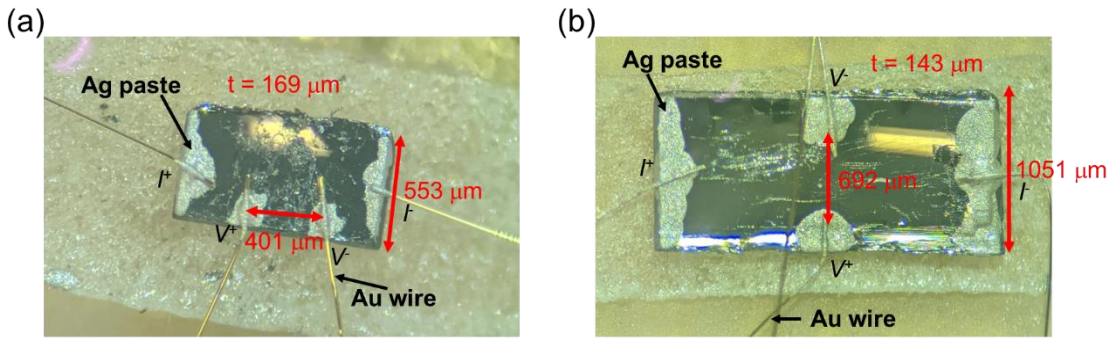

Fig. 7.2. Photos of sample configurations for four-terminal (a) electrical resistivity and (b) Hall resistivity measurements. The samples of (a) and (b) are $LaO_{0.8}F_{0.2}BiS_{1.76}Se_{0.24}$ and $LaO_{0.8}F_{0.2}BiS_{1.26}Se_{0.72}$ as the representatives, respectively. Silver paste and gold wire were used for mounting samples. The t in (a) and (b) means sample thickness.

8. Crystal-structural information

8.1. XRD patterns and lattice constants

First, I show the crystal-structural information for $LaO_{1-x}F_xBiS_{2-y}Se_y$. Figures 8.1 and 8.2 show the XRD patterns for the polycrystalline and single-crystal samples of $LaO_{1-x}F_xBiS_{2-y}Se_y$, respectively. Only 00*l* peaks were observed for the single-crystal samples (see Fig. 8.2) because the plate-like samples were arrayed in parallel on the sample holder [see Fig. 7.1(b)]. The Rietveld refinements were performed by using RIETAN-FP software [55] to estimate the lattice constants *a* and *c* of the polycrystalline. The tetragonal space group *P*4/*nmm* (No. 129, D_{4h}) is used for the refinement since the F doping (electron-carrier doping) leads to the stabilization of the tetragonal structure [38, 39]. I will show that the slight F-doping effect stabilizes the tetragonal structure in Section 8.2. The lattice constant *c* for the single-crystal samples was estimated by the PDIndexer software [157]. The refined lattice constants *a* and *c* for the polycrystalline samples and single crystals are plotted in Figs. 8.3(a) and (b). I present only the *c*-axis lattice constants for the single crystals because only 00*l* peaks were used for the refinement. The *a*-axis lattice parameter increases with increasing Se concentration since the ionic radius of Se is larger than that of S. The *c*-axis lattice constant of $x = 0.5$ is smaller than $x = 0.2$ since the electron-carrier doping (F substitution) is greatly sensitive to changing the *c*-axis length in the $BiCh_2$-based system [37]. Thus, there are slight variations of the *c*-axis lengths with the Se concentration because the lattice constant *c* is dependent on both F and Se concentration, and it is hard to precisely control the F-doping level (we cannot determine the actual value of F concentration by EDX due to the light element). The trend of the *c*-axis parameters for the single crystals with the Se concentration agrees with polycrystalline samples. The results indicate that the F and Se concentrations are somewhat successfully controlled in our single crystals.

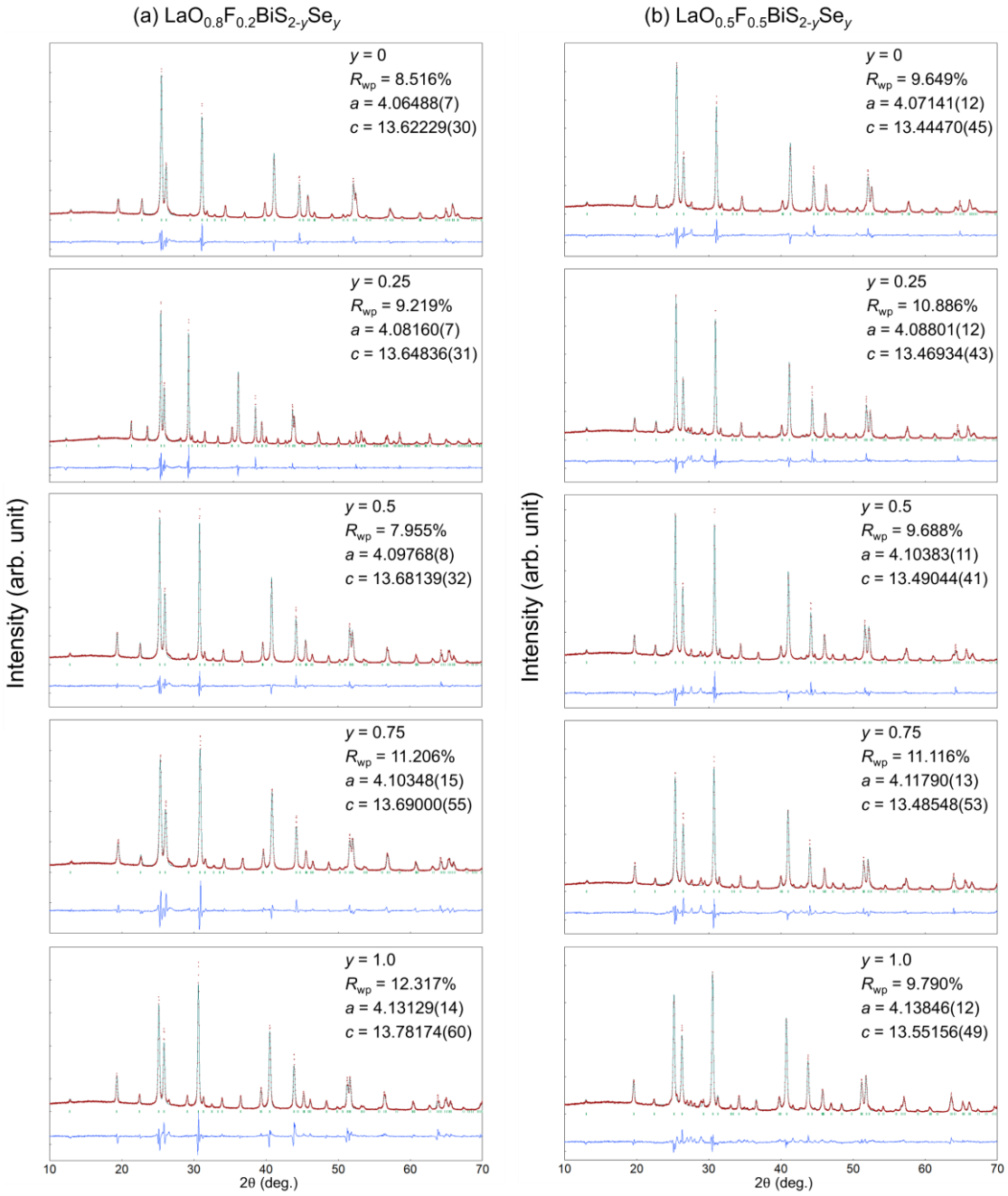

Fig. 8.1. Powder XRD patterns for the polycrystalline samples of (a) $LaO_{0.8}F_{0.2}BiS_{2-y}Se_y$ and (b) $LaO_{0.5}F_{0.5}BiS_{2-y}Se_y$. Red dots, green curves, green dots, and blue curves represent the experimental data, theoretically calculated curves, peak positions for the tetragonal phase *P*4/*nmm* (No. 129, D_{4h}), and residual curves between the experimental data and theoretically calculated curves, respectively. The Se concentrations *y* are nominal values. The lattice constants *a* and *c* are described in the insets of the figures. The *R*-factor R_{wp} is put in the insets as well.

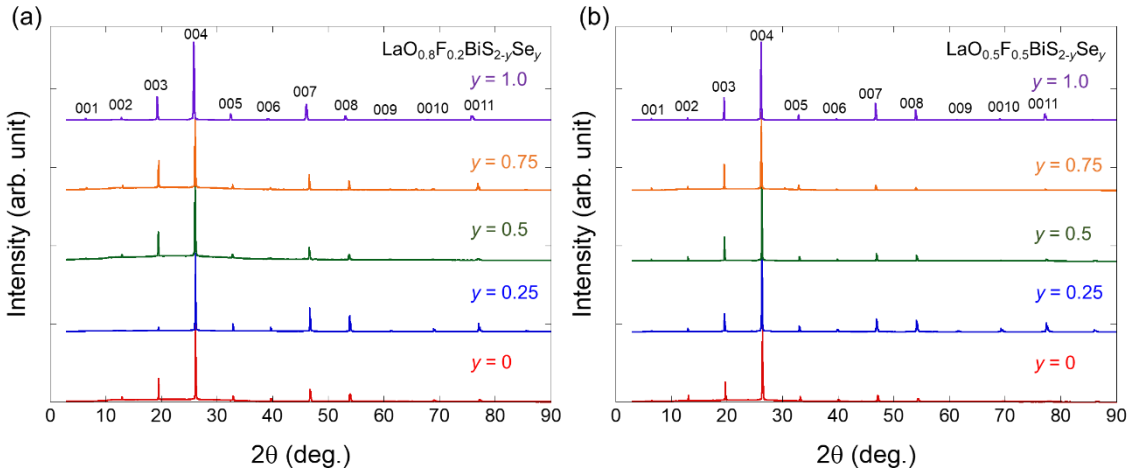

Fig. 8.2. XRD patterns for single-crystal samples of (a) $LaO_{0.8}F_{0.2}BiS_{2-y}Se_y$ and (b) $LaO_{0.5}F_{0.5}BiS_{2-y}Se_y$. The color variation expresses the nominal Se concentration. Only 00*l* peaks were observed and indexed in the inset of figures.

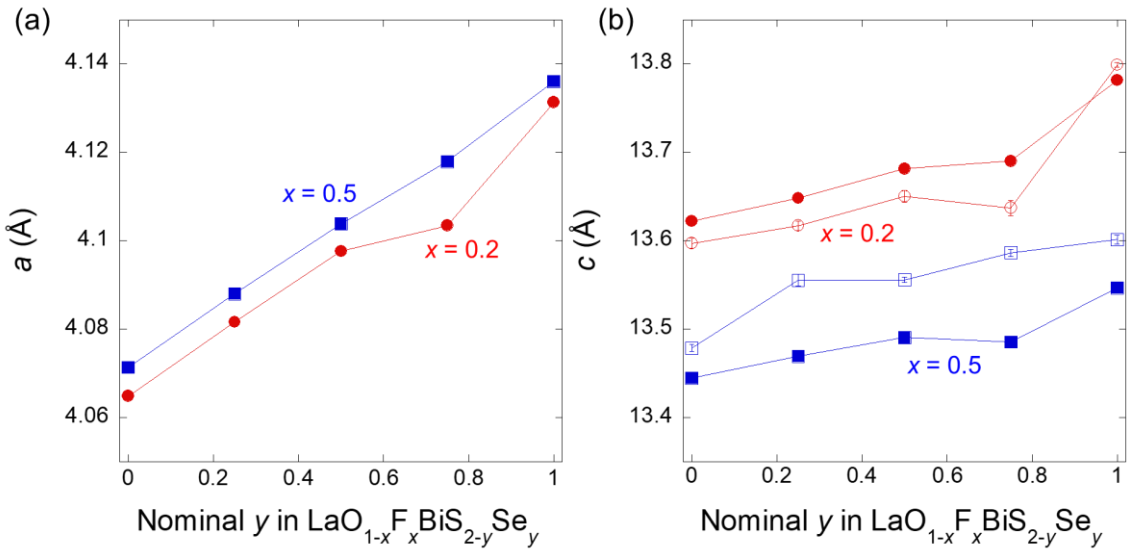

Fig. 8.3. Lattice constants (a) *a* and (b) *c* as functions of the nominal Se concentration *y* for the polycrystalline samples (closed red circles for $x = 0.2$ and blue squares for $x = 0.5$) and single crystals (open red circles for $x = 0.2$ and blue squares for $x = 0.5$) of the $LaO_{1-x}F_xBiS_{2-y}Se_y$.

8.2. Crystal-structural transition from monoclinic to tetragonal

As introduced in Chapter 2, F-free $LaOBiS_{2-y}Se_y$ belongs to the monoclinic structure ($P2_1/m$, No. 11) [36, 37]. I show that the crystal-structural transition from monoclinic to tetragonal ($P4/nmm$, No. 129) symmetry occurs by slight F substitution (electron-carrier substitution). The lattice constant *c* for the F-free and slightly F-doped $LaO_{1-x}F_xBiSSe$ ($x = 0$, 0.01, 0.02, and 0.03) shows a systematic decrease

with increasing nominal x, as shown in Figure 8.5(e), which suggests that electron carriers are systematically doped even in the low F-doping regime. In monoclinic phases, the 200 peaks split into 200 and 020. Therefore, by scanning the 200 peaks on temperatures, the structural transition temperature T_s and the evolution of the lattice constants a and b can be investigated. Figures 8.4(a)–(d) display the temperature dependences of the tetragonal 200 peaks and monoclinic 200 and 020 peaks on the synchrotron X-ray diffraction (SXRD) patterns for x = 0, 0.01, 0.02, and 0.03, respectively. Commonly, the 200 peaks shift to higher angles on cooling due to decreasing the lattice volume. As shown in Figure 8.4(a), the splitting of the 200 peaks into the monoclinic 200 and 020 peaks was observed below $T \approx 340$ K for x = 0, which indicates a structural transition to the monoclinic structure at $T_s \approx 340$ K. The peak intensity for x = 0 is rapidly suppressed with decreasing temperature when the temperature approaches T_s, indicating structural instability toward a structural transition (symmetry lowering). The decrease in peak intensity during the temperature scanning corresponds to the broadening of the peak in this experimental setup, in which the sample condition was not modified, and the temperature was continuously changed. The structural transition was observed for x = 0.01 at $T_s \approx 240$ K. In addition, a similar trend in the suppression of peak intensity was observed for x = 0.01 [see Fig. 8.4.(b)]. On the other hand, for x = 0.02 and 0.03, a clear structural transition was not observed down to 100 K. However, the suppression of the peak intensity was observed for x = 0.02. This signature implies that the sample has structural instability and a structural transition is expected below 100 K. Notably, the peak intensity is almost constant from 300 to 100 K for x = 0.03, which probably implies no structural transition at temperatures lower than 100 K. To quantitatively confirm the peak broadening with decreasing temperatures, the temperature evolutions of the full-width half maximum (FWHM) of the 200 peaks were estimated from the Gaussian fitting [see Fig. 8.6]. The values of FWHM are also consistent with the scenario above. These results suggest that the structural transition can be completely suppressed at a concentration higher than x = 0.03 in $LaO_{1-x}F_xBiSSe$. To analyze lattice constants a and b from the obtained data in Fig. 8.4, the 200 and 020 peaks were fitted by one or two Gaussian functions. Two Gaussian functions were used for x = 0 and 0.01, where clear structural transitions were observed. For x = 0.02 and 0.03, I analyzed the lattice constant with one Gaussian function. Figures 8.5(a) and (b) show the temperature dependence of the lattice constants a and b for x = 0 and 0.01. Indeed, the lattice constants a and b for x = 0 and 0.01 are split around T_s. For x = 0.02 and 0.03, the lattice constants linearly changed with decreasing temperature, which implies that the tetragonal structure may be dominant in this temperature regime. The trend that the structural transition from tetragonal to monoclinic is rapidly suppressed by slight F substitution in $LaO_{1-x}F_xBiSSe$ is consistent with the theoretical study which proposed that the tetragonal structure is more stable than monoclinic in F-substituted $LaOBiCh_2$ [38]. Due to the experimental limitation, we could scan the lattice constants on the temperature only at $T > 100$ K. Thus, I deduce that a structural transition below 100 K occurs for x = 0.02 from the suppression of

peak intensity. In contrast, because the peak intensity for x = 0.03 does not show a decrease down to 100 K, I assume that the low-temperature structure for x = 0.03 may be tetragonal. At least, I speculate that higher F concentrations above x = 0.03 stabilize the tetragonal structure even at lower temperatures. However, this study is performed by the powder-XRD investigation, and it is difficult to analyze the higher-angle peaks, such as 400 and 600 peaks, since the intensity at higher angles is relatively weak, and these peaks are overlapped with others. We need to perform the crystal-structural analysis using single crystals to confirm such peak splittings in detail. A recent synchrotron XRD study using the single-crystal sample $LaO_{0.5}F_{0.5}BiS_2$ found the presence of superlattice reflections below $T \approx 260$ K and suggested that it is related to the CDW formation [92]. Indeed, several theoretical calculations proposed that the one-dimensional nature of the Bi-6p_x/p_y orbitals exists even at the doping level of x = 0.5, which is related to the CDW formation by the FS nesting of the (π, π) direction [88, 89]. However, the synchrotron XRD of Ref. 92 does not detect the distinct structural transition from the tetragonal to monoclinic symmetry for $LaO_{0.5}F_{0.5}BiS_2$ down to 10 K. In contrast, the structural transition was clearly observed for the non-doped $LaOBiS_2$ [36]. Therefore, the *global* crystal structure for optimally F-doped $LaO_{0.5}F_{0.5}BiS_{2-y}Se_y$ belongs to the tetragonal symmetry (*P*4/*nmm*, No. 129) at least, and there may be *local* monoclinic distortion, which might be related to CDW formation, even in the tetragonal structures for $BiCh_2$-based compounds.

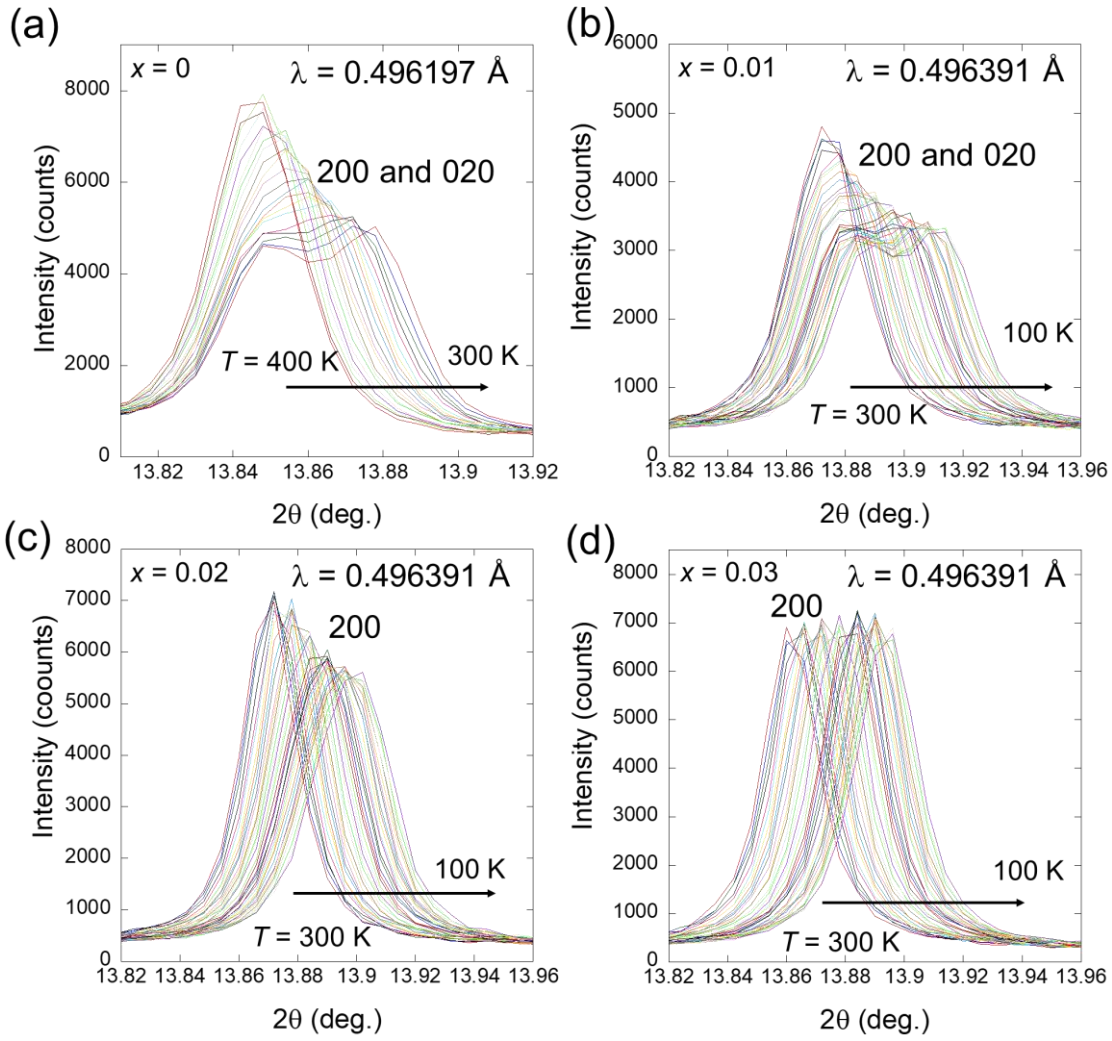

Fig. 8.4. Temperature evolutions of the 200 and 020 peaks of the synchrotron XRD patterns for (a) $x = 0$, (b) $x = 0.01$, (c) $x = 0.02$, and (d) $x = 0.03$ of $LaO_{1-x}F_xBiSSe$. The wavelengths used in the scanning are indicated in the figures.

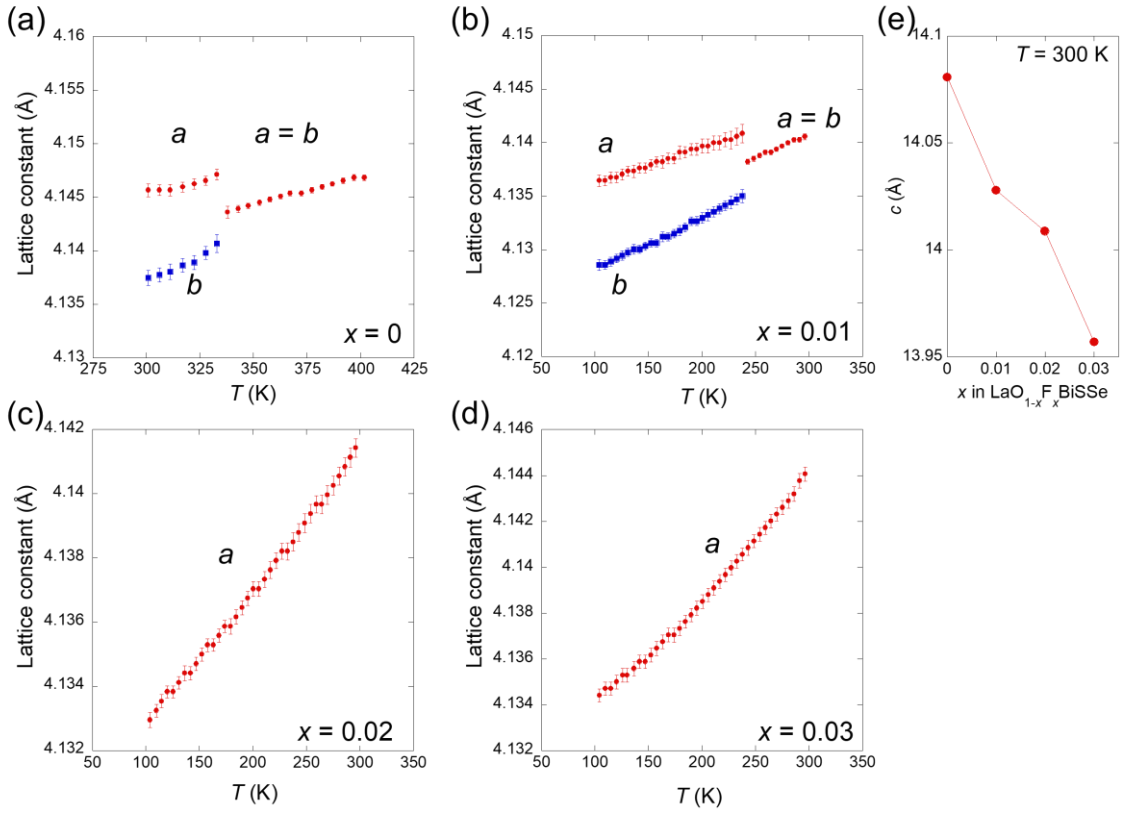

Fig. 8.5. Temperature dependence of the lattice constants *a* (red circles) and *b* (blue circles) for (a) *x* = 0, (b) *x* = 0.01, (c) *x* = 0.02, and (d) *x* = 0.03 in $LaO_{1-x}F_xBiSSe$. (e) F-concentration dependence of the lattice constant *c* at *T* = 300 K.

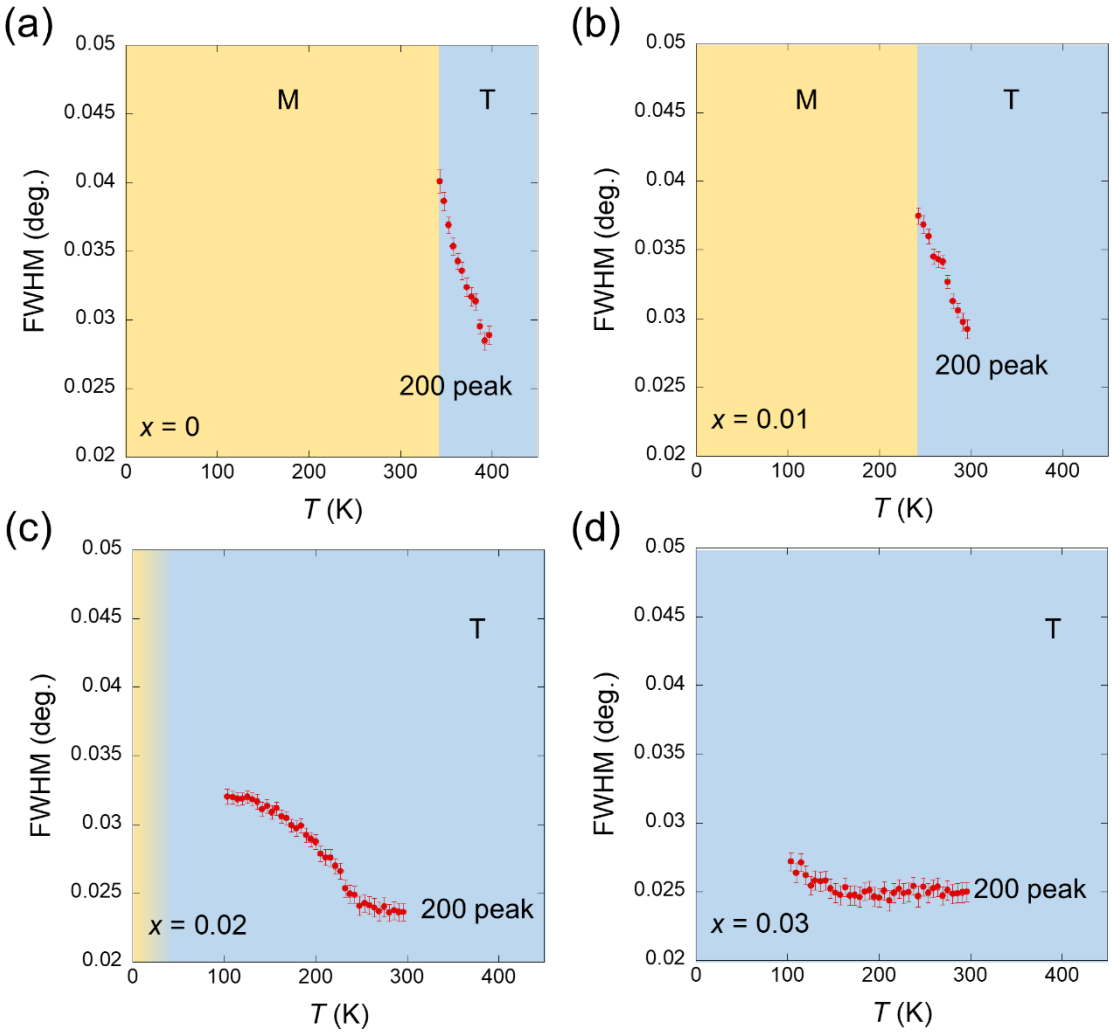

Fig. 8.6. Temperature evolution of full-width half maximum (FWHM) of the 200 peaks for (a) x = 0, (b) x = 0.01, (c) x = 0.02, and (d) x = 0.03 in $LaO_{1-x}F_xBiSSe$. Yellow and Blue regions represent monoclinic and tetragonal phases, respectively. The analysis of FWHM was performed only in the tetragonal phase because it is difficult to estimate the FWHM of 200 and 020 peaks due to the overlapped peaks.

9. WAL states induced by Se substitution

9.1. Previous results

As introduced in Section 2, the superconducting properties have been intensively investigated in the $BiCh_2$-based compounds. However, there is an unresolved problem in the normal-state-resistivity behavior. Previous experimental results for $LaO_{0.5}F_{0.5}BiS_2$ showed a weak increase in resistivity, although superconductivity emerges at low temperatures [155]. The experimental results are inconsistent with the theoretical calculations since the Fermi level crosses the conduction band for the doping level x = 0.5, and thus metallic behavior should emerge [60, 159]. Furthermore, the shielding volume fraction estimated from magnetization measurements is less than 10%, which indicates that superconductivity in $LaO_{0.5}F_{0.5}BiS_2$ is filamentary in nature [31, 33, 154]. Se substitution leads to the gradual suppression of the upward behavior in the resistivity, and heavily Se-doped $LaO_{0.5}F_{0.5}BiSSe$ shows almost metallic behavior and bulk superconductivity (the shielding fraction is roughly 100%) [31, 154]. I will show the magnetization data in Section 9.4. The Se-substitution effect is considered to act as chemical pressure, which leads to the depression of the in-plane disorder [37, 54]. These results imply that a localization phenomenon is in play that can be suppressed by Se substitution. Sakai *et al*. suggested that similar localized states reported for $Sr_{1-x}La_xFBiS_2$, closely related to $LaO_{1-x}F_xBiS_2$, may be due to Anderson localization [156]. If the states are related to Anderson localization, a negative MR is expected. However, MR data were not reported in the previous work. That justifies a systematic study to address the localization phenomena in $BiCh_2$-based systems by means of magnetotransport.

9.2. Electrical resistivity and Hall coefficient

First, I show the electrical resistivity measurements for $LaO_{1-x}F_xBiS_{2-y}Se_y$ (x = 0.2 and 0.5, y = 0-1.04). Figures 9.1(a) and (b) present the temperature dependence of the electrical resistivity in the *ab*-plane ρ_{ab} for x = 0.2 and x = 0.5, respectively. For x = 0.2 [Fig. 9.1(a)], Se-free $LaO_{0.8}F_{0.2}BiS_2$ (x = 0.2, y = 0) exhibits insulating behavior in the entire temperature range. The insulating behavior is gradually suppressed with increasing Se concentration, and superconductivity is observed at low temperatures for y = 0.46, 0.72, and 0.94. However, a weak increase of ρ_{ab} in the low-temperature region is still seen for y = 0.46 and 0.72, while in the high-temperature region, metallic behavior is observed. When the Se-substitution level reaches y = 0.94, metallic behavior is found in the entire temperature range. The x = 0.5 samples [Fig. 9.1 (b)] show a trend similar to the x = 0.2 samples. However, there is a clear difference between the Se-free samples: $LaO_{0.5}F_{0.5}BiS_2$ (x = 0.5, y = 0) shows a superconducting transition at $T \approx 2$ K, while $LaO_{0.8}F_{0.2}BiS_2$ (x = 0.2, y = 0) is insulating behavior in the entire temperature range down to 2 K. In addition, the absolute value of ρ_{ab} at low temperatures for $LaO_{0.5}F_{0.5}BiS_2$ is much smaller than that of $LaO_{0.8}F_{0.2}BiS_2$, despite the weakly insulating behavior

for $LaO_{0.5}F_{0.5}BiS_2$. These results indicate that electron-carrier doping (F substitution) suppresses the insulating characteristics, but a F (electron-carrier-doped) content $x = 0.2$ is insufficient to completely suppress the insulating state. However, heavily Se-substituted $LaO_{0.8}F_{0.2}BiS_{1.06}Se_{0.94}$ ($x = 0.2$, $y = 0.94$) with the same nominal $x = 0.2$ shows metallic behavior and superconductivity. Moreover, theoretical calculations suggest that a doping level of $x = 0.2$ should be sufficient to make the $BiCh_2$-based system metallic [60, 159]. The moderately Se-substituted samples ($y = 0.46$ and 0.72 with $x = 0.2$ and $y = 0.39$ and 0.65 with $x = 0.5$) exhibit metallic behavior in the high-temperature region, but a weak increase in ρ_{ab} at low-temperatures. In other words, ρ_{ab} in the normal states increases with decreasing temperature below T_{min} [see Figs. 9.1(a) and (b)]. Hence, I deduce that carrier localization occurs in these compositions. Thus, the $LaO_{0.8}F_{0.2}BiS_2$ phase is not a conventional band insulator but an insulator caused by carrier localization. A similar localization state was observed for polycrystalline samples of $Sr_{1-x}La_xFBiS_2$, which compares well to our target material $LaO_{1-x}F_xBiS_{2-y}Se_y$ [156]. The authors of Ref. 156 suggested that the weak increase in ρ_{ab} is due to Anderson localization (WL). I will discuss this possibility with the MR results in Section 3.4.

I performed Hall resistivity measurements to further investigate the physical properties in the normal states. Figures 9.1(c) and (d) show the temperature dependence of the Hall coefficient R_{H} for $x = 0.2$ and $x = 0.5$, respectively. As shown in the inset of Fig. 9.1(d), our experimental results show single-band behavior, i.e., a linear function $\rho_H\ (B)$, although multiband-like behavior [nonlinear $\rho_H\ (B)$] was reported for $BiCh_2$-based compounds in previous studies [40, 86, 87]. Note that in the present work, I use single crystals, while in the previous experiments [40, 86, 87], the data were obtained on polycrystalline samples, which might cause some differences because there is large anisotropy between *ab*-plane and *c*-axis directions originating from the quasi-two-dimensional electronic state for $BiCh_2$-based compounds [30, 31] and polycrystalline samples have the two contributions. I determined the Hall coefficient R_{H} from the linear slope of R_{H} (B). R_{H} increases with decreasing temperature for $x = 0.2$ and 0.5. The increasing behavior is systematically depressed by increasing Se concentration, analogous to the ρ_{ab} (T) behavior in Figs. 9.1(a) and (b). For the $x = 0.2$ samples [Fig. 9.1(c)], sign changes of R_{H} from negative to positive are observed for $y = 0$, 0.24, 0.47, and 0.72. In contrast, a negative R_{H} is kept until 5 K for heavily Se-substituted $LaO_{0.8}F_{0.2}BiS_{0.95}Se_{1.05}$ ($x = 0.2$, $y = 1.05$), which indicates that electron-type carriers are dominant in the entire temperature region for this compound. For the $x = 0.5$ samples [Fig. 9.1(d)], the R_{H} (T) curves are similar to those for $x = 0.2$. However, heavily Se-substituted $LaO_{0.5}F_{0.5}BiS_{1.09}Se_{0.91}$ ($x = 0.5$, $y = 0.91$) shows a positive R_{H} throughout the entire temperature region, implying that hole-type carriers are predominant for that compound. According to the theoretical calculations for the FS topology of the $BiCh_2$-based system, the electron pockets around the X points exist up to $x \approx 0.45$, and hole pockets around the Γ and M points emerge above $x > 0.45$ [70, 71]. Therefore, the negative R_{H} (electron-type carriers) for $LaO_{0.8}F_{0.2}BiS_{0.95}Se_{1.05}$ and the positive R_{H} (hole-type carriers) for $x = 0.5$ in the low-temperature region

are in line with the theoretical work. However, the sign changes and the hole-type carriers at low temperatures observed for y = 0–0.72 in x = 0.2 are inconsistent with the theoretical expectations. A similar sign-change behavior of R_H was observed in polycrystalline $EuFBiS_2$, suggesting that CDW formation is related to the sign change [93]. In our experiments, the sign changes in R_H are observed, concomitant with the upward behavior of $\rho_{ab}(T)$, which is incompatible with a conventional CDW scenario by FS nesting. However, the nonmetallic behavior probably does not originate from a conventional band insulator since superconductivity is observed even when $\rho_{ab}(T)$ increases at low temperatures. In addition, a recent synchrotron radiation XRD study found the appearance of the superlattice reflections in a single-crystal sample of $LaO_{0.5}F_{0.5}BiS_2$ below $T \approx 260$ K and suggested that it is related to the CDW formation [92]. Moreover, the electrical resistivity of $LaO_{0.5}F_{0.5}BiS_2$ increases with decreasing temperature below $T \approx 260$ K [92]. I define similar temperatures as T_{min} in this study [see Figs. 9.1(a) and (b)]. Besides, there are several theoretical papers in which a CDW for the $BiCh_2$-based compounds is suggested [88, 89]. Thus, the sign changes in R_H for our crystals may relate to the CDW formation. Moreover, the sign-change temperature T^* progressively decreases, and the values of the positive R_H in the low-temperature regions are also systematically depressed with increasing Se concentration. Therefore, together with the results of the $\rho_{ab}(T)$ measurements, I speculate that the R_H data in the Se-free and moderately Se-substituted compounds with x = 0.2 point to carrier localization and that this may be linked to the CDW. For x = 0.5, the sign-change behavior is observed only for y = 0.19. Observing the sign change in the x = 0.5 case may be challenging since the hole-type carriers are basically predominant in the carrier-doping level. Alternatively, the temperature dependence of the Hall coefficients for x = 0.5 has almost the same tendency with increasing Se concentration as x = 0.2. Therefore, also considering that the possible CDW formation was observed for the x = 0.5 sample $LaO_{0.5}F_{0.5}BiS_2$ by the synchrotron XRD [92], I expect that the CDW might be present in the x = 0.5 samples as well. The carrier density n at low temperatures, estimated from $n = 1/|R_H e|$, changes from the order of 10^{19} cm^{-3} to 10^{21} cm^{-3} by Se substitution in x = 0.2 and from the order of 10^{19} cm^{-3} to 10^{20} cm^{-3} in x = 0.5.

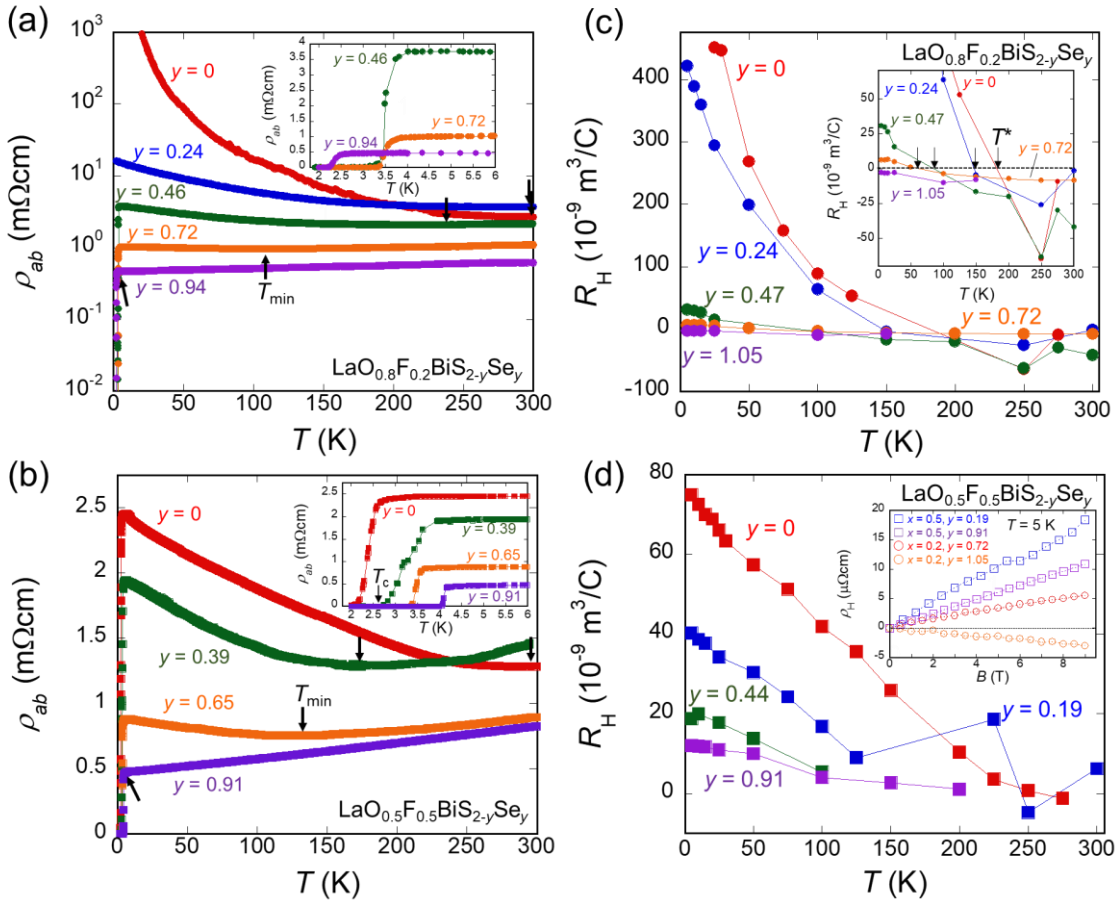

Fig. 9.1. (a,b) Temperature dependence of the electrical resistivity in the *ab*-plane, $\rho_{ab,}$ for (a) x = 0.2 (circles) and (b) x = 0.5 (squares), respectively. Different colors refer to the actual Se concentration, estimated from EDX. The arrows in (a) and (b) show T_{min}, where the normal-state resistivity above T = 5 K has a minimum. The insets in (a) and (b) represent the enlarged ρ_{ab} (T) curves around the superconducting transition. The superconducting transition temperature T_c is defined as the zero-resistivity temperature. (c,d) Temperature dependence of the Hall coefficient R_H for (c) x = 0.2 (circles) and (d) x = 0.5 (squares), respectively. The inset of (c) expresses the enlarged R_H (T) around the sign change. The arrows in the inset of (c) denote the sign-change temperature of the Hall coefficient. The inset of (d) shows the Hall resistivity ρ_H as a function of the magnetic field at T = 5 K for LaO$_{0.5}$F$_{0.5}$BiS$_{1.81}$Se$_{0.19}$ (open blue squares), LaO$_{0.5}$F$_{0.5}$BiS$_{1.09}$Se$_{0.91}$ (open purple squares), LaO$_{0.8}$F$_{0.2}$BiS$_{1.28}$Se$_{0.72}$ (open red circles), and LaO$_{0.8}$F$_{0.2}$BiS$_{0.95}$Se$_{1.05}$ (open orange circles). Note that we plot the x = 0.2 data to compare with x = 0.5, although figure (e) represents the Hall coefficient for x = 0.5.

9.3. Magnetization measurements

Next, I measured magnetization to estimate the shielding volume fractions for the $LaO_{1-x}F_xBiS_{2-y}Se_y$ samples. The magnetization measurements were performed by the Superconducting Quantum Interference Device (SQUID) magnetometer (MPMS 3, Quantum Design). Figures 9.2(a) and (b) show the temperature dependence of the magnetic susceptibility under H = 1 Oe for x = 0.2 and 0.5, respectively. The demagnetization factor N is large in this study since our single crystals have plate-like shapes, and the applied magnetic field is parallel to the c axis (perpendicular to the plate surface) [160, 161]. Thus, we corrected the diamagnetic signal by considering the demagnetization effect, and the estimated N is displayed in Table 9.1. The observed T_c is almost consistent with the resistivity measurements [see Figs. 9.1(a) and (b)]. The shielding fraction after demagnetization correction increase with increasing Se concentration [see Fig. 9.2(c)], which is comparable to the results obtained on polycrystals [154]. The magnetic susceptibility for $LaO_{0.8}F_{0.2}BiS_{1.28}Se_{0.72}$, $LaO_{0.5}F_{0.5}BiS_{1.35}Se_{0.65}$, and $LaO_{0.5}F_{0.5}BiS_{1.06}Se_{0.94}$ slightly exceeds the perfect diamagnetism ($4\pi\chi = -1$) probably because of the existence of tiny single crystals on the primary single-crystalline sample. These results demonstrate that the Se substitution is essential for bulk superconductivity to emerge, which may support the scenario that the Se substitution suppresses localization (see Sections 9.2 and 9.4).

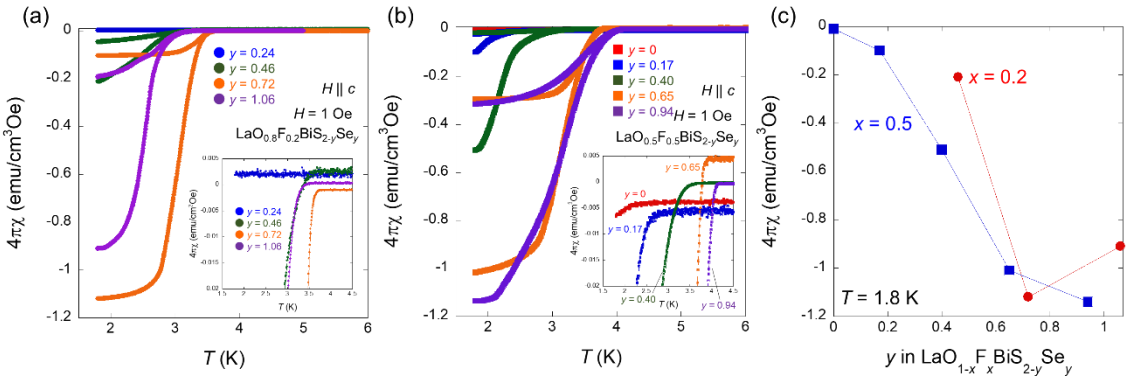

Fig. 9.2. Temperature dependence of the magnetic susceptibility after demagnetization correction for (a) x = 0.2 and (b) x = 0.5, respectively. The applied magnetic field is parallel to the c axis. Color difference denotes the actual Se concentration estimated from EDX. The insets of (a) and (b) show enlarged magnetic-susceptibility curves around the superconducting transition. (c) Magnetic susceptibility under the zero-field cooling at T = 1.8 K as a function of the Se concentration y for x = 0.2 (red circles) and x = 0.5 (blue squares).

Table 9.1. T_c, sample size, demagnetization factor N, and magnetic susceptibility of $LaO_{1-x}F_xBiS_{2-y}Se_y$. The Se concentration is estimated from the EDX.

Compounds	T_c from magnetization curve (K)	Sample size ($a \times b \times c$) (mm^3)	N	$4\pi\chi$ at $T = 1.8$ K
$LaO_{0.8}F_{0.2}BiS_{1.76}Se_{0.24}$	-	1.025 × 0.553 × 0.169	0.706	-
$LaO_{0.8}F_{0.2}BiS_{1.54}Se_{0.46}$	3.5	1.146 × 0.448 × 0.063	0.858	-0.21
$LaO_{0.8}F_{0.2}BiS_{1.28}Se_{0.72}$	3.7	1.132 × 1.812 × 0.126	0.849	-1.12
$LaO_{0.8}F_{0.2}BiS_{0.94}Se_{1.06}$	3.4	0.984 × 0.950 × 0.154	0.760	-0.91
$LaO_{0.5}F_{0.5}BiS_2$	2.2	0.919 × 0.867 × 0.149	0.752	-0.01
$LaO_{0.5}F_{0.5}BiS_{1.83}Se_{0.17}$	2.6	0.628 × 0.739 × 0.053	0.861	-0.1
$LaO_{0.5}F_{0.5}BiS_{1.61}Se_{0.39}$	3.4	1.292 × 1.472 × 0.109	0.858	-0.51
$LaO_{0.5}F_{0.5}BiS_{1.35}Se_{0.65}$	3.9	1.087 ×0.582 × 0.085	0.827	-1.01
$LaO_{0.5}F_{0.5}BiS_{1.06}Se_{0.94}$	4.1	1.038 × 1.158 × 0.062	0.892	-1.14

9.4. Magnetoresistance (MR)

To further investigate the localization behavior deduced from $\rho_{ab}(T)$ and $R_H(T)$, we performed MR measurements. If Anderson localization (WL) is realized in the $BiCh_2$-based systems, as suggested in a previous study [156], a negative MR should be observed in the localization regime [122, 123]. Figures 9.3(a)–(h) show the MR defined as $\mathrm{MR} = [\rho_{ab}(B) - \rho_{ab}(0)]/\rho_{ab}(0) \times 100\%$ as a function of magnetic field for $y = 0$ and 1.05 with $x = 0.2$, and $y = 0$ and 0.91 with $x = 0.5$, at $T = 5$ K and 7.5 K, respectively. The observed MR is clearly different from the negative MR expected from the Anderson localization (WL) scenario. The MR curves for the heavily Se-substituted compounds in $x = 0.2$ and 0.5 show sharp cusps in the low magnetic field at $T = 5$ K. The sharp dip of the MR in the low field is a characteristic feature of WAL, which has been observed in various materials with strong SOC (or spin-orbit scattering by strong spin-orbit coupled impurity) [119 and Chapter 4]. Indeed, the coefficient of determination R^2 for the quadratic fitting (classical MR) is relatively not good for the heavily Se-substituted samples. We display the results of the quadratic fittings in Table 9.2. That is consistent with the previous ARPES observation that SOC gives a pronounced effect on the band structure of $La(O,F)BiS_2$ [73]. The low-field MR curves for heavily F-doped and Se-free $LaO_{0.5}F_{0.5}BiS_2$ become broad and close to classical quadratic-field dependence. Moderately F-doped and Se-free $LaO_{0.8}F_{0.2}BiS_2$ exhibit an almost flat MR in low fields, which implies that a WAL-WL

crossover takes place. At T = 7.5 K, the WAL for the heavily Se-substituted samples with x = 0.2 and 0.5 is weakened. The MR curves for moderately Se-substituted $LaO_{0.5}F_{0.5}BiS_{1.35}Se_{0.65}$ (x = 0.5, y = 0.65) and $LaO_{0.8}F_{0.2}BiS_{1.28}Se_{0.72}$ (x = 0.2, y = 0.72) are displayed in Fig. 9.3 (a)–(h) as well. The MR behavior is probably positioned at the intermediate states of the Se-free and heavily Se-substituted samples, while there is uncertainty in both x = 0.2 and 0.5. However, the next magnetoconductance data, which are usually used to discuss the WAL and WL, clarify that the moderately Se-doped samples are in the intermediate states (I call *weak* WAL states in this study). To clearly exhibit the WAL, I correct the MR to the magnetoconductance ΔG (MC) defined as the $\Delta G\ (B) = G\ (B) - G\ (0)$. Figures 9.3(j)–(m) show the low-field MC as a function of the magnetic field at T = 5 K [Figs. 9.3(i) and (j)] and 7.5 K [Figs. 9.3(k) and (l)]. I show positive-field regions to analyze the MC data. I have analyzed the low-temperature data only at T = 5.0 K and 7.5 K since the low-filed MR at higher-temperature regions becomes broad and close to flat on the magnetic fields for all samples [see Fig. 9.4]. Basically, the 2D MC of the WAL contribution is described by the Hikami-Larkin-Nagaoka (HLN) formula [124]. To quantitatively analyze the MC curves and compare them with previous studies of WAL, I fit the data with the 2D HLN formula (Eq. 4.3). The solid lines in Figs. 9.3(i)–(l) represent the HLN fitting. The HLN model can fit the MC data well except for $LaO_{0.8}F_{0.2}BiS_2$ at T = 7.5 K [red solid line in Fig. 9.3(k)]. The coefficient of determination R^2 for this compound is less than 80% despite over 95% for the others [see Table. 9.3]. That is probably due to the WAL-WL crossover state. The obtained values of α and l_ϕ are displayed in Figs. 9.7(c), (d), and Table 9.3. The magnitudes of α are in the order of 10^4, except for $LaO_{0.8}F_{0.2}BiS_2$, which is much larger than reported for 2D compounds [126–128]. Such tremendous values of α have been observed in 3D bulk systems and are considered to derive from the 3D bulk contribution (a large number of conducting channels) [138, 162–164]. Thus, I speculate that the large values of α in our systems are due to the 3D bulk nature of the single crystals. In this study, we use the HLN model only to quantitatively investigate the change of the MC behavior by the elemental-substitution effect. The obtained l_ϕ is comparable to the values found in previous studies for both 2D and 3D bulk compounds [126–128, 138, 162–164]. The absolute values of α and l_ϕ systematically increase with increasing Se concentration [see Figs. 9.7(c) and (d)], which indicates that the WAL behavior emerges by Se substitution. Furthermore, the order of α for $LaO_{0.8}F_{0.2}BiS_2$ is 10^4 times smaller than in the other samples [see Table 9.3], which implies that this compound is in the WAL-WL crossover states. A similar evolution of α by doping was observed for $Bi_{2-x}Cr_xSe_3$, and the sign-change behavior of α from negative to positive was regarded as the crossover from WAL to WL [126]. I also performed the HLN fitting for lower-field (up to B = 0.2 T) MC data (see Fig. 9.5 and Table 9.4). The change of α and l_ϕ by Se substitution is the same tendency as the HLN fitting up to B = 1 T in Figs. 9.3(i)–(l). Thus, I expect that the change from the WAL to weak WAL (almost quadratic MR) and WAL-WL crossover can be controlled by the elemental substitution of F and Se in the $BiCh_2$-based system and that the localization states observed in $\rho_{ab}\ (T)$ and $R_H\ (T)$

[Figs. 9.1(a)–(d)] can be associated with the MC behavior.

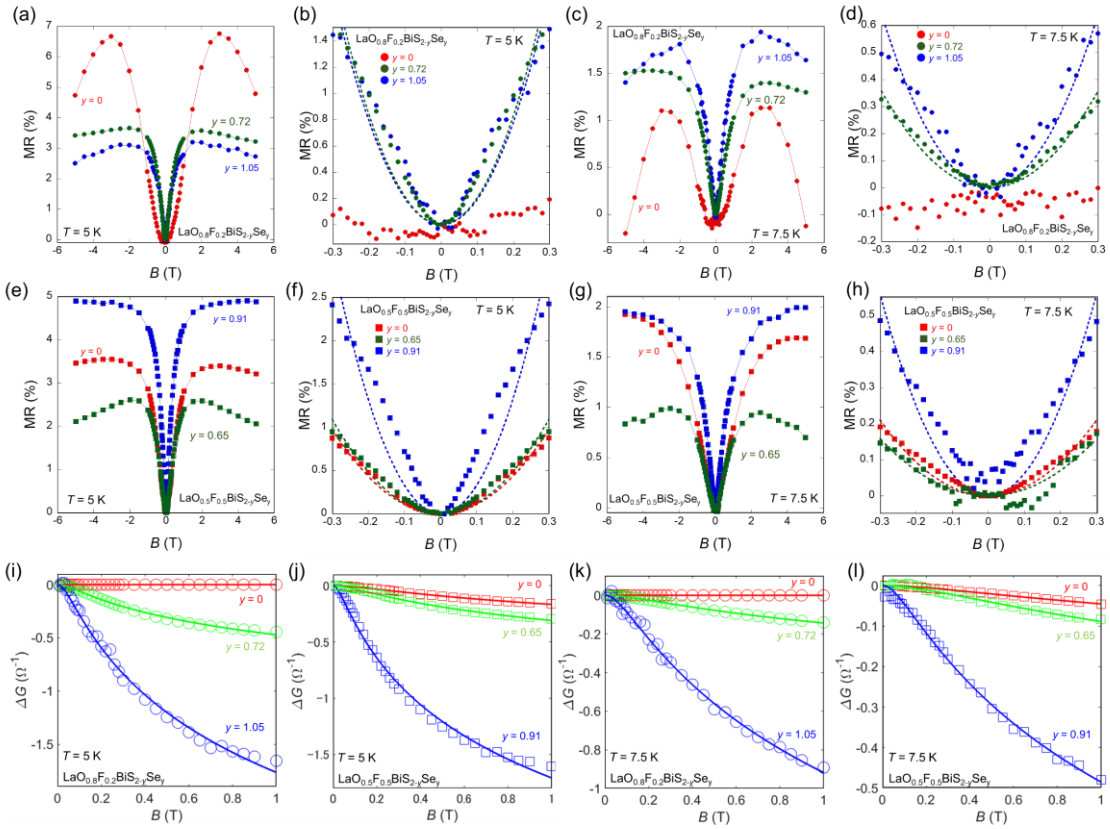

Fig. 9.3. (a) MR for $y = 0$ (red circles), $y = 0.72$ (green circles), $y = 1.05$ (blue circles) with $x = 0.2$ at $T = 5$ K. (b) The enlarged MR curves in the low-field region at $T = 5.0$ K. (c) and (d) show the MR for $x = 0.2$ at $T = 7.5$ K. (e–h) MR data for $x = 0.5$. Dotted lines in (b), (d), (f), and (h) show the quadratic in B fits. (i–l) MC at $T = 5$ K for (i) $x = 2$ (open circles) and (j) $x = 0.5$ (open squares), respectively. Solid lines represent the fits with the HLN model (Eq. 4.3). (k) and (l) express the MC at $T = 7.5$ K. The color variation expresses the actual Se concentration as listed, estimated from the EDX results.

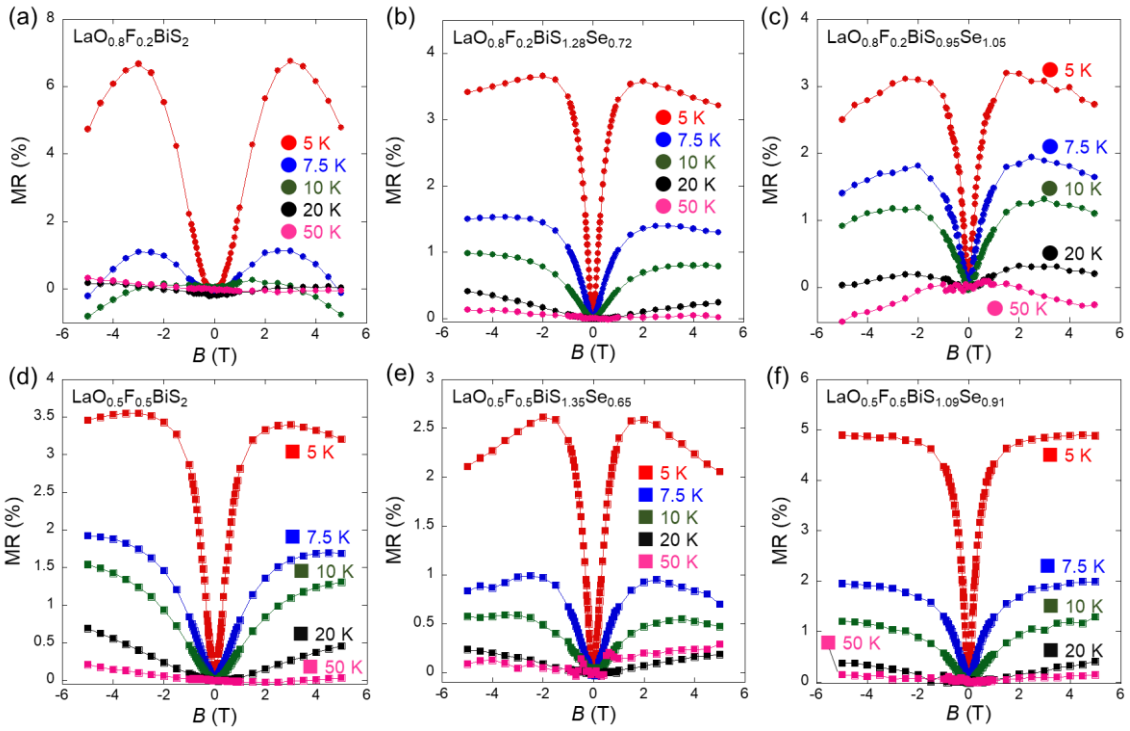

Fig. 9.4. MR at various temperatures for (a) $LaO_{0.8}F_{0.2}BiS_2$, (b) $LaO_{0.8}F_{0.2}BiS_{1.28}Se_{0.72}$, (c) $LaO_{0.8}F_{0.2}BiS_{0.95}Se_{1.05}$, (d) $LaO_{0.5}F_{0.5}BiS_2$, (e) $LaO_{0.5}F_{0.5}BiS_{1.35}Se_{0.65}$, and (f) $LaO_{0.5}F_{0.5}BiS_{1.09}Se_{0.91}$ from T = 50 K to 5 K. The Se concentration is estimated from the EDX.

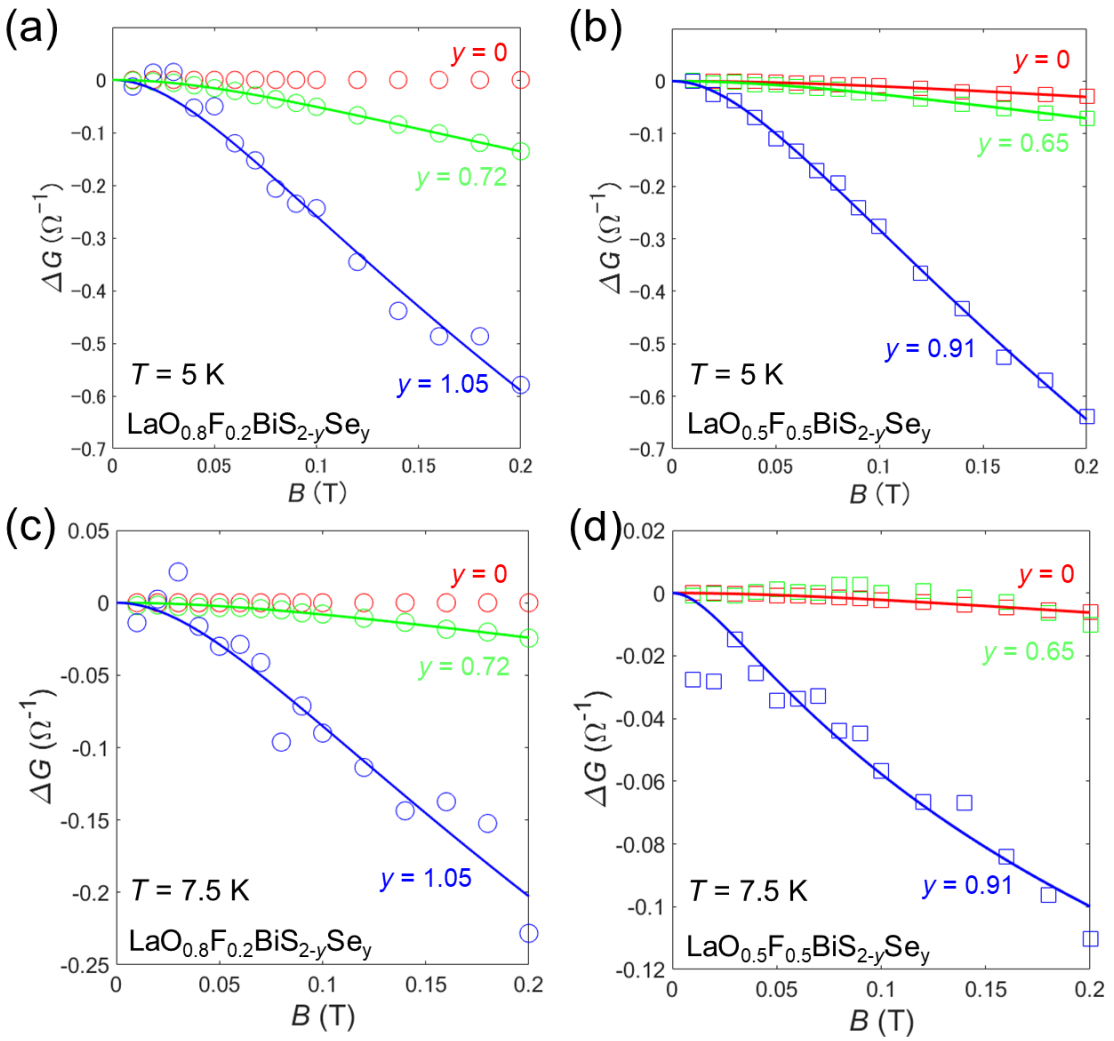

Fig.9.5. MC up to B = 0.2 T at T = 5 K for (a) x = 0.2 (open circles) and (b) x = 0.5 (open squares), respectively. Solid lines represent the fits with the HLN model (Eq. 4.3 in the main text). (c) and (d) express the MC at T = 7.5 K. The color variation expresses the actual Se concentration as listed, estimated from the EDX results.

Table 9.2. Coefficient A and coefficient of determination R^2 for the quadratic fitting (MR = AB^2) for $LaO_{1-x}F_xBiS_{2-y}Se_y$ at T = 5 K and 7.5 K. The Se concentration is estimated from the EDX.

Compounds	Temperature (K)	A (T^{-2})	R^2
$LaO_{0.8}F_{0.2}BiS_2$	-	-	-
$LaO_{0.8}F_{0.2}BiS_{1.28}Se_{0.72}$	5	20.9	0.927
$LaO_{0.8}F_{0.2}BiS_{0.95}Se_{1.05}$	5	19.6	0.854
$LaO_{0.5}F_{0.5}BiS_2$	5	10.8	0.958
$LaO_{0.5}F_{0.5}BiS_{1.35}Se_{0.65}$	5	12.1	0.957
$LaO_{0.5}F_{0.5}BiS_{1.09}Se_{0.91}$	5	33.0	0.844
$LaO_{0.8}F_{0.2}BiS_2$	-	-	-
$LaO_{0.8}F_{0.2}BiS_{1.28}Se_{0.72}$	7.5	4.0	0.958
$LaO_{0.8}F_{0.2}BiS_{0.95}Se_{1.05}$	7.5	7.1	0.896
$LaO_{0.5}F_{0.5}BiS_2$	7.5	2.3	0.940
$LaO_{0.5}F_{0.5}BiS_{1.35}Se_{0.65}$	7.5	1.8	0.862
$LaO_{0.5}F_{0.5}BiS_{1.09}Se_{0.91}$	7.5	6.2	0.833

Table 9.3. HLN parameters α and phase coherence length l_ϕ and coefficient of determination R^2 in the HLN fitting for $LaO_{1-x}F_xBiS_{2-y}Se_y$ at T = 5 K and 7.5 K up to B = 1 T. The Se concentration is estimated from the EDX.

Compounds	Temperature (K)	α (x10^4)	l_ϕ (nm)	R^2
$LaO_{0.8}F_{0.2}BiS_2$	5	-0.000968±0.000791	25.3±7.6	0.953
$LaO_{0.8}F_{0.2}BiS_{1.28}Se_{0.72}$	5	-2.38±0.16	70.7±3.6	0.996
$LaO_{0.8}F_{0.2}BiS_{0.95}Se_{1.05}$	5	-7.85±0.57	80.2±4.6	0.994
$LaO_{0.5}F_{0.5}BiS_2$	5	-1.40±0.08	46.9±1.6	0.998
$LaO_{0.5}F_{0.5}BiS_{1.35}Se_{0.65}$	5	-1.92±0.13	58.8±2.6	0.997
$LaO_{0.5}F_{0.5}BiS_{1.09}Se_{0.91}$	5	-6.72±0.44	91.5±5.1	0.995
$LaO_{0.8}F_{0.2}BiS_2$	7.5	-0.00020±0.015	14.3±30.3	0.752
$LaO_{0.8}F_{0.2}BiS_{1.28}Se_{0.72}$	7.5	-1.29±0.05	45.0±1.0	0.999
$LaO_{0.8}F_{0.2}BiS_{0.95}Se_{1.05}$	7.5	-5.73±0.40	58.7±2.7	0.997
$LaO_{0.5}F_{0.5}BiS_2$	7.5	-0.67±0.06	33.7±0.1	0.995
$LaO_{0.5}F_{0.5}BiS_{1.35}Se_{0.65}$	7.5	-1.28±0.33	34.3±4.1	0.985
$LaO_{0.5}F_{0.5}BiS_{1.09}Se_{0.9}$	7.5	-3.09±0.26	57.9±3.1	0.998

Table 9.4. HLN parameters α and phase coherence length l_ϕ and coefficient of determination R^2 for the HLN fitting for $LaO_{1-x}F_xBiS_{2-y}Se_y$ at T = 5 K and 7.5 K up to B = 0.2 T. The Se concentration is estimated from the EDX.

Compounds	Temperature (K)	α (x10^4)	l_ϕ (nm)	R^2
$LaO_{0.8}F_{0.2}BiS_2$	5	-	-	-
$LaO_{0.8}F_{0.2}BiS_{1.28}Se_{0.72}$	5	-4.01±0.22	55.3±1.1	0.999
$LaO_{0.8}F_{0.2}BiS_{0.95}Se_{1.05}$	5	-10.13±4.48	70.2±13.3	0.981
$LaO_{0.5}F_{0.5}BiS_2$	5	-1.68±1.34	43.7±11.1	0.986
$LaO_{0.5}F_{0.5}BiS_{1.35}Se_{0.65}$	5	-2.78±0.63	49.6±3.86	0.998
$LaO_{0.5}F_{0.5}BiS_{1.09}Se_{0.91}$	5	-11.05±1.31	70.2±3.54	0.999
$LaO_{0.8}F_{0.2}BiS_2$	7.5	-	-	-
$LaO_{0.8}F_{0.2}BiS_{1.28}Se_{0.72}$	7.5	-1.15±0.84	46.2±11.1	0.983
$LaO_{0.8}F_{0.2}BiS_{0.95}Se_{1.05}$	7.5	-4.02±3.75	65.5±30.0	0.931
$LaO_{0.5}F_{0.5}BiS_2$	7.5	-0.25±0.03	49.3±2.3	0.999
$LaO_{0.5}F_{0.5}BiS_{1.35}Se_{0.65}$	7.5	-	-	-
$LaO_{0.5}F_{0.5}BiS_{1.09}Se_{0.91}$	7.5	-0.74±0.44	115.2±41.5	0.869

9.5. Electronic band structure

I have analyzed the data with the HLN model, but a recent theoretical calculation about the WAL may be useful for our experimental results. The theoretical work which considered the strong SOC in the atoms that constitute the lattice (denoted as SOC lattice in Ref. 165) suggested that the WAL-WL crossover is realized by adjusting the ratio of the Fermi energy E_F to the band gap E_g [165]. In the $BiCh_2$-based system, several electronic-band calculations suggest that E_g decreases by Se substitution [35, 166]. Since the F substitution causes electron-carrier doping, the elemental-substitution effect of Se and F leads to controlling E_F and E_g in the $BiCh_2$-based system, which may contribute to the change of the MC. Moreover, the predicted G (B) for the $Bi_{1-x}Sb_x$ alloy [165], in which E_F of semi-metallic Bi can be changed by Sb substitution, is similar to the observed MC [Figs. 9.3(j)–(m)].To confirm the scenario on the changes of the MC behavior by controlling E_F and E_g by Se substitution, we investigate the electronic band structures. Figures 9.6(a) and (b) exhibit the calculated electronic band structures for Se-free $LaO_{0.5}F_{0.5}BiS_2$ and heavily Se-substituted $LaO_{0.5}F_{0.5}BiSSe$. The band gap at the X point clearly decreases with Se substitution. Moreover, Figs. 9.6(c) and (d) show the ARPES spectra for our single crystals of Se-free $LaO_{0.5}F_{0.5}BiS_2$ and heavily Se-substituted $LaO_{0.5}F_{0.5}BiSSe$. The observed band gap values at the X point were estimated to be 0.875 eV for Se-free $LaO_{0.5}F_{0.5}BiS_2$ and 0.715 eV for heavily Se-substituted $LaO_{0.5}F_{0.5}BiSSe$. The tendency of the band gap change observed in ARPES is consistent with the theoretical calculations. In addition, the spectral intensity at E_F of Se-free $LaO_{0.5}F_{0.5}BiS_2$ is strongly reduced compared to that of heavily Se-substituted $LaO_{0.5}F_{0.5}BiSSe$ [see Fig. 9.6(e)], which is consistent with the localized and non-localized nature of the samples. Thus, the

electronic band structures from the theoretical calculations and ARPES support the results of the transport properties.

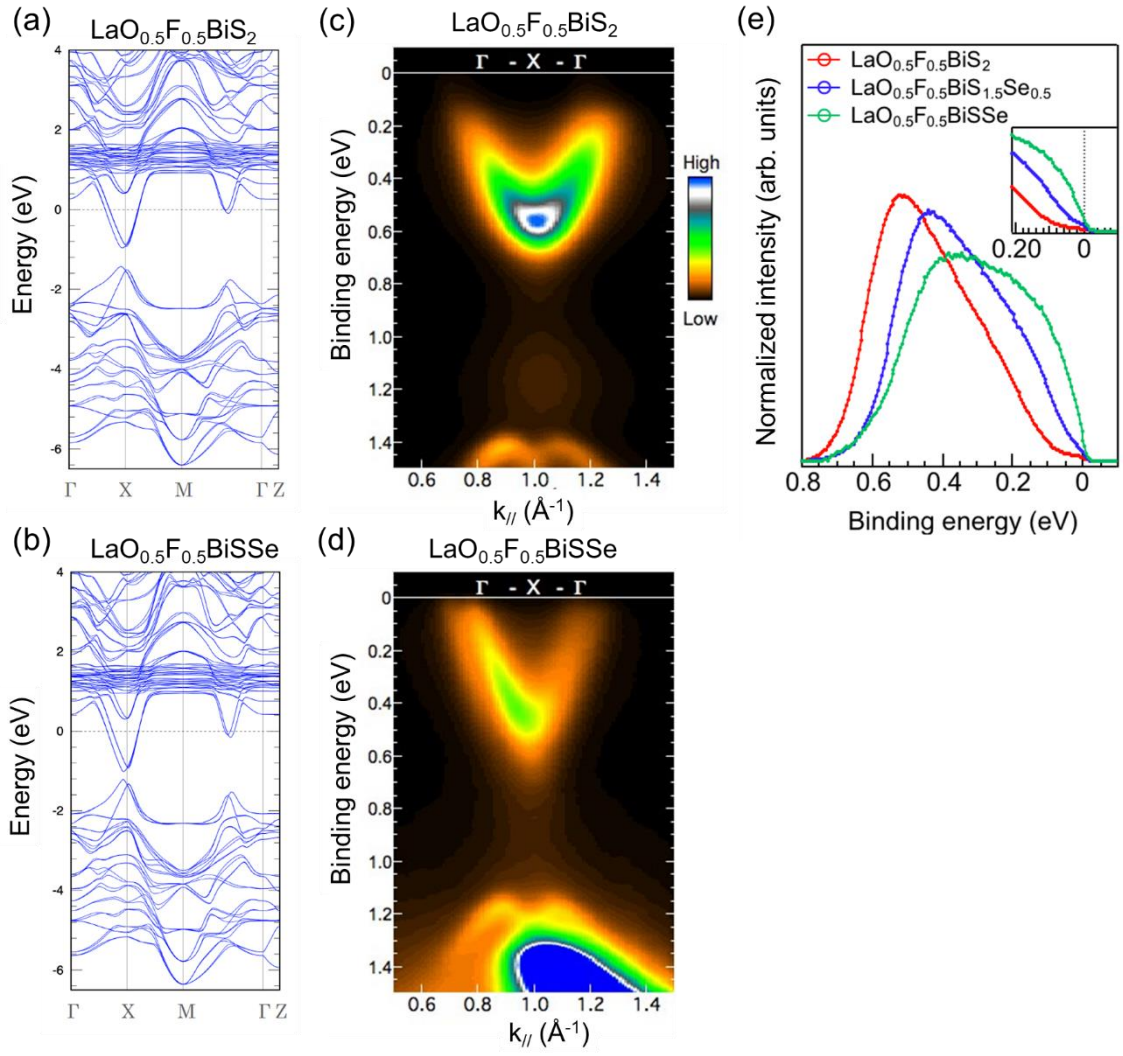

Fig. 9.6. Electronic band structures. (a,b) Calculated band structures of (a) $LaO_{0.5}F_{0.5}BiS_2$ (x = 0.5, y = 0) and (b) $LaO_{0.5}F_{0.5}BiSSe$ (x = 0.5, y = 1). (c,d) ARPES spectra for the single crystals of (c) $LaO_{0.5}F_{0.5}BiS_2$ (x = 0.5, y = 0) and (d) $LaO_{0.5}F_{0.5}BiSSe$ (x = 0.5, y = 1). (e) Comparison of the k-integrated spectra near E_F for the electron pocket at X between $LaO_{0.5}F_{0.5}BiS_2$, $LaO_{0.5}F_{0.5}BiS_{1.5}Se_{0.5}$, and $LaO_{0.5}F_{0.5}BiSSe$. The Se concentration for the ARPES results is given by its nominal value. The inset of (e) shows an expanded view of the E_F region. The spectra were normalized by area after subtracting the Shirley background [167, 168].

9.6. Clear maximum of MR

Next, I discuss an apparent maximum of the MR for moderately F-doped and Se-free $LaO_{0.8}F_{0.2}BiS_2$. The theoretical calculation suggested that there is no minimum of ΔG (B) (no maximum of the MR) as a function of the field in the SOC lattice, while a clear minimum of the ΔG (B) (maximum of the MR) is observed in conventional HLN theory, which considers a 2D system with strong spin-orbit coupled impurities (disordered 2D system) [165]. I have not found any specific impurities in my single crystal samples (I confirmed that the actual atomic ratios are almost consistent with the nominal values, although I cannot wholly determine that there are no impurities). However, moderately F-doped and Se-free $LaO_{0.8}F_{0.2}BiS_2$ probably have a disorder originating from local crystal distortions caused by structural instability due to the presence of Bi lone pairs [31]. The crystal structure of the parent compound has a monoclinic symmetry ($P2_1/m$, No. 11) [36, 37], and the tetragonal structure ($P4/nmm$, No.129) is gradually stabilized by the F substitution (electron-carrier doping) [38, 39, and Chapter 8]. Moreover, the Se-substitution effect causes the depression of the local disorder in the BiCh1 plane [37, 54]. Thus, moderately F-doped and Se-free $LaO_{0.8}F_{0.2}BiS_2$ still have local distortions, which may lead to the clear maximum of the MR. Furthermore, the temperature dependence of the resistivity for $LaO_{0.8}F_{0.2}BiS_2$ follows variable range hopping (VRH) in a relatively wide temperature region (see Fig. 16.4), which indicates the presence of disorder. On the basis of the discussion here, I propose that the $BiCh_2$-based $LaO_{1-x}F_xBiS_{2-y}Se_y$ compounds provide a new platform where the WAL states may be realized when the structural disorder is removed by Se substitution [the behavior of VRH is also suppressed by Se substitution (see Fig. 16.4)].

9.7. Electronic phase diagram

In Figs. 9.7(a) and (b), I summarize the electronic phases of $LaO_{0.8}F_{0.2}BiS_{2-y}Se_y$ and $LaO_{0.5}F_{0.5}BiS_{2-y}Se_y$ as functions of y and temperature. For x = 0.2 [Fig. 9.7(a)], the $\rho_{ab}(T)$ behavior for y = 0 demonstrates an insulating behavior in the entire temperature region [blue region in Fig. 9.7(a)]. The insulating behavior is gradually suppressed with increasing Se concentration, and superconductivity emerges for y = 0.46, 0.72, and 0.94, although the weak increase in $\rho_{ab}(T)$ is still observed for y = 0.46 and 0.72 (denoted as Weakly insulating in Fig. 9.7). There is no strong correlation between y and T_c in x = 0.2. When the Se-substitution level reaches y = 0.94, the $\rho_{ab}(T)$ curve exhibits the metallic behavior in the whole-temperature region (yellow regions in Fig. 9.7). The T_{min} and T^* (the definition is described in the caption of Fig. 9.7) progressively decline with increasing Se concentration, and the sign change disappears for y = 1.05, which indicates that the Se substitution suppresses the localization state. The normalized resistivity ρ_{ab} (5 K)/ ρ_{ab} (295 K) and the Hall coefficients at T = 5 K and 100 K systematically decrease with increasing Se concentration, as shown in Figs. 9.7(c) and (d). The magnitude of α and l_ϕ in the HLN model increases with increasing Se concentration, which implies

that the WAL state emerges for y = 1.05 [denoted as WAL in Fig. 9.7(a) because of the largest α in the x = 0.2 samples], and it is weakened for y = 0.72 [denoted as *Weak* WAL in Fig. 9.7(a) because of the intermediate value of α between y = 0 and 1.05]. Furthermore, the absolute value of α for Se-free $LaO_{0.8}F_{0.2}BiS_2$ is much smaller than the others, indicating that the crossover state is realized. The electronic phase diagram for x = 0.5 [Fig. 9.7(b)] is similar to the one for x = 0.2; however, y = 0 in the x = 0.5 case presents superconductivity at $T \approx 2$ K, although ρ_{ab} (T) exhibits a weakly insulating behavior. The largest absolute values of α and l_ϕ for y = 0.91 in the x = 0.5 samples imply the WAL characteristics [see Fig. 9.7(d)]. The WAL is diminished for $LaO_{0.5}F_{0.5}BiS_{1.35}Se_{0.65}$ and $LaO_{0.5}F_{0.5}BiS_2$ [denoted as *Weak* WAL in Fig. 4(b) because of the intermediate values of α between $LaO_{0.8}F_{0.2}BiS_2$ and heavily Se-substituted samples]. Therefore, the change of the MC behavior by the F and Se substitution is associated with the ρ_{ab} (T) behavior for both x = 0.2 and 0.5. The T_c for x = 0.5 monotonically increases with increasing Se concentration, which is different from the x = 0.2 case. The distinct behavior may originate from the FS topology since theoretical studies propose that the superconducting gap structure and the T_c change with the transition from the electron-pocket FSs (x < 0.45) around the X points to hole-pocket FSs (x > 0.45) around the Γ and M points [72]. The localization state [blue regions and green regions in Figs. 9.7(a) and (b)] may relate to the CDW as discussed in Section 9.2, although I cannot completely determine the transition temperature of the CDW formation. However, I believe that the T_{min} or T^* may be related to the CDW formation because synchrotron XRD observed superlattice reflections below a similar temperature to the T_{min} in the previous study [92].

In conclusion, I have investigated the transport properties of the $BiCh_2$-based system $LaO_{1-x}F_xBiS_{2-y}Se_y$ (x = 0.2 and 0.5, y = 0–1.05). The ρ_{ab} (T) behavior and R_H (T) suggest the existence of unique localization states. The localization behavior is systematically depressed with increasing Se concentration. MR measurements indicate that WAL is realized in the heavily Se-substituted systems. The WAL behavior is weakened by the changes in F and Se concentrations. A crossover state of WAL and WL may emerge around moderately F-doped and Se-free $LaO_{0.8}F_{0.2}BiS_2$. The change of the MC behavior by the F and Se substitution clearly correlates with the results of ρ_{ab} (T) and R_H (T). Moreover, the localization regions are possibly associated with the CDW. Based on the results shown here, I propose that the $BiCh_2$-based system is an excellent platform to study unique localization states, electronic ordering, and superconductivity by using the elemental substitution with bulk single crystals.

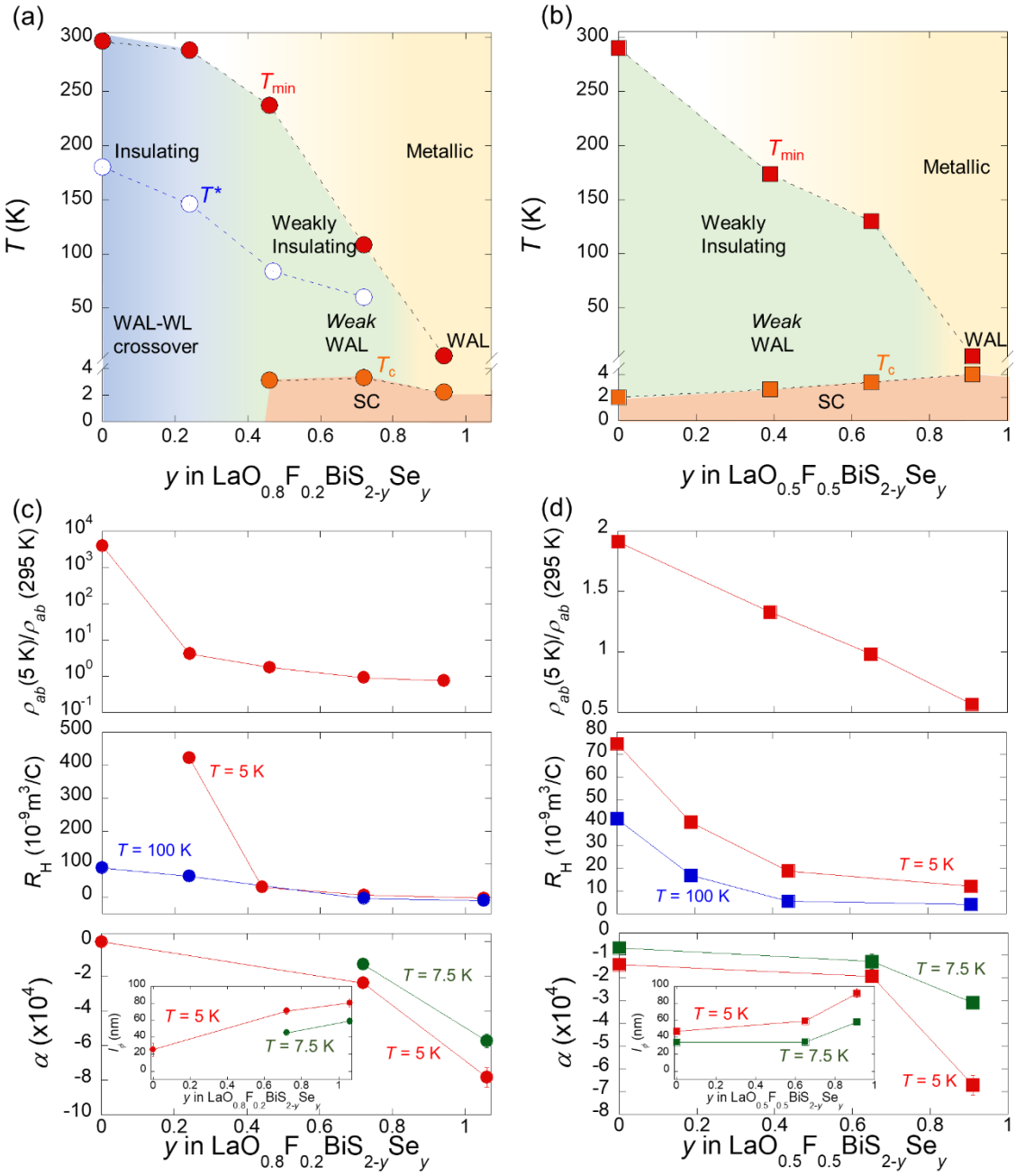

Fig. 9.7. Electronic phase diagrams for (a) x = 0.2 and (b) x = 0.5. T_{min} (filled red circles) represents the temperature at which the $\rho_{ab}(T)$ above T = 5 K (in the normal states) has a minimum. T* (open blue circles) and T_c (filled orange circles) exhibit the sign-change temperature in the Hall coefficient and superconducting transition temperature (zero resistivity). T* for x = 0.5 is not displayed in Fig. 9.5(b) since the sign change is only observed for y = 0.19. Blue, green, yellow, and orange regions express the insulating, weakly insulating, metallic, and superconducting (denoted as SC) states, respectively. We depict the WAL-WL crossover, *Weak* WAL, and WAL in (a) and (b) by referring to the results of the MC. (c,d) Se concentration y dependence of the ρ_{ab} (5 K)/ρ_{ab} (295 K), Hall coefficients at T = 5 K

(red) and 100 K (blue), and α and l_ϕ [the inset in (c) and (d)] in the HLN model (Eq. 4.3) at T = 5 K (red) and 7.5 K (green) for (c) x = 0.2 (circles) and (d) x = 0.5 (squares), respectively.

10. Extremely high upper critical field

10.1. Local inversion symmetry breaking in the $BiCh_2$ layer

The F-doped (electron-carrier-doped) $BiCh_2$-based superconductor possesses a centrosymmetric crystal structure of tetragonal *P*4/*nmm* (No. 129, D_{4h}), as introduced in Chapter 8, while the $BiCh_2$ layer lacks the inversion symmetry with the C_{4v} site point group of Bi and Ch sites. Theoretical studies predicted that hidden spin polarization by local RSOI should exist in the $REOBiCh_2$ system [152, 166]. The spin polarization attributed to the local inversion symmetry breaking in the $BiCh_2$ layer was observed by spin-ARPES (SARPES) for $LaO_{0.55}F_{0.45}BiS_2$ [153]. Especially it has been suggested that the Rashba-type spin polarization is realized near the Fermi level. Furthermore, the observed in-plane B_{c2} for $LaO_{0.5}F_{0.5}BiS_2$ largely exceeds the Pauli limit, which may imply that the local inversion asymmetry, i.e., the RSOI, can play a significant role in superconductivity [155]. The orbital pair-breaking effect can be suppressed in the magnetic field parallel to the *ab*-plane under the layered system and the quasi-2D electronic states (see Chapter 3). However, research focused on local inversion asymmetry has not been extensively developed in $BiCh_2$-based compounds. That justifies a study to address the influence of the local inversion asymmetry in $BiCh_2$-based systems on the superconducting nature by investigating the upper critical fields. In the $BiCh_2$-based superconductors, I selected $LaO_{0.5}F_{0.5}BiS_{2-y}Se_y$ (y = 0.22 and 0.69) as the target materials to purely investigate the superconducting properties because the compounds do not contain *f*-electron elements in the REO blocking layer. Figure 10.1 shows the crystal structure of the target system $LaO_{0.5}F_{0.5}BiS_{2-y}Se_y$ (y = 0.22 and 0.69), which has a layered structure composed of the LaO blocking layers and $BiCh_2$ conducting layers. Although the crystal structure possesses global inversion symmetry (the symbol indicated with P in Fig. 10.1 shows the global inversion center), the inversion symmetry is locally broken in each $BiCh_2$ layer (dashed rectangles show each $BiCh_2$ layer in Fig. 10.1). A partial Se substitution for the in-plane S site (Ch1 site) leads to the enhancement of the bulk nature of superconductivity [154 and Chapter 9], and a specific heat jump is clearly observed [65]. The in-plane chemical pressure effect and carrier concentration have been revealed to be essential for the emergence of bulk superconductivity in the $REOBiCh_2$ system [31 and Chapter 2]. The Se concentration y was estimated using EDX. The actual atomic ratio is almost consistent with the nominal value. I have investigated upper critical fields for the compounds by the resistivity measurements under magnetic fields.

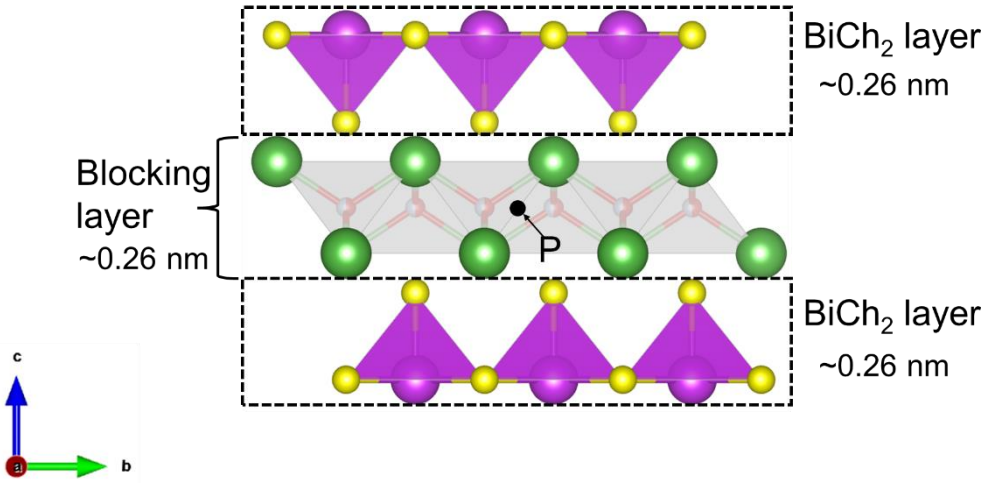

Fig. 10.1. Two $BiCh_2$ layers and LaO blocking layer. The inversion symmetry is locally broken in each $BiCh_2$ layer. The symbol P in the LaO blocking layer denotes the global inversion center for the $LaO_{0.5}F_{0.5}BiS_{2-y}Se_y$ system. The thicknesses of the $BiCh_2$ and blocking layers were evaluated as the length between the centers of the two atomics by structural analysis of powder X-ray diffraction.

10.2. Temperature dependence of the *ab*-plane resistivity under magnetic fields

The resistivity measurements in a static field up to 9 T and 2 K were performed using a PPMS with a horizontal rotator probe. Pulsed magnetic field measurements were performed at the Institute for Solid State Physics (ISSP) at the University of Tokyo. Figure 10.2 shows the temperature dependence of the in-plane resistivity ρ_{ab} at a field strength of the zero field for $LaO_{0.5}F_{0.5}BiS_{2-y}Se_y$ (y = 0.22 and 0.69). The T_c defined as the midpoint (zero resistivity) of the transition is 3.18 K (3.0 K) and 4.18 K (3.95 K) for y = 0.22 and y = 0.69 to compare the data with the magnetic field. The higher Se concentration causes higher T_c in the carrier-doping level of x = 0.5 (see Chapter 9). A weak increase in the resistivity was observed in low-temperature regions. The Se substitution suppresses the weak increase. The reason for the weak increase and the suppression by the Se substitution is discussed in Chapter 9 in detail.

Figures 10.3(a) and (b) show the temperature dependence of the in-plane resistivity ρ_{ab} for y = 0.22 at various fields parallel to the *ab* plane and *c* axis. The applied electric current was perpendicular to the magnetic field in $B \parallel c$ and parallel in $B \parallel ab$. In the case of $B \parallel c$, the superconducting states are immediately suppressed by the applied field. In contrast, in the case of $B \parallel ab$, the superconductivity is robust against the applied field. Figures 10.3(c) and (d) exhibit the field dependence of the ρ_{ab} for y = 0.22 from 3.0 to 2.0 K with $B \parallel ab$ and $B \parallel c$. The ρ_{ab} (B) data [Figs. 10.3(c) and (d)] show a trend similar to ρ_{ab} (T). Figures 10.3(e)–(h) show the y = 0.69 data. The behaviors of both ρ_{ab} (T) and ρ_{ab} (B) are similar to that of y = 0.22. For y = 0.69 with $B \parallel ab$, zero resistivity is retained up to 9 T

for temperatures below 2.6 K. The temperature and field dependencies of ρ_{ab} show a sizeable anisotropic factor $\gamma_{SC} = B_{c2}^{ab}/B_{c2}^{c}$ [see Figs. 10.8(c) and (d)], indicating that the superconductors have strong anisotropic (quasi-2D) superconducting characteristics [44, 45]. The upper critical fields were estimated from the midpoint of the resistive transition of the ρ_{ab} (B) data; a similar criterion has been used in several studies [101, 102, 108, 109, 155]. Moreover, I plotted the B_{c2} defined as the beginning of the resistive increase from zero resistivity (zero-resistivity criteria) of the ρ_{ab} (B) data and from the ρ_{ab} (T) data, in Figs. 10.5(c)–(f). The B_{c2} (T) behavior estimated from the ρ_{ab} (T) curves [Figs. 10.5(e) and (f)] almost consistent with the values from ρ_{ab} (B) data.

To investigate the in-plane B_{c2} variation at higher fields, we measured the field dependence of ρ_{ab} for y = 0.22 and 0.69 based on the use of pulsed high fields up to 55 T. Figures 10.4(a) and (b) show the ρ_{ab} (B) data acquired by the pulsed fields parallel to the *ab* plane from 4.2 K to ~0.47 K for y = 0.22 and 0.69, respectively. Notably, the superconducting states are not completely destroyed up to 55 T at ~ 0.47 K for both y = 0.22 and 0.69. Moreover, for y = 0.69, the superconducting states survive at the highest field of 55 T, even at 1.39 K. The gradient of the ρ_{ab} (B) curves from zero resistivity to the normal state became smaller in the low-temperature and high-field regions for both samples. I define the normal state resistivity ρ_n as the black dashed lines in Figs. 10.4(a) and (b) because it is not primarily changed by the scanning field. Thus, the magnitude of B_{c2} was estimated from the midpoint of zero resistivity and ρ_n. I also plotted the B_{c2} defined as the beginning of the resistive increase from zero resistivity (zero-resistivity criteria) of the ρ_{ab} (B) curves by the pulsed field [see Figs. 10.5 (c) and (d)].

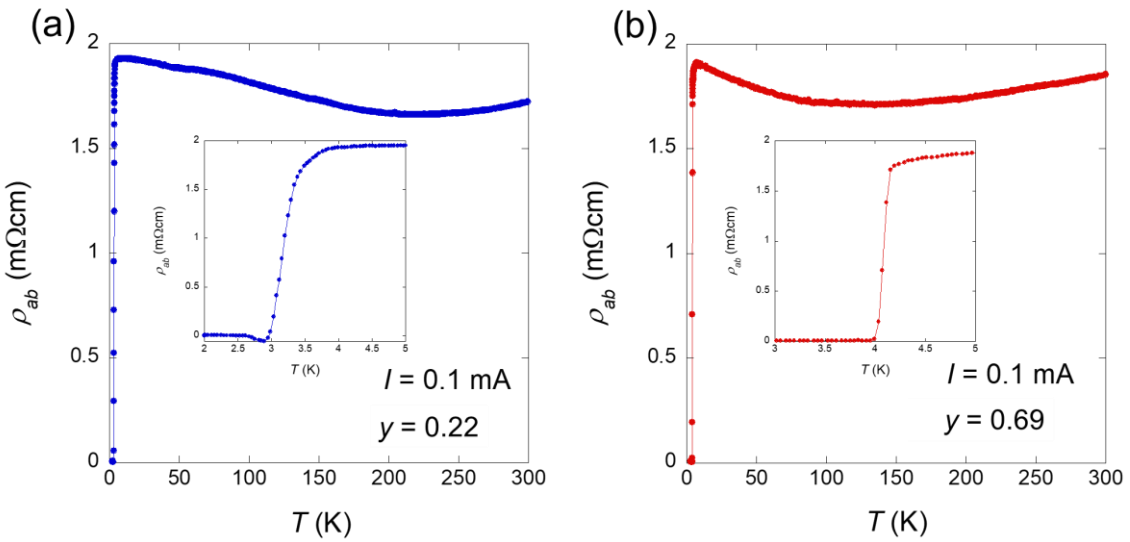

Fig. 10.2. Temperature dependence of the resistivity in the absence of a magnetic field for (a) y = 0.22 and (b) y = 0.69. The insets show the enlarged resistivity curves near the superconducting transition. The superconducting transition temperature, T_c, is defined as the midpoint (zero resistivity) of the

resistive transition and was observed at T_c = 3.18 K (3.0 K) and 4.08 K (3.95 K).

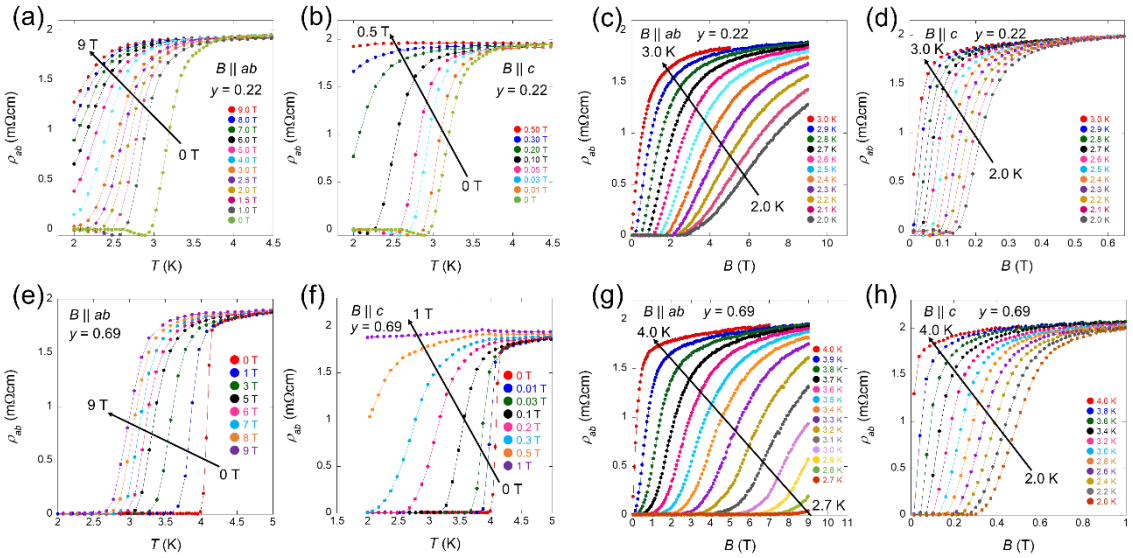

Fig. 10.3. In-plane resistivity ρ_{ab} for x = 0.22 and 0.69 in magnetic fields. (a,b) Temperature dependence of the in-plane resistivity ρ_{ab} in magnetic fields for y = 0.22 in (a) $B \parallel ab$ and (b) $B \parallel c$. The arrows denote the direction from low to high fields. (c,d) Field dependence of the ρ_{ab} at different temperatures for y = 0.22 in (c) $B \parallel ab$ and (d) $B \parallel c$. The arrows denote the direction from low to high temperatures. (e–h) $\rho_{ab}(T)$ in (e) $B \parallel ab$ and (f) $B \parallel c$, and (g) $\rho_{ab}(B)$ in $B \parallel ab$ and (h) $B \parallel c$ for y = 0.69.

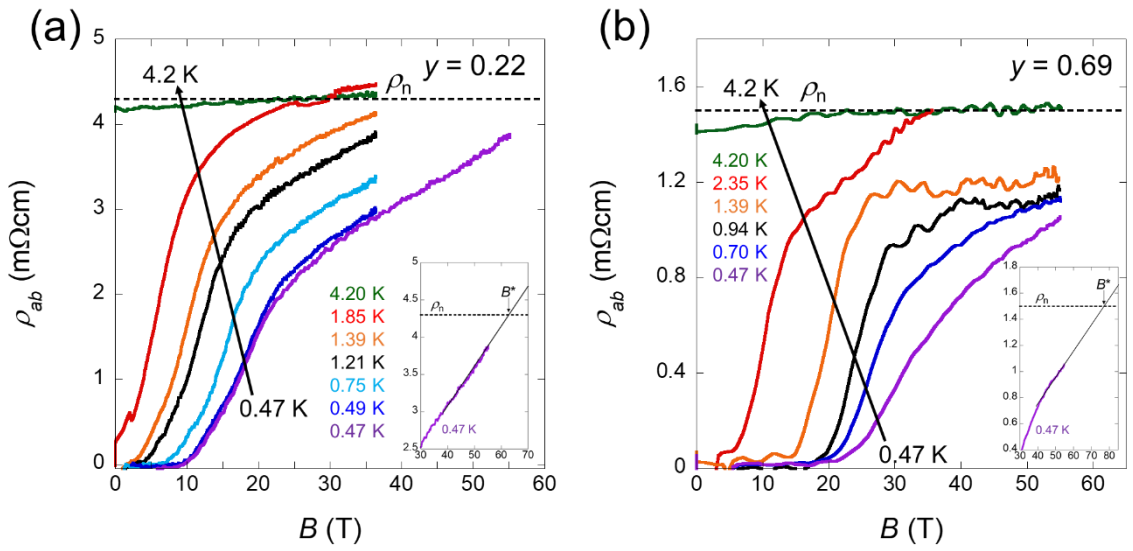

Fig. 10.4. Field dependence of the resistivity by pulsed magnetic fields. (a,b) Field dependence of the in-plane resistivity in $B \parallel ab$ for (a) y = 0.22 and (b) 0.69. The ρ_n (black dashed lines) denotes normal resistivity in the pulsed-field measurement. The insets show magnified views of the ρ_{ab} (B) curves at

T ~ 0.47 K near ρ_n. B^* is defined as the intersection of the extrapolation of the ρ_{ab} (B) curves and the ρ_n.

10.3. Temperature dependence of the upper critical fields

I summarize the in-plane $B_{c2}^{\parallel}$ (T) obtained by the static fields (Fig. 10.3) and pulsed fields (Fig. 10.4) for y = 0.22 and 0.69 in Figs. 10.5(a)–(d). Figures 10.5(a) and (b) show the midpoint criteria, and Figures 10.5(c) and (d) show the zero-resistivity criteria. The pulsed-field data are not so contradictory to the static-field data because we used the same single crystal samples. Note that there is uncertainty in the field directions in the pulsed-field measurements to deviate slightly from the *ab* plane because we could not use a rotator system in the setup; therefore, we added the error bar to the blue circles in Figs. 10.5(a)–(d). The upturn of $B_{c2}^{\parallel}$ at the low-temperature regions indicates that $B_{c2}^{\parallel}$ (0) probably exceeds our minimum temperature value ($T \approx 0.47$ K). Put differently, $B_{c2}^{\parallel}$ (T) is not saturated even at $T \approx 0.47$ K.

There are two distinct origins of upper critical fields, as explained in Chapter 3. I first describe the orbital pair-breaking effect. The orbital limit B_{orb} (0) is estimated to be 9.9 T and 0.34 T within the in-plane and out-of-plane direction for y = 0.22, and 17.7 T and 0.63 T within the in-plane and out-of-plane direction for y = 0.69 from the initial slope of B_{c2} at T_c (initial 6 points) based on the relation Eq. 3.5 with A = 0.69 in the dirty limit [97, 98]. The slopes are summarized in Table 10.3. Note that the upturn behavior of $B_{c2}^{\parallel}$ (T) near T_c is not suitable for the WHH model in nature [155]. I will discuss the upturn in Section 10.6 in detail. I describe the WHH curves [dashed lines in Figs. 10.5(a)–(d)]. The observed $B_{c2}^{\parallel}$ clearly exceeds the in-plane orbital limit, and the WHH curves are not suitable for $B_{c2}^{\parallel}$ at y = 0.22 and 0.69. The out-of-plane upper critical fields $B_{c2}^{\perp}$ (T) data are relatively well-fitted by WHH curves, as shown in Fig. 10.6. The black and blue dotted curves in Fig. 10.6 express WHH curves from the slopes of the initial 6 points and all points, respectively. The blue curves are almost comparable to the $B_{c2}^{\perp}$ (T) data for y = 0.22 in both midpoint and zero-resistivity criteria, while the experimental results for y = 0.69 slightly deviate from the WHH curves. Such deviation along the out-of-plane field direction was observed in previous work [155].

For the paramagnetic-pair breaking effect, the Pauli limit is estimated from Eq. 3.2. Pauli limit is estimated to be 5.9 and 7.6 T for y = 0.22 (T_c = 3.18 K) and 0.69 (T_c = 4.08 K), respectively. These values [black diamonds in Figs. 10.5 (a)–(d)] are much lower than the observed $B_{c2}^{\parallel}$ while much higher than $B_{c2}^{\perp}$. Thus, I expect that the out-of-plane upper critical fields $B_{c2}^{\perp}$ are determined by the orbital pair-breaking effect. To evaluate in-plane coherence lengths, I estimated the slopes of $B_{c2}^{\perp}(T)$ $(\frac{dB_{c2}}{dT}\Big|_{T=T_c})$ by initial 6 points and all-data points. I summarized these values in Table 10.2. I discuss the case of the slopes of $B_{c2}^{\perp}(T)$ by all-data points for midpoint criteria because the initial slope near T_c is assumed in the WHH model [other criteria and estimation are not inconsistent (see Tables 10.2

and 10.3)]. The in-plane coherence length $\xi_{\parallel}$ was evaluated from temperature-derivative Eq. 3.7. This led to $\xi_{\parallel} \approx 24$ and ≈ 18 nm for $y = 0.22$ and 0.69, respectively. These values are comparable to previous work for $y = 0$ [155]. I summarized in-plane conference lengths estimated from other criteria in Tables 10.1 and 10.2. To estimate the out-of-plane coherence length $\xi_{\perp}$, I used the B^*, defined as the intersection of the extrapolation of the $\rho_{ab}\ (B)$ curves at the minimum temperature of ~0.47 K and ρ_n (see the insets of Fig. 10.4). Specifically, B^* is expected to be the field that completely destroys the superconducting states at ~0.47 K. By using the values of $\xi_{\parallel}$ and B^* at the minimum temperatures, I roughly evaluated the out-of-plane coherence length $\xi_{\perp}$ at ~0.47 K from $B_{c2}^{\parallel} = \Phi_0/2\pi\xi_{\parallel}\xi_{\perp}$. That resulted in $\xi_{\perp} \approx 0.22$ and ≈ 0.24 nm for $y = 0.22$ and 0.69, respectively. The out-of-coherence lengths $\xi_{\perp}$ are almost comparable to the thickness of the blocking layer. I will discuss the relationship between the out-of-plane coherence lengths and the blocking-layer thickness in Section 10.5.

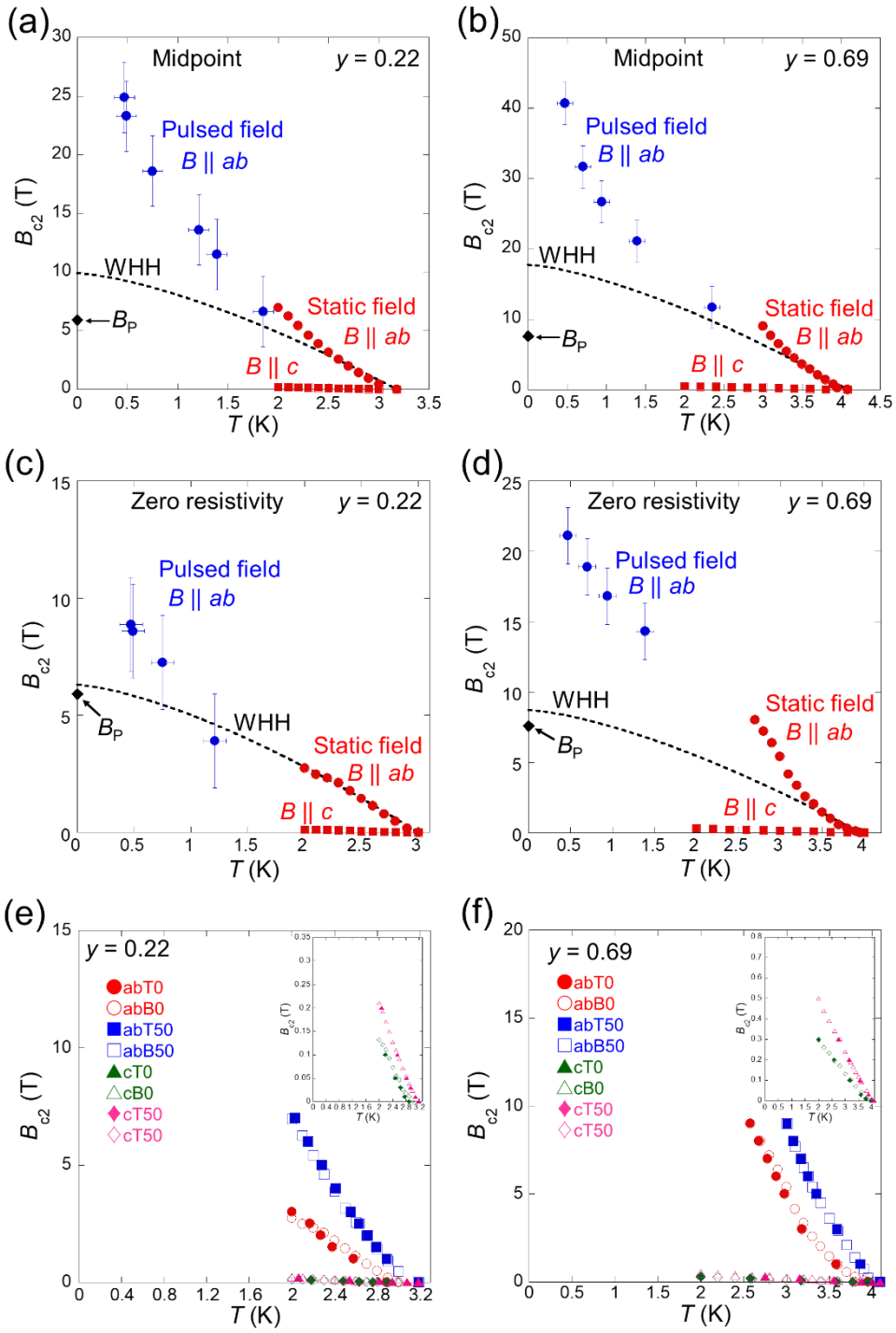

Fig. 10.5. Huge in-plane upper critical field for locally non-centrosymmetric superconductor $LaO_{0.5}F_{0.5}BiS_{2-y}Se_y$ (y = 0.22 and 0.69). (a,b) In-plane upper critical fields estimated from the midpoint of the resistive transition as functions of temperatures for (a) y = 0.22 and (b) 0.69. Red and blue circles show the $B_{c2}^{\parallel}(T)$ by static field and pulsed field, respectively. I added the error bars to the blue circles as it is possible for the applied fields to slightly deviate from the *ab* plane owing to the lack of rotator measurements. Additionally, there is uncertainty related to the stability of temperature. The

black dashed curves show the Werthamer–Helfand–Hohenberg (WHH) fits. Black diamonds denote the Pauli limit ($B_P = 1.86T_c$). (c,d) Temperature dependence of upper critical fields estimated from zero-resistivity criteria for (c) y = 0.22 and (d) 0.69. (e,f) Comparison of B_{c2} estimated from $\rho_{ab}(T)$ and $\rho_{ab}(B)$ curves. I also show the out-of-plane upper critical fields in the insets of (e) and (f). Temperature dependence of the upper critical fields from the $\rho_{ab}(T)$ and $\rho_{ab}(B)$ curves for (e) y = 0.22 and (f) 0.69. The abT0 (red closed circles) shows the in-plane upper critical fields defined as the beginning of the resistive increase from zero resistivity of the $\rho_{ab}(T)$ data, the abB0 (red open circles) of the $\rho_{ab}(B)$ data, abT50 (blue closed squares) as the midpoint of the resistive transition of the $\rho_{ab}(T)$ and abB50 (blue open squares) of the $\rho_{ab}(B)$, respectively. The cT0, cB0, cT50, and cT50 show the out-of-plane upper critical fields in the same way as the in-plane upper critical fields.

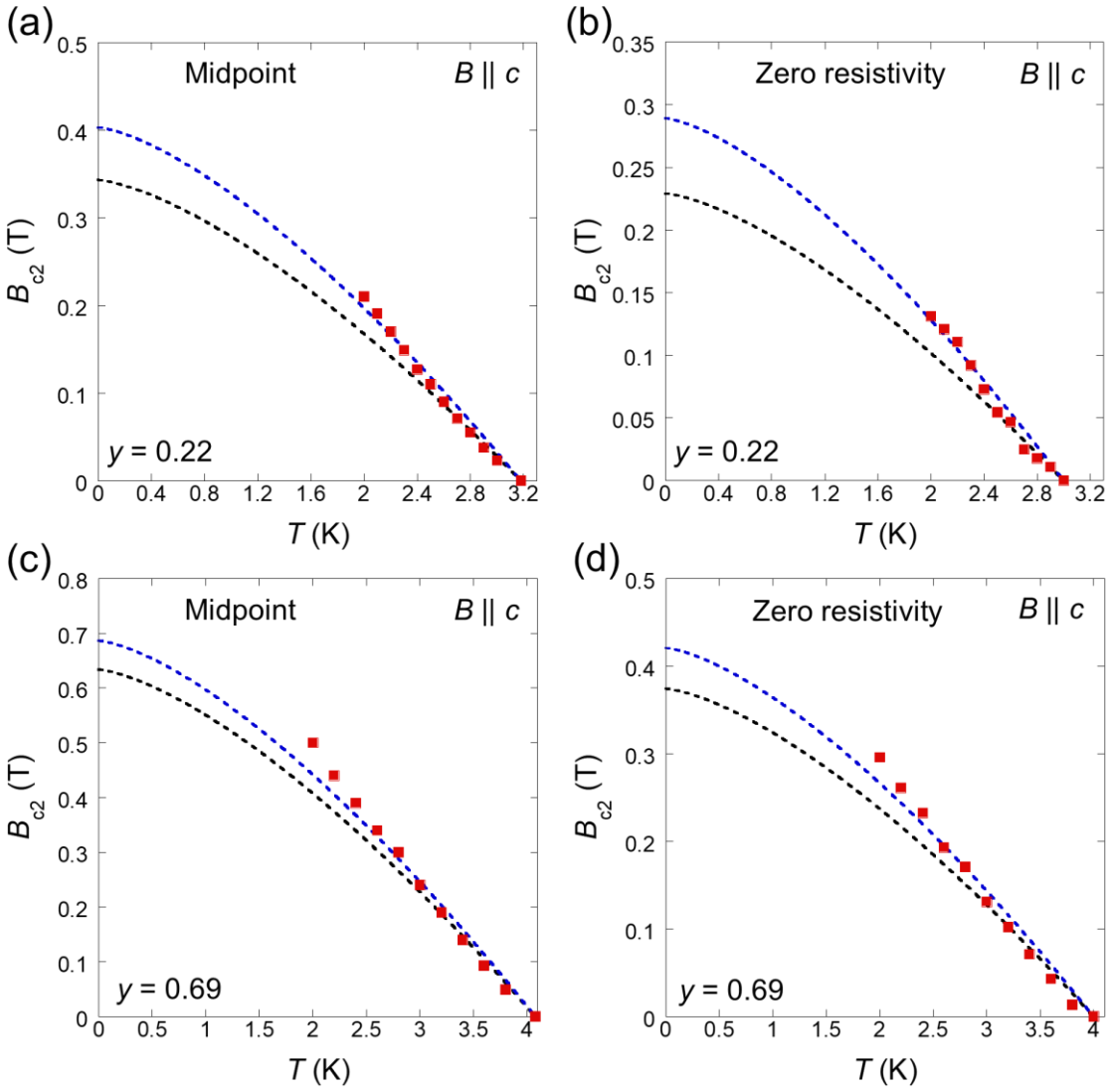

Fig. 10.6. Out-of-plane upper critical fields as functions of temperatures for (a,b) y = 0.22 and (c,d)

0.69. The upper critical fields in (a) and (c) [(b) and (d)] were evaluated from the midpoint of the resistive transition [zero-resistivity criteria]. The black and blue curves show the WHH curves by the initial 6 points and all-data points, respectively.

Table 10.1. Out-of-plane upper critical fields estimated from WHH curves by the beginning of the resistive increase from zero resistivity (zero-resistivity criteria) of the $\rho_{ab}(B)$ curves and middle points of the resistive transitions, and the in-plane coherence lengths from these criteria. ZR and MP mean the zero-resistivity and midpoint criteria, respectively. The 6 and A represent that the initial six points and all-data points were used for fitting, respectively.

Composition	$B_{c2}^{ZR6}(0)$ [T]	$B_{c2}^{ZRA}(0)$ [T]	$B_{c2}^{MP6}(0)$ [T]	$B_{c2}^{MPA}(0)$ [T]	$\xi_{\parallel}^{ZR6}(0)$ [nm]	$\xi_{\parallel}^{ZRA}(0)$ [nm]	$\xi_{\parallel}^{MP6}(0)$ [nm]	$\xi_{\parallel}^{MPA}(0)$ [nm]
$LaO_{0.5}F_{0.5}BiS_{1.78}Se_{0.22}$	0.23	0.29	0.34	0.40	38	34	31	29
$LaO_{0.5}F_{0.5}BiS_{1.31}Se_{0.69}$	0.37	0.42	0.63	0.69	30	28	23	22

Table 10.2. The slope of the temperature dependence of out-of-plane upper critical fields from the initial six and all-data points, and the in-plane coherence length from these slopes. The meaning of ZR6, ZRA, MP6, and MPA is the same as in Table 10.1.

Composition	$\left.\frac{dB_{c2}^{ZR6}}{dT}\right\|_{T=T_c}$ [T/K]	$\left.\frac{dB_{c2}^{ZRA}}{dT}\right\|_{T=T_c}$ [T/K]	$\left.\frac{dB_{c2}^{MP6}}{dT}\right\|_{T=T_c}$ [T/K]	$\left.\frac{dB_{c2}^{MPA}}{dT}\right\|_{T=T_c}$ [T/K]	$\xi_{\parallel}^{ZR6}(0)$ [nm]	$\xi_{\parallel}^{ZRA}(0)$ [nm]	$\xi_{\parallel}^{MP6}(0)$ [nm]	$\xi_{\parallel}^{MPA}(0)$ [nm]
$LaO_{0.5}F_{0.5}BiS_{1.78}Se_{0.22}$	-0.11	-0.14	-0.16	-0.18	32	28	26	24
$LaO_{0.5}F_{0.5}BiS_{1.31}Se_{0.69}$	-0.14	-0.15	-0.22	-0.24	25	23	19	18

Table 10.3. The slope of the temperature dependence of in-plane upper critical fields from the initial six and all-data points and the orbital limit from WHH curves. The meaning of ZR6, ZRA, MP6, and MPA is the same as in Table 10.1.

Composition	$\left.\frac{dB_{c2}^{ZR6}}{dT}\right\|_{T=T_c}$ [T/K]	$\left.\frac{dB_{c2}^{ZRA}}{dT}\right\|_{T=T_c}$ [T/K]	$\left.\frac{dB_{c2}^{MP6}}{dT}\right\|_{T=T_c}$ [T/K]	$\left.\frac{dB_{c2}^{MPA}}{dT}\right\|_{T=T_c}$ [T/K]	$B_{c2}^{ZR6}(0)$ [T]	$B_{c2}^{ZRA}(0)$ [T]	$B_{c2}^{MP6}(0)$ [T]	$B_{c2}^{MPA}(0)$ [T]
$LaO_{0.5}F_{0.5}BiS_{1.78}Se_{0.22}$	-3.0	-2.9	-4.5	-6.2	6.2	6.0	9.9	13.5
$LaO_{0.5}F_{0.5}BiS_{1.31}Se_{0.69}$	-3.2	-6.5	-6.3	-8.4	8.7	18.1	17.7	18.4

10.4. Theta angular dependence of the upper critical field

The angular θ dependence of the B_{c2} at T = 2.3 K and 2.5 K for y = 0.22, and T = 3.3 K and 3.5 K for y = 0.69 are displayed in Figs. 10.7 (θ represents the angle between the c-axis and the direction of the applied magnetic field). $B_{c2}\ (\theta)$ was estimated from the midpoint of the resistive transition. Generally, $B_{c2}\ (\theta)$ for layered superconductors is described by the anisotropic three-dimensional (3D) Ginzburg–Landau (GL) model or the 2D Tinkham formula. The anisotropic 3D GL model is given as

$$\left(\frac{B_{c2}(\theta)\cos\theta}{B_{c2}^{\perp}}\right)^2 + \left(\frac{B_{c2}(\theta)\sin\theta}{B_{c2}^{\parallel}}\right)^2 = 1. \qquad (10.1)$$

This formula explains $B_{c2}\ (\theta)$ for anisotropic 3D superconductors. In contrast, the 2D Tinkham's formula is given as

$$\left|\frac{B_{c2}(\theta)\cos\theta}{B_{c2}^{\perp}}\right| + \left(\frac{B_{c2}(\theta)\sin\theta}{B_{c2}^{\parallel}}\right)^2 = 1. \qquad (10.2)$$

This relation describes B_{c2} (θ) in the case of 2D systems. The 2D Tinkham formula exhibits cusp-like behavior around the magnetic field parallel to the plane. The observed B_{c2} (θ) is not contradictory to the anisotropic 3D GL model (orange solid curves in Fig. 10.7). The broadening of B_{c2} (θ) at y = 0.69 can be attributed to the flux flow and/or tiny single crystals with an inclination of a few degrees [108]. The 2D Tinkham formula (black dashed curves in Fig. 10.7) is not favorable for the broad B_{c2} (θ) behavior. We could not perform the angular dependence of the B_{c2} at lower temperatures because the maximum field in our rotator system (PPMS) is 9 T. Thus, the high-field and low-temperature regions might show the 2D nature of the B_{c2}. Moreover, we may need to use thin-film samples to exactly investigate the angular dependence of the upper critical fields, while there have been no reports for fabricating thin-film samples for the $BiCh_2$-based compounds at the present stage. I hope that studies using thin-film samples will be performed in the future.

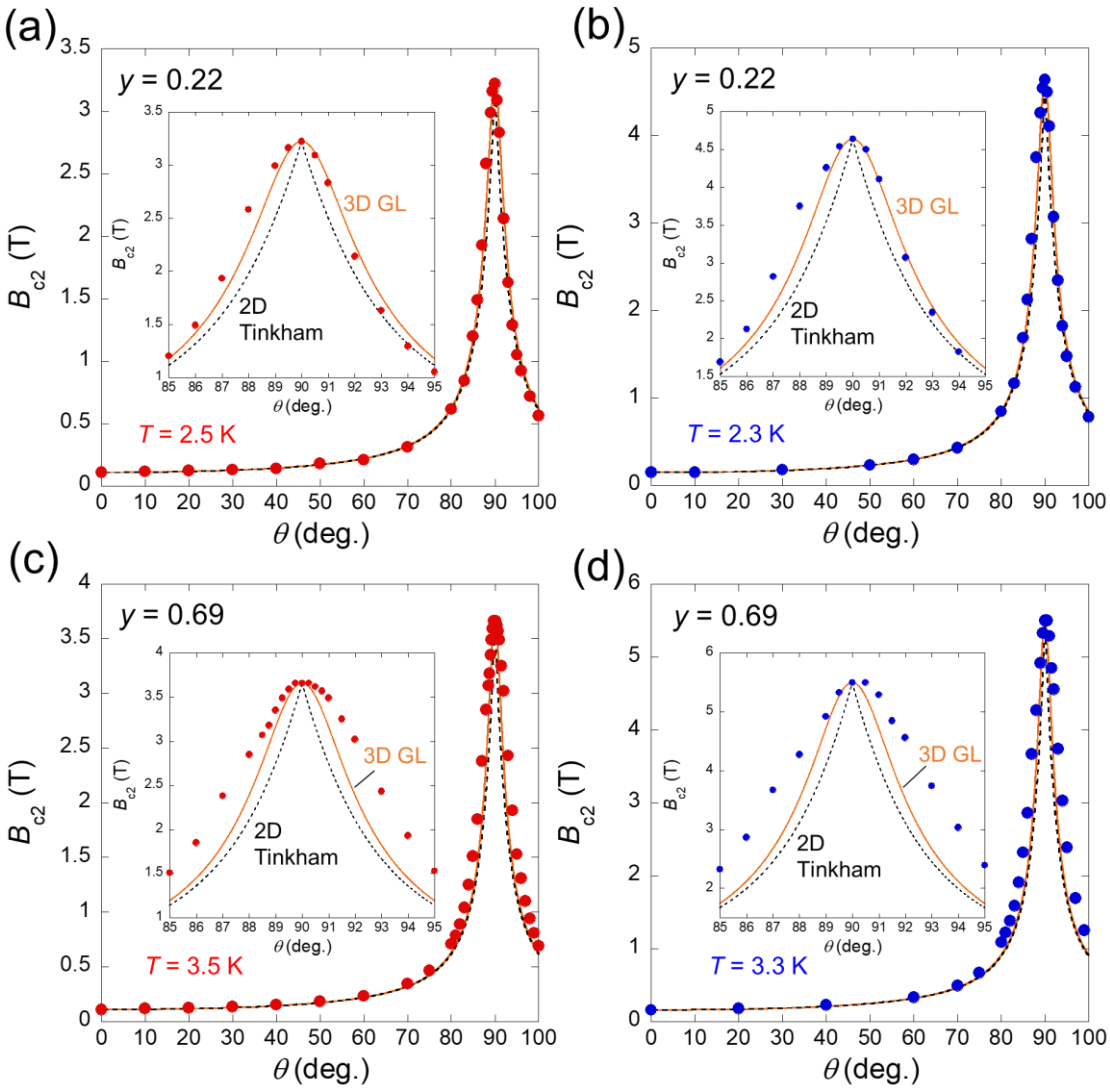

Fig. 10.7. Three-dimensional (3D) nature of the upper critical field. Angular θ dependence of the upper critical field at (a) T = 2.3 K and (b) 2.5 K for y = 0.22 and (c) T = 3.3 K and (d) 3.5 K for y = 0.69 (b). θ represents the angle between the c-axis and the direction of the applied magnetic field. The insets show magnified views of the region around θ = 90°. The orange solid curves denote the anisotropic 3D Ginzburg-Landau (GL) model (Eq. 10.1). The black dashed curves show the two-dimensional (2D) Tinkham formula (Eq. 10.2).

10.5. Suppression of both paramagnetic and orbital pair-breaking effects

The paramagnetic pair-breaking effect and the orbital pair-breaking effect should be suppressed because the observed in-plane $B_{c2}^{\parallel}$ clearly exceeds the Pauli limits and the orbital limits from the WHH model in the dirty limit. The strong coupling nature enhances the Pauli limit for the paramagnetic pair-breaking effect. While I assumed the validity of the weak-coupling limit (black diamonds in Fig. 10.5), several experimental results in $BiCh_2$-based superconductors indicate the strong-coupling nature [62, 63, 64, 84, and Chapter 2]. However, even if we use the reported value of $\Delta(0) = 2.25\, k_B T_c$ by specific heat measurements for the single crystal of $LaO_{0.5}F_{0.5}BiSSe$ (y = 1.0) [65], the Pauli limit is much smaller than the observed $B_{c2}^{\parallel}$. A previous study proposed that the behavior of in-plane B_{c2} for $LaO_{0.5}F_{0.5}BiS_2$ (y = 0) can be explained by the two-gap nature [155]. Indeed, μSR measurements imply that the two-gap superconductivity is suitable for the $BiCh_2$-based superconductor [67, 68, and Chapter 2]. However, multigap-superconductivity candidates, such as MgB_2 and Iron-based superconductors, have complicated FSs composed of multi-orbitals. In contrast, the $BiCh_2$-based systems have the relatively simple FS mainly comprised of Bi-6p_x/p_y orbitals, and these orbitals should degenerate in the F-doped tetragonal structure. Moreover, specific heat measurements suggested a single gap for the $LaO_{0.5}F_{0.5}BiSSe$ (y = 1.0) single-crystal sample [65]. Thus, I speculate that the single-gap scenario is probably valid for the present single-crystal samples because the μSR measurements, suggesting the multi-gap scenario, were performed using polycrystalline samples, and the anisotropy between the *ab*-plane and *c*-axis directions may influence the analysis of the μSR results. Therefore, I suggest that the lack of the local inversion symmetry in the $BiCh_2$ layer leads to the large in-plane $B_{c2}^{\parallel}$. The RSOI, due to the lack of local inversion symmetry, suppresses the paramagnetic pair-breaking effect even in the magnetic fields parallel to the *ab* plane because the spin direction is locked onto the *ab* plane, and the spin texture protects the Cooper pairs from depairing against the applied fields [155]. Strictly speaking, the suppression of the paramagnetic pair-breaking effect originates from the Van-Vleck susceptibility from the interlayer contribution due to the spin-band splitting, as introduced in Chapter 3. SARPES observed the local Rashba-type spin texture near the Fermi level for $LaO_{0.55}F_{0.45}BiS_2$ [153]. Moreover, the spin-singlet and spin-triplet states can be mixed in a material by breaking the local inversion

symmetry. If the spin-triplet component is the predominant component in the superconductivity in the present phases, the paramagnetic pair-breaking effect may be absent in this system. In any case, the paramagnetic pair-breaking effect was largely suppressed by the local inversion symmetry breaking in the $BiCh_2$ layer.

The orbital limit should also be enhanced to observe the high in-plane upper critical fields. The electronic correlation for the $BiCh_2$-based system is weak since the conduction band is mainly composed of Bi 6*p* orbitals. Thus, the effective mass for the $BiCh_2$-based system is not large [155], while the heavy-fermion system has a large effective mass. Indeed, the electronic specific heat coefficient is in the order of a few mJ/molK^2 for the $BiCh_2$-based compounds [65] despite the order of ~10^2–10^3 mJ/molK^2 for heavy-fermion systems [21]. In 2D superconductors, the orbital pair-breaking effect along the plane direction is primarily suppressed, as introduced in Chapter 3. The RSOI generally weakens the interlayer coupling and increases the 2D nature of the superconductivity [112]. This situation allows us to establish the Josephson vortex state in the magnetic fields parallel to the *ab* plane. We can regard the Josephson vortex phase as the CS phase (see Chapter 3). I will discuss this in the next section. Under this condition, I deduce that the Josephson vortices penetrate into the LaO blocking layer when the out-of-plane coherence length $\xi_\perp$ is comparable to the thickness of the blocking layer, in which the vortices may induce the orbital pair-breaking effect. However, $B_{c2}\ (\theta)$ in Fig. 10.7 indicates that the 2D nature is not strong because the anisotropic 3D GL model is relatively close to the obtained $B_{c2}\ (\theta)$ data. Therefore, it is reasonable to expect the crossover of the conventional Abrikosov (3D) and Josephson vortex (2D) state to be realized in this system. Furthermore, I plotted the temperature dependence of the $B_{c2}^{\parallel}/B_{c2}^{\perp}$ in Fig. 10.8(c) and (d). The values from the midpoint criteria for both samples (blue circles) increase with decreasing temperatures, which indicates that the 2D nature is enhanced at low-temperature regions. In contrast, the ratio for y = 0.22 by zero-resistivity criteria [red circles in Fig. 10.8(c)] has no clear dependence on temperatures. I will discuss the reason in the next section. To confirm whether the angular-dependent B_{c2} is changed by temperature, we may need to investigate $B_{c2}\ (\theta)$ at the lower-temperature regions by using dilution systems and/or thin-film samples in future work. Evaluation of the out-of-plane coherence length $\xi_\perp \approx$ 0.22 (y = 0.22) and ≈ 0.24 nm (y = 0.69) at the minimum temperature are comparable to the LaO blocking layer thicknesses ~0.26 nm in the cases of both samples. The blocking layer thicknesses were estimated from powder XRD at 298 K (room temperature). I expect that B_{c2} could be determined by the orbital pair-breaking effect from the Josephson vortices if we could confirm the change from the anisotropic 3D GL model to 2D Tinkham's formula in the lower temperature region and/or by using thin-film samples. On the other hand, we must be careful that the GL coherence length should be estimated from the temperatures close to T_c. The estimation of the out-of-plane coherence length is performed in much lower temperatures (~0.47 K) than T_c, while the in-plane coherence lengths, evaluated from the slope of $B_{c2}^{\perp}\ (T)$ as summarized in Table 10.2, are almost comparable to the

estimation by $B_{c2}^{\perp}$ (0) in Table 10.1. The observed in-plane $B_{c2}^{\parallel}$ (T) has the upturn behavior near T_c, and thus it is not practical to use the initial slope since Eq. 3.7 shows that the B_{c2} (T) is proportional to temperatures. If we assume a 2D superconductor for our system, the B_{c2} (T) is proportional to $\sqrt{T}$ (Eq. 3.8). Even so, it is difficult to explain the upturn behavior. I discuss the upturn of B_{c2} (T) near T_c in the next section.

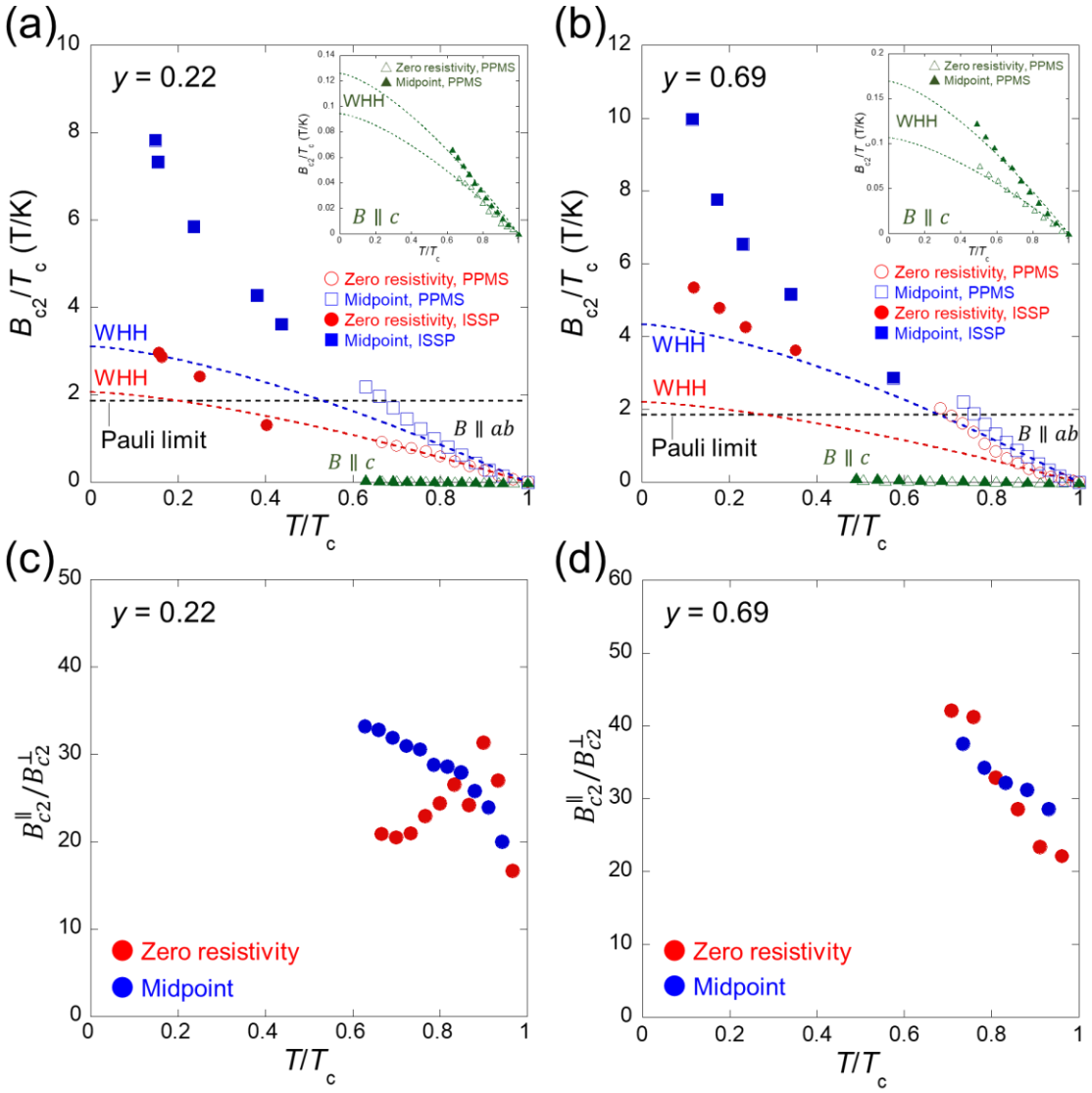

Fig. 10.8. Phase diagram of the upper critical fields for (a) y = 0.22 and (b) y = 0.69 with zero-resistivity and midpoint criteria. The upper critical fields and temperatures are divided by superconducting transition temperature T_c. The insets of (a) and (b) exhibit the out-of-plane upper critical fields. (c,d) $B_{c2}^{\parallel}/B_{c2}^{\perp}$ as a function of T/T_c by zero-resistivity (red circles) and midpoint (blue circles) criteria for (c) y = 0.22 and (d) y = 0.69.

10.6. Comparison with theoretical predictions

Finally, I discuss the unique phenomena in the locally non-centrosymmetric systems under magnetic fields: CS phase and PDW state. The CS phase emerges in the magnetic fields parallel to the *ab* plane and is induced by two distinct origins: the staggered RSOI (the paramagnetic pair-breaking effect is predominant) and the Josephson vortex state (the orbital pair-breaking effect is predominant) [109, 115]. In my target materials, I have not completely determined whether the orbital pair-breaking effect or the paramagnetic pair-breaking effect dominates in the in-plane field direction. However, if the discussion in Section 10.5 is spot-on, the Josephson vortices penetrate into the blocking layer, and the vortex state causes the orbital pair-breaking effect. Thus, we can expect that the orbital pair-breaking effect may lead to the CS phase. However, the upturn behavior of $B_{c2}^{\parallel}$ near T_c in blue open squares in Fig. 10.8(c,d) and red circles in Fig. 10.8(d) seems different from the theoretically predicted CS phase [109, 115]. I do not have a crystal-clear explanation about the upturn near T_c at the present stage. However, I can show a clue to resolve the problem below. There are not many examples of the CS phase. However, as introduced in Chapter 3, the multilayer systems composed of Pb (superconducting layers) and Sb (spacer layers) thin films exhibit the phase transition from uniform BCS to the CS phase in the magnetic fields parallel to the plane [109]. Interestingly, further increasing magnetic fields, another phase transition from the CS phase to the Helical phase was observed in the higher magnetic fields [109]. These phase transitions from uniform BCS to the CS phase further to the Helical phase originates from the center-of-mass momentum $\boldsymbol{q}$ and the interlayer coupling δ changing by magnetic fields [see Chapter 3]. Moreover, they suggested that the upturn of B_{c2} (T) at low and high fields corresponds to the transition from the uniform BCS to the CS phase and the Helical phase, respectively. Therefore, I speculate that the upturn behavior of the observed $B_{c2}^{\parallel}(T)$ probably relates to the CS or Helical phases. If the orbital pair-breaking effect by the Josephson vortex state is predominant for our target materials, the upturn near T_c may be explained. That is because the lower critical fields $B_{c1}^{\parallel}$ are much smaller than the obtained $B_{c2}^{\parallel}$. Figure 16.3 shows the in-plane magnetic field dependence of the magnetization for y = 0.65 (different batch from y = 0.69). The minimum value of the magnetization in the low-field region is only below ~20 Oe (~2 mT) for y = 0.65, which indicates that the $B_{c1}^{\parallel}$ is the order of ~mT. (Note that the demagnetization effect is much small in the in-plane magnetic field direction due to the plate-like single crystals.) The vortices can penetrate the blocking layers in much smaller fields than the $B_{c2}^{\parallel}$. Therefore, I deduce that the CS phase may emerge even near T_c, i.e., the transition fields from BCS to the CS phase may be much smaller (the order of mT). If it makes sense, the change in the behavior of $B_{c2}^{\parallel}(T)$ near T_c for y = 0.22 between different criteria [red and blue open circles in Figs. 10.8(a)] is somewhat strange. Upturn behavior of $B_{c2}^{\parallel}(T)$ near T_c should be observed even in zero-resistivity criteria for y = 0.22 if the scenario is correct. That is possibly due to the localization region for y = 0.22 (see Chapter 9). In

the region of the localization state, the shielding volume fraction is small [see Figs. 9.2(b) and (c)]. The bulkiness of the superconductivity might influence the difference between the zero-resistivity and midpoint criteria. Next, I comment on the broad resistive transition under higher magnetic fields (pulsed fields) for both samples. The broadening of the resistive transition might exhibit the presence of the Josephson vortex state since the broadening of the resistivity under magnetic fields is basically a common feature in type-II superconductors and can be caused by the motion of the vortices [169]. Hence, I speculate that the upturn of the $B_{c2}^{\parallel}(T)$ near T_c might be related to the CS phase and the non-saturated behavior at lower temperatures and higher magnetic fields to the Helical phase. A more detailed investigation is necessary to reveal whether the superconducting phases under magnetic fields are CS, Helical, or other phases.

Finally, I briefly comment on the PDW state in the magnetic fields parallel to the *c* axis. The obtained out-of-plane $B_{c2}^{\perp}(T)$ is clearly lower than the Pauli limit [black diamond in Figs. 10.5(a)–(d)], which implies that the $B_{c2}^{\perp}(T)$ follows the orbital pair-breaking effect. Indeed, the WHH model by all-data points (blue curves) is almost consistent with the out-of-plane $B_{c2}^{\perp}(T)$. In this condition, the PDW state cannot emerge in the magnetic-filed parallel to the *c* axis because it is realized under the assumption of weak or absent orbital pair-breaking effects [111].

In conclusion, I have observed extremely high in-plane upper critical fields for the centrosymmetric superconductor $LaO_{0.5}F_{0.5}BiS_{2-y}Se_y$ with local inversion symmetry breaking in the $BiCh_2$ layer. The superconducting states are not completely destroyed, even at the field strength of 55 T. The paramagnetic pair-breaking effect should be suppressed by the local RSOI, which arises from the lack of local inversion symmetry. The orbital limit should also be enhanced by the layered structure (quasi-2D-electronic states) and strong local RSOC. Local inversion symmetry breaking may be a clue for the solution of the pairing symmetry of superconductivity in the $BiCh_2$-based superconductor family. Our results pave the way for exploring superconductors with high upper critical fields and lead to an in-depth understanding of the relationship between superconductivity and local inversion symmetry breaking.

11. In-plane anisotropy of the MR in the superconducting state

11.1. Two-fold symmetric MR in the superconducting states

To further investigate the physical properties, I performed the in-plane anisotropy measurements of magnetoresistance in the normal and superconducting states. I expected that the four-fold symmetry of the tetragonal structure might be broken because the two-fold symmetric state of the monoclinic structure exists in the F-free systems, which is analogous to the electronic nematicity in the iron-based superconductors. Moreover, the layered crystal structures, including Bi, are similar to the doped-Bi_2Se_3, where nematic superconductivity has been observed. The crystal-structural similarity is a trigger that I tried to perform the anisotropy measurements for the $BiCh_2$-based superconductors. I used a two-axes rotator to precisely apply the magnetic fields to the plane. The in-plane anisotropy measurements were performed as collaborative work with the Institute of Materials Research (IMR), Tohoku University. In this study, I measured the *c*-axis resistivity [see Fig. 11.1(a)] because the Lorentz force on the vortices is identical concerning the in-plane angle ϕ variations [θ and ϕ are defined as Fig. 11.1(a)]. Figure 11.1(b) shows the temperature dependence of the *c*-axis resistivity for $LaO_{0.5}F_{0.5}BiSSe$ (This Se concentration is a nominal value). The obtained T_c is similar to the $LaO_{0.5}F_{0.5}BiS_{1.09}Se_{0.91}$ (x = 0.5, y = 0.91) in Fig. 9.1(b), but the magnitude of the *c*-axis resistivity is roughly 100 times larger than the *ab*-plane value, which implies that the electronic state has quasi-two-dimensional nature. Figure 11.1 (c) shows the θ angle dependence of the *c*-axis resistivity at the conditions of $\phi = 90°$, B = 15 T, and T = 2.5 K. ρ_{min} is defined as the minimum *c*-axis resistivity at which the magnetic field is precisely parallel to the *ab* plane. We performed the θ-angular-dependence measurements by changing ϕ angles from -180° to 180°. Figure 11.1(d) shows the ϕ dependence of ρ_{min} at T = 2.5 K and 5.0 K. The ϕ dependence of ρ_{min} shows dip at $\phi = \pm 90°$, indicating two-fold symmetry of ρ_{min} in the superconducting states (strictly speaking, mixed state). In contrast, the normal state at T = 5.0 K does not exhibit a clear correlation on the ϕ angular dependence in this scale. Given that the rotational symmetry breaking was observed only in the superconducting states, this phenomenon may not be close to the electronic nematicity in the normal states, such as iron-based superconductors but nematic superconductivity, such as doped-Bi_2Se_3. We can simply expect that the phenomenon is induced by symmetry lowering from tetragonal to monoclinic at low temperatures. On the other hand, as introduced in Chapter 8, tetragonal structures are stabilized by the F-substitution (electron-carrier doping) effect [38, 39]. Furthermore, the monoclinic distortion $100 \times |a - b|/(a + b)$ is only ~0.1% for F-free LaOBiSSe and ~0.2% for F-free $LaOBiS_2$ at room temperatures [36, 37] while the magnitude of the resistivity anisotropy $100 \times |\rho_{\mathrm{min}}^{\pm 90} - \rho_{\mathrm{min}}^{0 \text{ or } \pm 180}|/(\rho_{\mathrm{min}}^{\pm 90} + \rho_{\mathrm{min}}^{0 \text{ or } \pm 180})$ at T

= 2.5 K in Fig. 11.1 (d) is ~15%. However, the monoclinic distortion may become large at low temperatures. Thus, I expect two-fold symmetry in the superconducting states to be induced by the local monoclinic distortion (one-dimensional nature) with a single-component superconductor. I will discuss this possibility in Section 11.3.

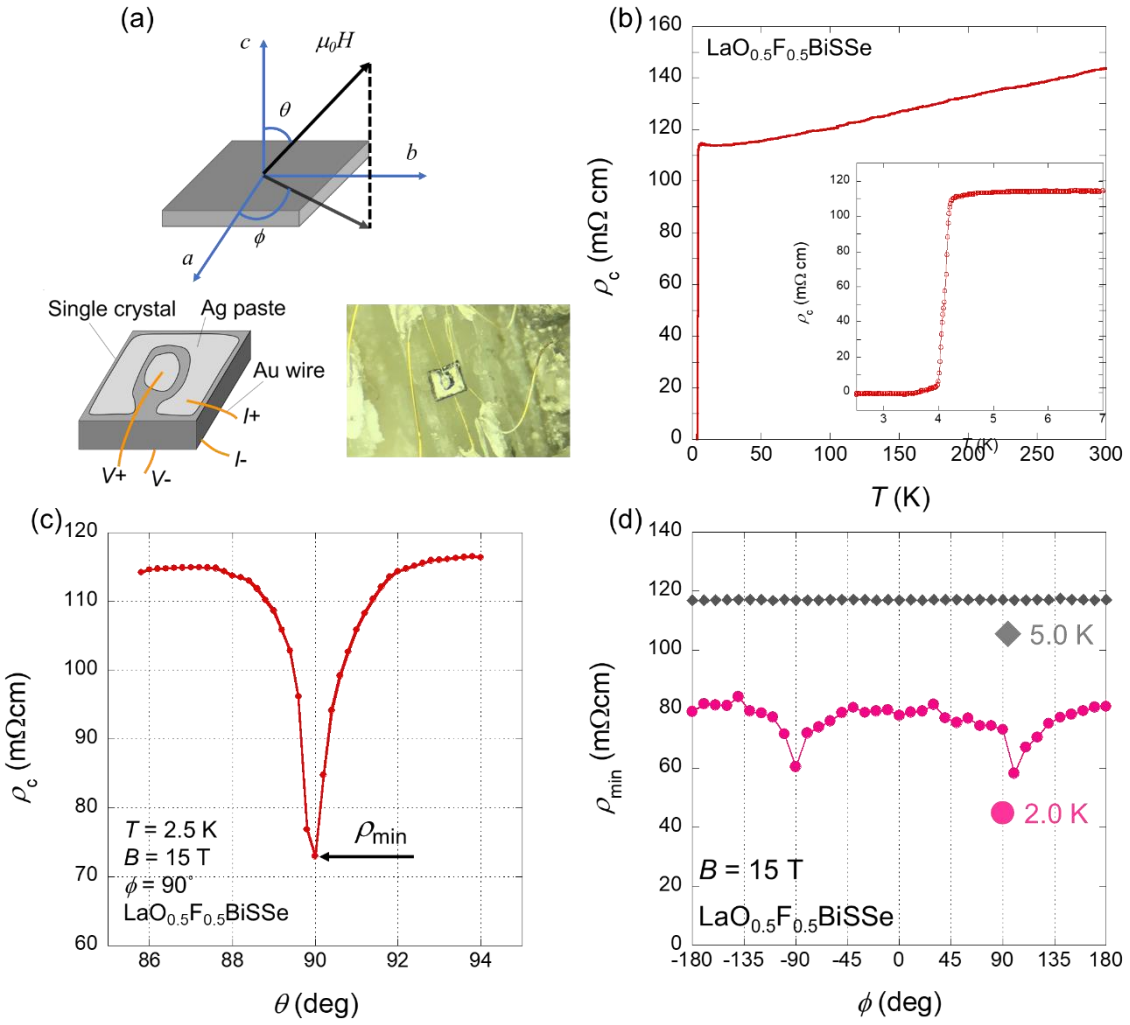

Fig. 11.1. (a) Schematic images and a photo of the experimental setup. θ is defined as the formed angle from the *c* axis to the *ab* plane, and ϕ is defined as the formed angle from the *a* axis to the *b* axis. (b) Temperature dependence of the *c*-axis resistivity for $LaO_{0.5}F_{0.5}BiSSe$ under zero magnetic field. The inset of (b) represents enlarged ρ_c-*T* curves around the superconducting transition. (c) θ dependence of the *c*-axis resistivity under ϕ = 90°, *B* = 15 T, and *T* = 2.5 K. The black arrow represents ρ_{min} where the magnetic field is exactly parallel to the *ab* plane. (d) ϕ dependence of ρ_{min} at *T* = 2.0 K (pink circles) and *T* = 5.0 K (gray diamonds) under *B* = 15 T.

11.2. Four-fold symmetric MR in the superconducting states

To further investigate the in-plane anisotropy of $BiCh_2$-based systems, I performed similar measurements to Fig. 11.1(c) and (d) for a different Se concentration from y = 1.0. I used comparable measurement systems to Section 11.1 at IMR, Tohoku university. Figure 11.2 (b) shows the temperature dependence of the c-axis resistivity for $LaO_{0.5}F_{0.5}BiS_{1.61}Se_{0.39}$ (y = 0.39). The observed T_c ≈ 3.3 K is smaller than y = 1 (nominal value), and the magnitude of the c-axis resistivity is in order of ~Ωcm in spite of ~mΩcm for y = 1.0 [see Fig. 11.1 (b)]. The different behavior by the Se substitution effect is consistent with Chapter 9's results. Figure 11.2(c) shows θ angular dependence of the c-axis resistivity under ϕ = -90°, B = 10 T, and T = 2.45 K (The definition of θ, ϕ, and ρ_{min} is the same as Section 11.1). The θ angular-dependence measurements were performed by changing ϕ angle per 10°, and Fig. 11.2(d) shows ρ_{min} as a function of the ϕ angle at T = 2.45 K (superconducting states) and T = 5 K (normal states). I described the two-fold and four-fold functions in Fig. 11.2(c). These are not fitting functions because the slight increase of ρ_{min} with increasing ϕ angle is not favorable for fitting, probably due to the sample shape [see Fig. 11.2(a)]. Thus, these functions are just eye-guided curves. The behavior of $\rho_{\mathrm{min}}(B)$ data is distinct from y = 1.0 in Fig. 11.1(d). From Fig. 11.2(d), we may expect that the four-fold component (orange curve) is close to the obtained data, which indicates that the four-fold symmetry is predominant in y = 0.39. At least, the one-dimensional order (two-fold-like symmetry) is not predominant in this composition as Fig.11.1(d) for y = 1.0 exhibits the peak-like behavior along $\phi = \pm 90°$. In contrast, the normal-state behavior has no clear correlation with the ϕ scan, consistent with y = 1.0 in Fig. 11.1(d). In the next section, I will discuss the conceivable reasons for the different behavior.

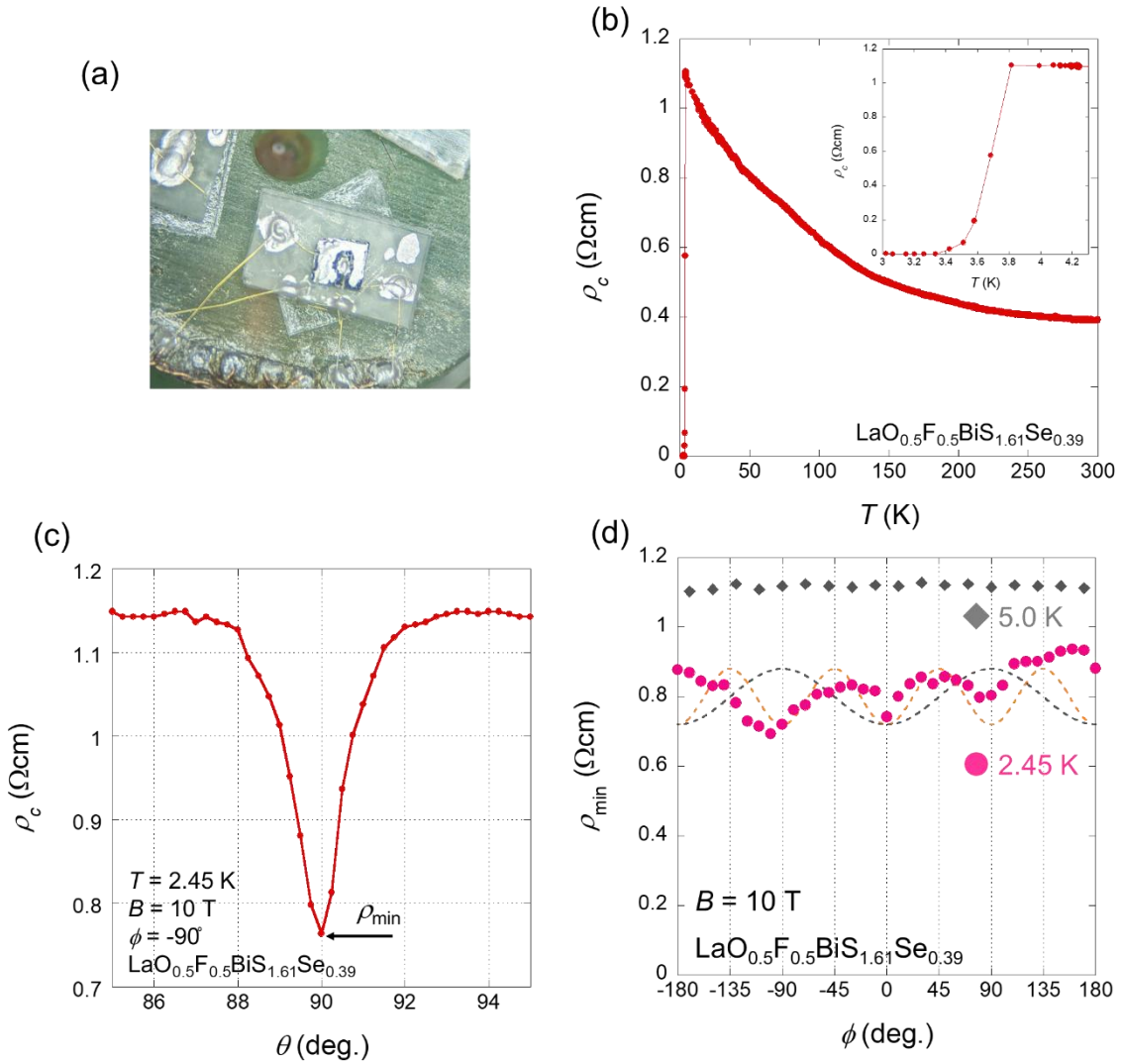

Fig. 11.2. (a) Photo of the experimental setup. (b) Temperature dependence of the *c*-axis resistivity for $LaO_{0.5}F_{0.5}BiS_{1.61}Se_{0.39}$ under zero magnetic field. The inset of (b) represents enlarged ρ_c-T curve around the superconducting transition. (c) θ angle dependence of the *c*-axis resistivity under ϕ = -90°, B = 10 T, and T = 2.45 K. The ρ_{min} criterion is the same as Fig. 11.1(c). (d) ϕ angle dependence of ρ_{min} at T = 2.45 K (pink circles) and T = 5.0 K (gray diamonds) under B = 10 T. Gray and orange curves exhibit two-fold component $0.07\cos\{2(\phi-90)\}+0.8$ and four-fold component $0.07\cos\{4(\phi-45)\}+0.8$, respectively. These functions are not fit curves since the slight increase of ρ_{min} with increasing ϕ is not suitable for using them as fittings.

11.3. Comparison with theoretical expectations

Finally, I compare the obtained experimental results with theoretical expectations. According to the theoretical calculations, the two-fold symmetry of the in-plane upper critical fields can emerge even in the conventional *s*-wave fully gapped superconductors [145, 146]. If we assume a single-component superconductor, such as a *s*-wave superconductor, the in-plane angular dependence of upper critical fields shows isotropic behavior in a tetragonal structure, as shown in Fig. 11.3. If there is a uniaxial strain in the single-component superconductor, two-fold symmetry of the in-plane upper critical fields can be realized. In contrast, when considering a two-component superconductor, the in-plane upper critical fields exhibit the four-fold symmetry in a tetragonal structure due to the degeneracy of two superconducting states. The uniaxial strain can lead to the two-fold symmetry of the in-plane upper critical fields. Therefore, the two-fold symmetry of the in-plane upper critical fields allows the uniaxial strain to exist even in either case of the single-component or two-component superconductivity. In the doped-Bi_2Se_3 superconductors, it has been suggested that two-component superconductivity (two-dimensional E_u representation in trigonal D_{3d} crystals) is realized, and thus the in-plane upper critical fields should show six-fold symmetry in trigonal crystals [146, 147]. The almost degenerated state of Δ_{4x} and Δ_{4y}, which is categorized as the two-dimensional E_u representation, is lifted by the uniaxial strain, and clear two-fold symmetry of the in-plane upper critical fields was observed [148]. So what is the origin of the in-plane anisotropy in the $BiCh_2$-based systems? It is reasonable to assume the presence of the uniaxial strain in the $BiCh_2$-based systems. Indeed, such one-dimensional instability similar to the uniaxial strain has been suggested in theoretical studies since the early stages [88, 89]. Moreover, several experimental results implied that the CDW formation, which is probably related to the one-dimensional instability, exists in the $BiCh_2$-based compounds [77, 90]. On the other hand, the four-fold-like symmetry of the MR in the superconducting states for $y = 0.39$ may indicate the presence of the two-component superconductivity, such as doped-Bi_2Se_3. In the tetragonal D_{4h} crystal of the target materials, the single-component and two-component superconductivity are summarized with superconducting-gap structures and the behavior of the in-plane upper critical fields in Table 11.1. Given the previous studies summarized in Table 11.1, the idea of a two-component superconductor is probably doubtful. When a two-component superconductor of E_u or E_g representations is realized in the $BiCh_2$-based superconductors, the superconducting-gap structures correspond to the p_x- and p_y-wave or d_{xz}- and d_{yz}-wave states, respectively. The p_x- and p_y-wave state is the spin-triplet superconductivity. However, there have been no reports suggesting spin-triplet superconductivity until this stage. Furthermore, when the one part of p_x- or p_y-wave superconductivity is realized, the superconducting-gap node lines are positioned along $k_x = 0$ or $k_y = 0$ lines. Under this condition and FS topology of $BiCh_2$-based compounds, symmetry-protected nodes are detected by bulk probes, such as magnetic penetration, specific heat, and thermal conductivity measurements. However, these

experiments suggested conventional nodeless *s*-wave superconductivity [62–65]. In addition, considering the d_{xz}- and d_{yz}-wave superconductivity, the line nodes should exist along the $k_x = 0$ or $k_y = 0$ lines as well. In nature, d_{xz}- and d_{yz}-wave superconductivity may not be favorable in the quasi-two-dimensional electronic states. Therefore, it is not easy to consider the two-component superconductor as the origin of the in-plane anisotropy for the $BiCh_2$-based superconductors. So what is the driving force for the four-fold symmetry? Given the previous studies, the single-component superconductivity such as fully gapped *s*-wave, anisotropic *s*-wave with accidental nodes, or $d_{x^2-y^2}$-wave states are reasonable as the superconducting-gap structure (see Table 11.1). Therefore, the four-fold symmetry of the MR in the superconducting states for y = 0.39 may originate from the FS topology. Regardless of Lifshitz transition around $x \approx 0.45$, the FS topology in the tetragonal may generate the four-fold symmetry. Moreover, the Se substitution is similar to the uniaxial strain effect. As a consequence, the two-fold symmetry was observed in y = 1. These discussions are the most promising explanation for the in-plane anisotropy of the MR in the superconducting states of these compounds. However, why the apparent in-plane anisotropy was observed only in superconducting states is still an open question. I hope that further studies will be developed in the future. Possibly, the lack of local inversion symmetry (Chapter 10) and/or localization (Chapter 9) may be related to the in-plane anisotropy. Especially the parity-mixed states may be a clue to reveal the in-plane anisotropy.

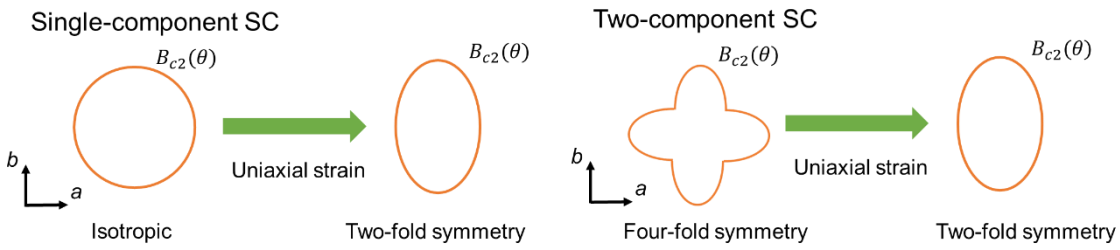

Fig. 11.3. Schematic images of the in-plane upper critical fields in a tetragonal D_{4h} lattice. The left- and right-hand cases show the single-component and two-component superconductivity, respectively. These images were described based on Ref. 145 and 146.

Table. 11.1. Classification of superconducting-gap structures, in-plane upper critical fields, and previous theoretical and experimental studies. The tetragonal crystal D_{4h} is assumed to describe the superconducting-gap structures and in-plane upper critical fields. In addition, I displayed several references to theoretical calculations and experiments.

SC gap structure (point group)	SC component	B_{c2} in *ab*-plane	Theoretical calculation	Experiment
s-wave (A_{1g})	Single	Isotropic	Yes [32, 60]	Yes [62-65]
Extended s-wave (A_{1g})	Single	Isotropic	Yes [32, 60, 72]	Yes [66, 75]
p_x-wave, p_y-wave (E_u)	Two	Four-fold symmetry	No	No
$d_{x^2-y^2}$-wave (B_{1g})	Single	Isotropic	Yes [32, 60, 72]	Yes [75]
d_{xy}-wave (B_{2g})	Single	Isotropic	Yes [60, 70]	No
d_{xz}-wave, d_{yz}-wave (E_g)	Two	Four-fold symmetry	No	No

12. Summary and Conclusion

I have investigated the transport properties for single-crystal samples of $BiCh_2$-based superconductors $LaO_{1-x}F_xBiS_{2-y}Se_y$. Especially, I focused on the local inversion symmetry breaking in the $BiCh_2$ layer and localization behavior in the normal states. Furthermore, I examined crystal structures for $LaO_{1-x}F_xBiS_{2-y}Se_y$ using synchrotron X-ray diffraction before investigating these phenomena and found that small F-doing (a few%) stabilizes the tetragonal structure in $LaO_{1-x}F_xBiSSe$.

Non-centrosymmetric superconductors have been extensively studied for a long time. Recent studies have suggested that locally non-centrosymmetric systems exhibit intriguing physical properties even in globally centrosymmetric compounds. In particular, several examples of local inversion symmetry breaking in layered systems exist. In a bilayer system, when each layer lacks inversion symmetry but the bilayer is coupled by interlayer coupling (globally centrosymmetric compounds), layer-dependent Rashba-type spin-orbit coupling can exist. The staggered Rashba-type spin-orbit interaction can cause unique superconducting properties. More recently discovered $CeRh_2As_2$ have centrosymmetric tetragonal structure *P*4/*nmm* (No. 129, D_{4h} point group) while the Ce site lacks the inversion symmetry with the C_{4v} site point group. This superconductor showed huge out-of-plane upper critical fields and phase transition under magnetic fields, which is consistent with theoretical expectations. The crystal structure of my target superconductors $LaO_{0.5}F_{0.5}BiS_{2-y}Se_y$ has tetragonal *P*4/*nmm*, and the Bi and Ch sites lack inversion symmetry with the C_{4v}. Thus, I expected large upper critical fields to be observed in the $BiCh_2$-based superconductors. I have investigated the in-plane and out-of-plane upper critical fields for $LaO_{0.5}F_{0.5}BiS_{2-y}Se_y$ (y = 0.22 and 0.69) by resistivity measurements under static fields and pulsed high fields. As a consequence, huge in-plane upper critical fields were observed for both samples. The in-plane upper critical fields are enhanced by the modulated Rashba-type spin-orbit interaction and the quasi-two-dimensional electronic states. Since the estimated out-of-plane coherence length is comparable to the thickness of the blocking layer, I speculate that the orbital pair-breaking effect by the Josephson vortex state is predominant along the in-plane direction. The upturn behavior of $B_{c2}^{\parallel}(T)$ near T_c may be related to the theoretically-predicted CS phase (Josephson vortex phase). At least, I deduce that the local Rashba-type spin-orbit interaction plays a significant role in superconducting states in $BiCh_2$-based superconductors. Under the inversion asymmetry, the parity-mixed state can be realized. I hope studies focusing on the parity-mixed state will be developed in future work. In contrast, out-of-plane upper critical fields are much smaller than the in-plane direction. The results imply that the orbital-pair breaking effect is predominant along the out-of-plane directions because the upper critical fields are suppressed below the Pauli limits.

Weak localization (WL) and weak antilocalization (WAL) have been extensively studied for over half a century since Anderson suggested localization in disordered conductor systems in 1958.

Constructive and destructive quantum interference causes WL and WAL. In previous reports, optimally F-doped and Se-free samples showed that weak increases in resistivity with decreasing temperatures were observed, which indicates the presence of any localization states. However, magnetoresistance data were not reported in the previous work. Thus, I performed magnetoresistance measurements in the normal states for $LaO_{1-x}F_xBiS_{2-y}Se_y$. I have found that Se-free and moderately Se-substituted samples exhibit a crossover of WL and WAL or *weak* WAL (almost quadratic MR) states. Compared with previous studies, the localization states may be related to the charge-density-wave formation. Moreover, heavily Se-substituted samples present WAL states. As the most important point, these magnetoresistance changes in the normal states by the elemental substitution are correlated with temperature dependences of resistivity and Hall coefficient. Furthermore, the change in localization behavior by Se substitution is probably related to the relative strength of the band gap and Fermi level, given the recent theoretical calculations. These results indicate that the Se-substitution effect suppresses the localization for the $BiCh_2$-based system.

These results of high in-plane upper critical fields and the localization/antilocalization are related to spin-orbit interaction. Therefore, this study has not only found the intriguing physical phenomena but also paved the way for the significance of spin-orbit interaction, particularly Rashba-type spin-orbit interaction in the $BiCh_2$-based systems. Thus, if thin films for the $BiCh_2$-based compounds are successfully prepared, studies also in spintronics fields will be developed in the future.

Finally, in the normal and superconducting states, I performed in-plane anisotropy measurements for $LaO_{0.5}F_{0.5}BiS_{2-y}Se_y$ (y = 0.39, 1.0). Four-fold and two-fold symmetry of the magnetoresistance in the superconducting states were observed in small (y = 0.39) and heavy (y = 1.0) Se concentrations, respectively. Compared with previous studies, the four-fold symmetry may be related to the FS topology, and the uniaxial strain, such as the one-dimensional order, may lead to the two-fold symmetry. The Se substitution effect is probably similar to the uniaxial strain. Furthermore, the alteration of the in-plane anisotropy by the Se substitution might be related to the local inversion symmetry breaking and/or the localization/antilocalization behavior. I hope that comprehensive research will be established in the future.

13. References

13.1. References to the main text

[1] H. K. Onnes, Commun. Phys. Lab. Univ. Leiden. Suppl. **29** (1911).

[2] D. Van Delft and P. Kes, Phys. Today **63**(9), 38 (2010).

[3] B. T. Matthias, Phys. Rev. **92**, 874 (1953).

[4] B. T. Matthias *et al*., Phys. Rev. **95**, 1435 (1954).

[5] J. R. Gavaler, Appl. Phys. Lett. **23**, 480 (1973).

[6] M. R. Norman, Science **332**, 196. (2011).

[7] Bednorz, J. G., and K. A. MuÈller, 1986, Z. Phys. B **64**, 189 (1986).

[8] M. K. Wu *et al*., Phys. Rev. Lett. **58**, 908 (1987).

[9] B. Keimer *et al*., Nature 518, 179 (2015).

[10] Y. Maeno *et al*., Nature **372**, 532 (1994).

[11] A. J. Leggett and Y. Liu, J. Supercond. Novel Magn. **34**, 1647 (2020).

[12] A. Pustogow *et al*., Nature **574**, 72 (2019).

[13] J. Nagamatsu *et al*., Nature **410**, 63 (2001).

[14] S. Souma *et al*., Nature **423**, 65 (2003).

[15] Y. Kamihara *et al*., J. Am. Chem. Soc. **130**, 3296 (2008).

[16] C. Wang *et al*., Europhys. Lett. **83**, 67006 (2008).

[17] T. Shibauchi, *et al*., Annu. Rev. Condens. Matter Phys. **5**, 113 (2014).

[18] T. Shibauchi *et al*., J. Phys. Soc. Jpn. **89**, 102002 (2020).

[19] A. P. Drozdov *et al*, Nature **525**, 73 (2015).

[20] E. Snider *et al*., Nature **586**, 373 (2020).

[21] Y. Ōnuki *et al*., J. Phys. Soc. Jpn. **73**, 769 (2004).

[22] D. Aoki *et al*., J. Phys. Soc. Jpn. **88**, 022001 (2019).

[23] Y. Saito *et al*., Nat. Rev. Mater. **2**, 16094 (2016).

[24] M. Sato and Y. Ando, Rep. Prog. Phys. **80**, 076501 (2017).

[25] J. Bardeen, L. N. Cooper, and J. R. Schrieffer, Phys. Rev. **108**, 1175 (1957).

[26] H. Frölich, Phys. Rev. **79**, 845 (1950).

[27] J. de Launay, Phys. Rev. **93** 661 (1954).

[28] M. Tinkham, *Introduction to Superconductivity*, (New York: McGraw-Hill) (1975).

[29] K. Momma and F. Izumi, J. Appl. Crystallogr. **44**, 1272 (2011).

[30] Y. Mizuguchi *et al*., Phys. Rev. B **86**, 220510 (2012).

[31] Y. Mizuguchi, J. Phys. Soc. Jpn. **88**, 041001 (2019).

[32] H. Usui *et al*., Phys. Rev. B **86**, 220501(R) (2012).

[33] Y. Mizuguchi *et al*., J. Phys. Soc. Jpn. **81**, 114725 (2012).

[34] B. Li, *et al*, Europhys. Lett. **101**, 47002 (2013).

[35] H. Huang *et al*., J. Materiomics. **8**, 302–310 (2022).

[36] R. Sagayama *et al*., J. Phys. Soc. Jpn. **84**, 123703 (2015).

[37] K. Nagasaka *et al*., J. Phys. Soc. Jpn. **86**, 074701 (2017).

[38] N. Hirayama *et al*., Phys. Rev. B **100**, 125201 (2019).

[39] K. Hoshi *et al*., Condensed Matter **5**, 81 (2020).

[40] J. Xing *et al*., Phys. Rev. B **86**, 214518 (2012).

[41] M. Tanaka *et al*., J. Alloys Compd. **722**, 467 (2017).

[42] H. F. Zhai *et al*., Phys. Rev. B **90**, 064518 (2014).

[43] A. Krzton-Maziopa *et al*., J. Phys.: Condens. Matter **26**, 215702 (2014).

[44] M. Nagao *et al*., J. Phys. Soc. Jpn. **82**, 113701 (2013).

[45] M. Nagao, Novel Supercond. Mater. **1**, 64 (2015).

[46] Y. L. Sun *et al*., Inorg. Chem. **53**, 11125 (2014).

[47] R. Jha *et al*., J. Phys. Soc. Jpn. **87**, 083704 (2018).

[48] R. Jha and Y. Mizuguchi, Condensed Matter **5**, 27 (2020).

[49] Y. Yuan *et al*., Phys. Rev. B **105**, 064509 (2022).

[50] B.-B. Ruan *et al*., J. Am. Chem. Soc. **141**, 3404 (2019).

[51] Y. Mizuguchi *et al*., J. Phys. Soc. Jpn. **87**, 023704 (2018).

[52] M. Tanaka *et al*., Appl. Phys. Lett. **106**, 112601 (2015).

[53] E. Paris *et al*., J. Phys.: Condens. Matter **30**, 455703 (2018).

[54] E. Paris *et al*., J. Phys.: Condens. Matter **29**, 145603 (2017).

[55] F. Izumi and K. Momma, Solid State Phenom. **130**, 15 (2007).

[56] T. Tomita *et al*., J. Phys. Soc. Jpn. **83**, 063704 (2014).

[57] A. Yamashita *et al*., Sci. Rep. **10**, 12880 (2020).

[58] W. L. McMillan, Phys. Rev. **167**, 331 (1968).

[59] P. B. Allen and R. C. Dynes, Phys. Rev. B **12**, 905 (1975).

[60] K. Suzuki *et al*., J. Phys. Soc. Jpn. **88**, 041008 (2019).

[61] C. Morice *et al*., Phys. Rev. B **95**, 180505 (2017).

[62] Shruti, P. Srivastava, and S. Patnaik, J. Phys.: Condens. Matter **25**, 312202 (2013).

[63] L. Jiao *et al*., J. Phys.: Condens. Matter **27**, 225701 (2015).

[64] T. Yamashita *et al*., J. Phys. Soc. Jpn. **85**, 073707 (2016).

[65] N. Kase *et al*., Phys. Rev. B **96**, 214506 (2017).

[66] G. Lamura *et al*., Phys. Rev. B **88**, 180509 (2013).

[67] P. K. Biswas *et al*., Phys. Rev. B **88**, 224515 (2013).

[68] J. Zhang *et al*., Phys. Rev. B **94**, 224502 (2016).

[69] K. Suzuki *et al*., Phys. Rev. B **96**, 024513 (2017).
[70] X. Wu *et al*., Europhys. Lett. **108**, 27006 (2014).
[71] M. A. Griffith *et al*., J. Phys.: Condens. Matter **29**, 305601 (2017).
[72] T. Agatsuma and T. Hotta, J. Magn. Magn. Mater. **400**, 73 (2016).
[73] K. Terashima *et al*., J. Phys. Soc. Jpn. **88**, 041006 (2019).
[74] L. K. Zeng *et al*., Phys. Rev. B **90**, 054512 (2014).
[75] Y. Ota *et al*., Phys. Rev. Lett. **118**, 167002 (2017).
[76] Y. Mizukami *et al*., Nat. Commun. **5**, 5657 (2014).
[77] T. Machida *et al*., J. Phys. Soc. Jpn. **83**, 113701 (2014).
[78] A. Ichikawa and T. Hotta, J. Phys. Soc. Jpn. **87**, 114706 (2018).
[79] B. Batlogg *et al*., Phys. Rev. Lett. **58**, 2333 (1987).
[80] P. M. Shirage *et al*., Phys. Rev. Lett. **103**, 257003 (2009).
[81] K. Hoshi *et al*., Phys. Rev. B **97**, 094509 (2018).
[82] R. Jha and Y. Mizuguchi, Appl. Phys. Lett. **13**, 093001 (2020).
[83] S. Kasahara *et al*., Nat. Commun. **7**, 12843 (2016).
[84] J. Liu *et al*., Europhys. Lett. **106**, 67002 (2014).
[85] S. Li *et al*., China: Phys. Mech. Astron. **56**, 2019 (2013).
[86] Y. Li *et al*., Supercond. Sci. Technol. **27**, 035009 (2014).
[87] S. K. Singh *et al*., J. Am. Chem. Soc. **134**, 16504 (2012).
[88] T. Yildirim, Phys. Rev. B **87**, 020506 (2013).
[89] X. Wan *et al*., Phys. Rev. B **87**, 115124 (2013).
[90] S. Demura *et al*., J. Phys. Soc. Jpn. **86**, 113701 (2017).
[91] J. Lee *et al*., Phys. Rev. B **103**, 245120 (2021).
[92] J. Kajitani *et al*., J. Phys. Soc. Jpn. **90**, 103601 (2021).
[93] H. F. Zhai *et al*., Phys. Rev. B **90**, 064518 (2014).
[94] R. Higashinaka *et al*., J. Phys. Soc. Jpn. **84**, 023702 (2015).
[95] E. Bauer, M. Sigrist, Eds., Non-Centrosymmetric Superconductors: Introduction and Overview, vol. 847 of Lecture Notes in Physics (Springer-Verlag, 2012).
[96] M. Smidman *et al*., Rep. Prog. Phys. **80**, 036501 (2017).
[97] E. Helfand and N. R. Werthamer, Phys. Rev. **147**, 288 (1966).
[98] N. R. Werthamer, E. Helfand, and P. C. Hohenberg, Phys. Rev. **147**, 295 (1966).
[99] E. Bauer *et al*., Phys. Rev. Lett. **92**, 027003 (2004).
[100] N. Kimura *et al*., Phys. Rev. Lett. **95**, 247004 (2005).
[101] X. Xi *et al*., Nat. Phys. **12**, 139 (2016).
[102] Y. Saito *et al*., Nat. Phys. **12**, 144 (2016).
[103] M. Sigrist *et al*., J. Phys. Soc. Jpn. **83**, 061014 (2014).

[104] M. H. Fischer *et al*., arXiv:2204.02449 (2022).
[105] Y. Mizukami1 *et al*., Nat. Phys. **7**, 849 (2011).
[106] S. K. Goh *et al*., Phys. Rev. Lett. **109**, 157006 (2012).
[107] M. Shimozawa *et al*., Phys. Rev. Lett. **112**, 156404 (2014).
[108] O. Zheliuk *et al*., Nat. Nanotechnol. **14**, 1123 (2019).
[109] R. Masutomi *et al*., Phys. Rev. B **101**, 184502 (2020).
[110] S. Kim *et al*., Science **373**, 1012 (2021).
[111] T. Yoshida *et al*., Phys. Rev. B **86**, 134514 (2012).
[112] D. Maruyama *et al*., J. Phys. Soc. Jpn. **81** 034702 (2012).
[113] T. Yoshida *et al*., Phys. Rev. Lett. **115**, 027001 (2015).
[114] T. Yoshida *et al*., J. Phys. Soc. Jpn. **82**, 074714 (2013).
[115] T. Watanabe *et al*., Phys. Rev. B **92**, 174502 (2015).
[116] K. Nogaki *et al*., Phys. Rev. Res. **3**, L032071 (2021).
[117] P. W. Anderson, Phys. Rev. **109**, 1492 (1958).
[118] A. Lagendijk *et al*., Phys. Today **62**, 24 (2009).
[119] G. Bergmann, Phys. Rep. **107**, 1 (1984).
[120] E. Abrahams *et al*., Phys. Rev. Lett. **42** 673 (1979).
[121] L. P. Gorkov *et al*., Pis'ma Zh. Eksp. Teor. Fiz. **30** 248 (1979). [JETP Lett. **30** 228 (1979)].
[122] H. Fukuyama and K. Yoshida, J. Phys. Soc. Jpn. **46**, 102 (1979).
[123] Y. Kawaguchi and S. Kawaji, J. Phys. Soc. Jpn. **48**, 699 (1980).
[124] S. Hikami, A. I. Larkin and Y. Nagaoka, Prog. Theor. Phys. **63**, 707 (1980).
[125] G. Bergman, Phys. Rev. Lett. **48**, 1046 (1982).
[126] M. Liu *et al*., Phys. Rev. Lett. **108**, 036805 (2012).
[127] M. Aitani *et al*., Phys. Rev. Lett. **113**, 206802 (2014).
[128] Y. Pan *et al*., New J. Phys. **16**, 123035 (2014).
[129] H. Yuan *et al*., Nat. Phys. **9**, 563 (2013).
[130] H. Liu *et al*., Nano Lett. **19**, 4551 (2019).
[131] L. Wang et al., Nat. Commun. **6**, 8892 (2015).
[132] S. V. Iordanskii, Y. B. Lyanda-Geller, and G. E. Pikus, JETP Lett. **60**, 206 (1994).
[133] T. Kawaguti and Y. Fujimori, J. Phys. Soc. Jpn. **52**, 722 (1983).
[134] H–T. He *et al*., Phys. Rev. Lett. **106**, 166805 (2011).
[135] F.V. Tikhonenko *et al*., Phys. Rev. Lett. **103**, 226801 (2009).
[136] C. H. Naylor et al., Nano Lett. **16**, 4297 (2016).
[137] A. T. Neal *et al*., ACS Nano **8**, 9137 (2014).
[138] S. Hao *et al*., Adv. Funct. Mater. **28**, 1803746 (2018).
[139] H. Schmidt *et al*., Phys. Rev. Lett. **116**, 046803 (2016).

[140] J. Wu *et al*., Proc. Natl. Acad. Sci. U.S.A. **117**, 10654 (2020).
[141] S. Yonezawa, Condens. Matter **4**, 2 (2019).
[142] K. Matano *et al*., Nat. Phys. **12**, 852 (2016).
[143] S. Yonezawa *et al*., Nat. Phys. **13**, 123 (2017).
[144] Y. Pan *et al*., Sci. Rep. **6**, 28632 (2016).
[145] L. I. Burlachkov, Zh. Eksp. Teor. Fiz. **89**, 1382 (1985) [Sov. Phys. JETP **62**, 800 (1985)].
[146] J. W. F. Venderbos *et al*., Phys. Rev. B **94**, 094522 (2016).
[147] L. Fu and E. Berg, Phys. Rev. Lett. **105**, 097001 (2010).
[148] I. Kostylev *et al*., Nat. Commun. **11**, 4152 (2020).
[149] Y. Machida, *et al*., Phys. Rev. Lett. **108**, 157002 (2012).
[150] Y. Xiang *et al*., Nat. Commun. **12**, 6727 (2021).
[151] M. Roppongi *et al*., arXiv: 2206.02580. (2022).
[152] X. Zhang *et al*., Nat. Phys. **10**, 387 (2014).
[153] S. L. Wu *et al*., Nat. Commun. **8**, 1919 (2017).
[154] T. Hiroi *et al*., J. Phys. Soc. Jpn. **84**, 024723 (2015).
[155] Y. C. Chan *et al*., Phys. Rev. B **97**, 104509 (2018).
[156] H. Sakai *et al*., J. Phys. Soc. Jpn. **83**, 014709 (2014).
[157] Y. Seto *et al*., High-Pressure Science and Technology **20**, 269 (2010), (in Japanese).
[158] A. Yamashita *et al*., Sci. Rep. **11**, 230 (2021).
[159] M. Ochi *et al*., J. Phys. Soc. Jpn. **85**, 094705 (2016).
[160] E. H. Brandt, Phys. Rev. B **60**, 11939 (1999).
[161] M. Abdel-Hafiez *et al*., Phys. Rev. **B** 88, 174512 (2013).
[162] O. Pavlosiuk et al., Sci. Rep. **6**, 18797 (2016).
[163] Z. Hou, *et al*., Appl. Phys. Lett. **107**, 202103 (2015).
[164] Y. Ma *et al*., Europhys. Lett. **138**, 36003 (2022).
[165] H. Hayasaka and Y. Fuseya, J. Phys.: Condens. Matter **32**, 16LT01 (2020).
[166] Q. Liu *et al*., Phys. Rev. B **91**, 235204 (2015).
[167] D. A. Shirley, Phys. Rev. B **5**, 4709 (1972).
[168] A. Proctor and P. M. A. Sherwood, Anal. Chem. **54**, 13 (1982).
[169] J. E. Hirsch and F. Marsiglio, Nature **596**, E9 (2021).
[170] J. P. Perdew, K. Burke, and M. Ernzerhof, *Phys. Rev. Lett.* **77**, 3865 (1996).
[171] G. Kresse and D. Joubert, *Phys. Rev. B* **59**, 1758 (1999).
[172] G. Kresse and J. Hafner, *Phys. Rev. B* **47**, 558 (1993).
[173] G. Kresse and J. Hafner, *Phys. Rev. B* **49**, 14251 (1994).
[174] G. Kresse and J. Furthmüller, *Comput. Mater. Sci.* **6**, 15 (1996).
[175] G. Kresse and J. Furthmüller, *Phys. Rev. B* **54**, 11169 (1996).

[176] Y. Mizuguchi *et al*., *Sci. Rep.* **5**, 14968 (2015).

13.2. References in Japanese (参考文献)

(1) 柳瀬陽一、物性研究、**97**, 824 (2012).

(2) 柳瀬陽一、固体物理、**49**, 109 (2014).

(3) 中村康晴、博士論文 (2017).

(4) 木村憲章、固体物理、**47**, 593 (2012).

(5) 藤本聡、LTM センター誌、**11**, 10 (2007).

(6) 柳瀬陽一、固体物理、**47**, 607 (2012).

(7) 柳瀬陽一、播磨尚朝、**46**, 229 (2011).

(8) 柳瀬陽一、播磨尚朝、**47**, 101 (2012).

(9) 松田裕司、物性研究、**4**, 044205 (2015).

(10)芝内孝禎、物性研究、**97**, 875 (2012).

(11)橘高俊一郎、物性研究、**6**, 85 (2017).

(12)長岡洋介、日本物理学会誌、**51**, 7 (1996).

(13)小布施英明、日本物理学会誌、**70**, 14 (2015).

(14)早坂太志、博士論文 (2020).

(15)Jeongchun Ryu、博士論文 (2019).

14. Publication lists

14.1. Papers as the first author

Papers (0), (I), (II), and (III) are during my Ph.D. degree (from Apr. 2020 to Mar. 2023). Papers (IV) and (V) are during the course from bachelor to master (from Apr. 2018 to Mar. 2020). Chapter 8 is related to (II) and (III). Chapter 10 is related to (I). Chapter 11 is related to (II) and (IV). Chapter 9 is related to (0) (This paper is under review by JPSJ., so I show preprint).

(0) **K. Hoshi**, H. Arima, N. Kataoka, M. Ochi, A. Yamashita, A. de Visser, T. Yokoya, K. Kuroki and Y. Mizuguchi, arXiv:2211.00843 (2022).

(I) **K. Hoshi**, R. Kurihara, Y. Goto, M. Tokunaga and Y. Mizuguchi, Sci. Rep. **12**, 288 (2022).

(II) **K. Hoshi** and Y. Mizuguchi, J. Phys.: Condens. Matter **33**, 473001 (2021).

(III) **K. Hoshi**, S. Sakuragi, T. Yajima, Y. Goto, A. Miura, C. Moriyoshi, Y. Kuroiwa, and Y. Mizuguchi, Condens. Matter. **5**, 81 (2020).

(IV) **K. Hoshi**, M. Kimata, Y. Goto, T. D. Matsuda, and Y. Mizuguchi, J. Phys. Soc. Jpn. **88**, 033704 (2019).

(V) **K. Hoshi**, Y. Goto, and Y. Mizuguchi, Phys. Rev. B. **97**, 094509 (2018).

14.2. Papers as the coauthor

(I) R. Kiyama, **K. Hoshi**, Y. Goto, M. Nagao and Y. Mizuguchi, J. Phys. Commun. **6**, 055009 (2022).

(II) T. Mitobe, **K. Hoshi**, M. R. Kasem, R. Kiyama, H. Usui, A. Yamashita, R. Higashinaka, T. D. Matsuda, Y. Aoki, T. Katase, Y. Goto and Y. Mizuguchi, Sci. Rep. **11**, 22885 (2021).

(III) R. Kiyama, **K. Hoshi**, Y. Goto, and Y. Mizuguchi, Phys. Status. Solidi RRL 2000546 (2021).

(IV) A. Yamashita, H. Usui, **K. Hoshi**, Y. Goto, K. Kuroki, and Y. Mizuguchi, Sci. Rep. **11**, 230 (2021).

(V) R. Kiyama, Y. Goto, **K. Hoshi**, R. Jha, A. Miura, C. Moriyoshi, Y. Kuroiwa, T. D. Matsuda, Y. Aoki, and Yoshikazu Mizuguchi, J. Phys. Soc. Jpn. **89**, 064702 (2020).

15. Acknowledgment

I am incredibly grateful to my supervisor, Dr. Mizuguchi, for his invaluable advice and continuous support since I started studying in his group. His knowledge and experience have encouraged me in all the time of my research and daily life. I would also like to thank Dr. Goto, Dr. Jha, Dr. Yamashita, Dr. Nakahira, and Dr. Arima for their experimental support and discussion of my study. I also thank all the members of Mizuguchi's group. It is their kind help and support that have made me study.

Additionally, I would like to express gratitude to collaborators Dr. Kimata and Sudo for the support and physics discussion in high-field and two-axes rotator experiments at IMR, Tohoku University, since I was a master's degree student. I also would like to thank Dr. Tokunaga and Dr. Kurihara for their support and physics discussion in pulsed-field measurements at ISSP, University of Tokyo. I would like to thank Dr. Kuroiwa (Hiroshima University), Dr. Moriyoshi (Hiroshima University), and Dr. Miura (Hokkaido University) for their experimental support in synchrotron XRD at SPring-8. Moreover, I would like to thank Dr. Yajima and Dr. Sakuragi for their experimental support in low-temperature XRD at ISSP, University of Tokyo. I greatly appreciate Dr. Nagao's experimental support in PPMS with the rotator system at University of Yamanashi. I am also grateful to Dr. Kuroki (Osaka university) and Dr. Ochi (Osaka university) for their theoretical calculations and discussion. I would like to thank Dr. Yokoya (Okayama University) and Kataoka (Okayama University) for the ARPES measurements and discussion.

Moreover, I would like to express my sincere gratitude to Dr. Visser for his experimental support at the University of Amsterdam. I also thank lab mates Lorenz and Salis in Visser's group for their experimental support. Their friendship and support have made my stay in Amsterdam valuable.

Finally, I would like to express my gratitude to my parents. Without their tremendous understanding and encouragement over the past few years, it would be impossible for me to complete my study.

16. Appendix

16.1. Electronic band structures

Electronic band structures for $LaO_{0.5}F_{0.5}BiS_{2-y}Se_y$ were investigated by collaborative work: the band calculations were performed by Dr. Ochi (Osaka University) and Dr. Kuroki (Osaka University) and ARPES measurements by Kataoka (Okayama University) and Dr. Yokoya (Okayama University), respectively. I briefly introduce these methods here. The results of electronic band structures are displayed in Section 9.5.

We performed first-principles band-structure calculation based on the density functional theory with the Perdew-Burke-Ernzerhof parametrization of the generalized gradient approximation [170] and the projector augmented wave (PAW) method [171] as implemented in the Vienna *ab initio* simulation package [172-175]. We used the experimental crystal structures determined by our experiment [176]. To represent the $O_{0.5}F_{0.5}$ occupation in $LaO_{0.5}F_{0.5}BiS_2$ and $LaO_{0.5}F_{0.5}BiSSe$, one oxygen and one fluorine atom are placed in a 10-atom unit cell. For simplicity, we assumed that selenium atoms occupy in-plane chalcogen sites in $LaO_{0.5}F_{0.5}BiSSe$. The core electrons in the PAW potential were [Kr]$4d^{10}$ for La, [He] for O and F, [Xe]$4f^{14}5d^{10}$ for Bi, [Ne] for S, and [Ar]$3d^{10}$ for Se, respectively. The spin-orbit coupling was included. We took 500 eV of the cutoff energy for the wave function, a 14×14×4 *k*-mesh, and 0.15 eV of the Gaussian smearing width.

ARPES measurements were performed at BL-9A in the Hiroshima Synchrotron Radiation Center (HiSOR) using a R4000 electron analyzer (Scienta Omicron) with *p*-polarized light. The total energy resolution was set to approximately 30 meV for $h\nu$ = 30 eV. All samples were cleaved *in-situ* on the (001) plane in an ultrahigh vacuum of less than 5×10^{-9} Pa. All the measurements were performed at the same temperature of 13 K. The binding energies of the samples were determined by referencing the Fermi energy (E_F) of gold electronically contacted with samples.

16.2. Characteristic physical parameters

I summarized several physical parameters in Table 16.1. First, lower critical fields B_{c1} are estimated from the *M-H* curves [see Figs. 16.1(a–c)]. We need to correct the observed values by considering the demagnetization effect. Thus, B_{c1} is evaluated from the following relation

$$B_{c1} = \frac{B_a}{1-N}. \tag{16.1}$$

B_a is estimated as the fields which deviate from the linear M (H) (Note that I estimated the B_a as the minimum values of the magnetization for $LaO_{0.5}F_{0.5}BiS_{1.61}Se_{0.39}$). The demagnetization factor N has already been summarized in Table 9.1. Figures 16.1(d–f) show the temperature dependence of the corrected B_{c1}. Furthermore, B_{c1} (0) is estimated from the formula $B_{c1}(T) = B_{c1}(0)[1-(T/T_c)^2]$

[solid black curves in Fig. 16.1(d–f)]. Magnetic penetration depth is evaluated from the B_{c1} (0) by the following formula

$$B_{c1} = \frac{\Phi_0}{4\pi\lambda_\parallel} \ln\left(\frac{\lambda_\parallel}{\xi_\parallel}\right). \quad (16.2)$$

The in-plane coherence lengths are necessary for estimating magnetic penetration depth. The in-plane coherence length $\xi_\parallel$ can be evaluated from out-of-plane upper critical fields by Eq. 3.7. The in-plane coherence length $\xi_\parallel$ for $LaO_{0.5}F_{0.5}BiS_{2-y}Se_y$ (y = 0.22, 0.69) are shown in Chapter 10. I also measured the out-of-plane upper critical fields for $LaO_{0.5}F_{0.5}BiS_{1.14}Se_{0.86}$ and $LaO_{0.8}F_{0.2}BiSSe$ (nominal values) by resistivity measurements under magnetic fields [see Figs. 16.2(a) and (b)]. Figures 16.2(c) and (d) show the temperature dependence of the out-of-plane upper critical fields for $LaO_{0.5}F_{0.5}BiS_{1.14}Se_{0.86}$ and $LaO_{0.8}F_{0.2}BiSSe$, respectively. The in-plane coherence lengths are estimated by the B_{c2} (T) slope (all-data points). The obtained values of lower critical fields and magnetic penetration depth are almost consistent with the previous studies [64]. I also summarized the GL parameter $\kappa = \lambda_\parallel(0)/\xi_\parallel(0)$ in Table 16.1. The values κ vastly exceed $1/\sqrt{2}$, indicating that the $BiCh_2$-based compounds are typical type II superconductors. The mean free path can be obtained from the relation

$$\ell = \frac{\hbar k_F}{\rho_0 n e^2}. \quad (16.3)$$

The residual resistivity ρ_0 is defined as the values at T = 5 K in this study. Carrier density n is obtained from the Hall coefficient (see Chapter 9). I also used the values n at T = 5 K for estimating the mean free path. Assuming a single cylindrical Fermi surface, the Fermi wave vector k_F can be written as the formula $k_F = \sqrt{2\pi nc}$, where c is the lattice constant and has already been displayed in Chapter 8. The obtained $\ell_\parallel$ is smaller than the $\xi_\parallel$ (see Table 16.1), implying that the $BiCh_2$-based superconductors are in the dirty limit. The dirty superconductivity in the doping level of x = 0.5 may support the fully gapped *s*-wave or extended *s*-wave state with accidental nodes. Bulk physical properties measurements may observe fully gapped *s*-wave behavior under the dirty superconductivity even when the extended *s*-wave state is realized.

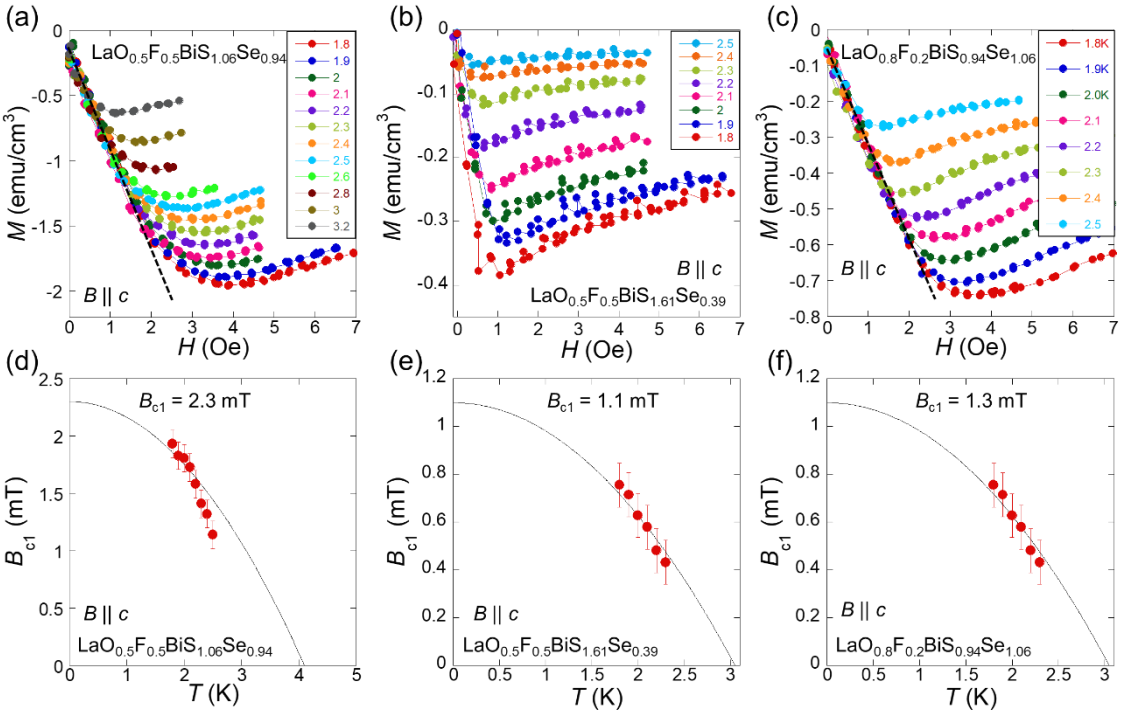

Fig. 16.1. (a–c) Zero-field-cooled M-H curves for (a) $LaO_{0.5}F_{0.5}BiS_{1.06}Se_{0.94}$, (b) $LaO_{0.5}F_{0.5}BiS_{1.61}Se_{0.39}$, and (c) $LaO_{0.8}F_{0.2}BiS_{0.94}Se_{1.06}$. Applied magnetic fields are parallel to the *c*-axis direction. The dashed lines are visual guides. (d–f) Temperature dependence of the lower critical fields for (a) $LaO_{0.5}F_{0.5}BiS_{1.06}Se_{0.94}$, (b) $LaO_{0.5}F_{0.5}BiS_{1.61}Se_{0.39}$, and (c) $LaO_{0.8}F_{0.2}BiS_{0.94}Se_{1.06}$. The solid lines represent the formula $B_{c1}(T) = B_{c1}(0)[1-(T/T_c)^2]$. The Se concentration is estimated from the EDX.

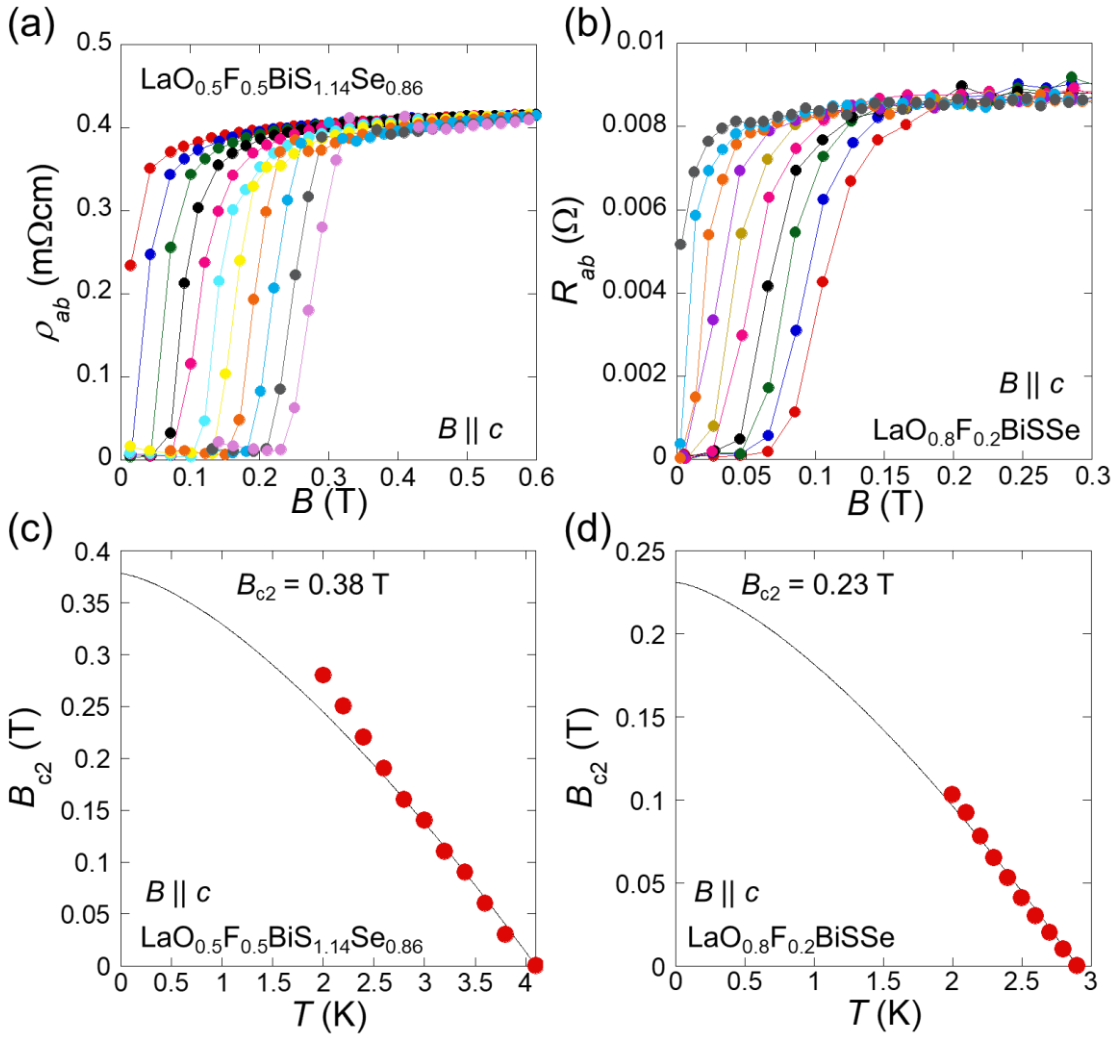

Fig. 16.2. (a–b) Temperature dependence of the resistivity under magnetic fields parallel to the *c*-axis direction for (a) $LaO_{0.5}F_{0.5}BiS_{1.14}Se_{0.86}$ and (b) $LaO_{0.8}F_{0.2}BiSSe$ (Se concentration is nominal value). (c–d) Temperature dependence of the out-of-plane upper critical fields for (a) $LaO_{0.5}F_{0.5}BiS_{1.14}Se_{0.86}$ and (b) $LaO_{0.8}F_{0.2}BiSSe$. The solid lines represent the WHH curves.

Table 16.1. Characteristic parameters of $BiCh_2$-based superconductors $LaO_{1-x}F_xBiS_{2-y}Se_y$.

Parameters	$LaO_{0.5}F_{0.5}BiSSe$	$LaO_{0.5}F_{0.5}BiS_{1.5}Se_{0.5}$	$LaO_{0.8}F_{0.2}BiSSe$
$B_{c1}^{\perp}(0)$ [mT]	2.3 (y = 0.94, #1)	1.1 (y = 0.39, #I)	1.3 (y = 1.06, #A)
$\lambda_{\parallel}(0)$ [nm]	458 (y = 0.94, #1)	714 (y = 0.39, #I)	590 (y = 1.06, #A)
$B_{c2}^{\perp}(0)$ [T]	0.38 (y = 0.86, #2)	0.40[a] (y = 0.22, #II)	0.23 (nominal, #B)
$\xi_{\parallel}(0)$ [nm]	25 (y = 0.86, #2)	24[a] (y = 0.22, #II)	31 (nominal, #B)
κ_{GL}	19	30	19
B_c (mT)	17	11	10
ρ_{ab}(5 K) [mΩcm]	0.46 (y = 0.91, #3)	1.9 (y = 0.39, #III)	0.46 (y = 0.94, #C)
R_H (5 K) [10^{-3}cm^3/C]	12 (y = 0.91, #3)	19 (y = 0.44, #IV)	3.1 (y = 1.05, #D)
n (5 K) [10^{21}cm^{-3}]	0.52 (y = 0.91, #3)	0.33 (y = 0.44, #IV)	2.0 (y = 1.05, #D)
μ (5 K)[cm^2/Vs]	26	9.7	6.8
$\ell_{\parallel}$ [nm]	3.6	1.1	1.9

(a) Nominal Se concentration is 0.25.

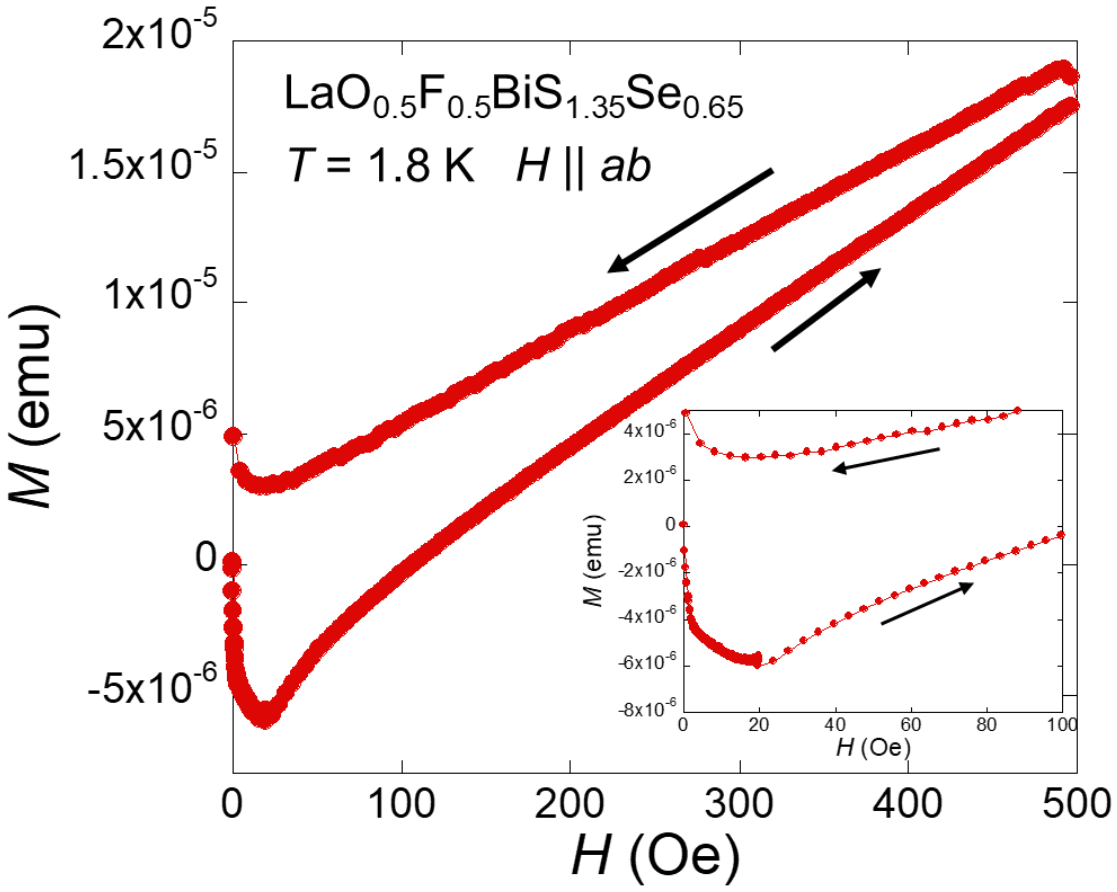

Fig. 16.3. *M-H* curve in the low-field region at T = 1.8 K for $LaO_{0.5}F_{0.5}BiS_{1.35}Se_{0.65}$. Applied magnetic fields are parallel to the *ab* plane. The inset shows the enlarged figure around the lower-field region.

16.3.Low-temperature resistivity

I investigate the temperature dependence of the resistivity by several models. The $T^{-1/2}$ or $1/\ln T$ [119] dependence of the resistivity has been reported in the weak-localization states at low temperatures. Hence, I display the low-temperature (from 50 K to 10 K) resistivity as functions of $T^{-1/2}$ and $1/\ln T$ in Figs. 16.4 (a–f). The regions, which are close to the dashed lines, possibly indicate the localization states. In addition, we can confirm that the $T^{-1/2}$ or $1/\ln T$ increases in resistivity are suppressed by Se substitution. Moreover, the low-temperature (from 50 K to 10 K) resistivity for the nonmetallic behavior follows variable range hopping (VRH) in wide temperature regions [see Figs. 16.4 (g–i)], which implies the presence of disorder. The VRH behavior is also suppressed by Se substitution, which is consistent with previous crystal-structural analysis suggesting that local disorder in the Ch1 sites was suppressed by Se substitution [31].

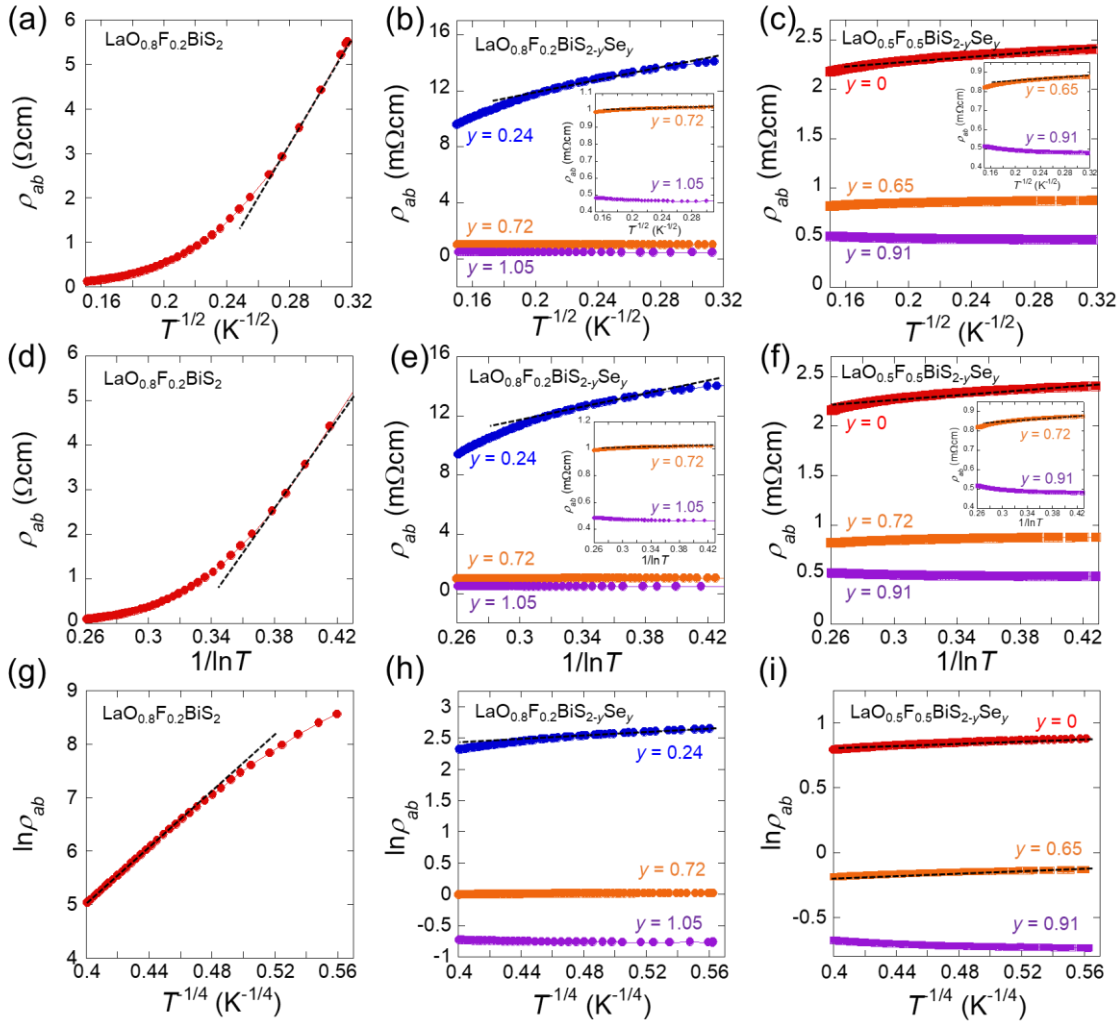

Fig. 16.4. Low-temperature resistivity (from 50 K to 10 K) ρ_{ab} as a function of $T^{-1/2}$ for (a) $LaO_{0.8}F_{0.2}BiS_2$ (red circles) (b) $LaO_{0.8}F_{0.2}BiS_{2-y}Se_y$ [y = 0.24 (blue circles), 0.72 (orange circles), and 1.05 (purple circles)] and (c) $LaO_{0.5}F_{0.5}BiS_{2-y}Se_y$ [y = 0 (red squares), 0.65 (orange squares), and 0.91 (purple squares)]. (d–f) ρ_{ab} vs. 1/ln$T$ for (a) $LaO_{0.8}F_{0.2}BiS_2$ (red circles) (b) $LaO_{0.8}F_{0.2}BiS_{2-y}Se_y$ [y = 0.24 (blue circles), 0.72 (orange circles), and 1.05 (purple circles)] and (c) $LaO_{0.5}F_{0.5}BiS_{2-y}Se_y$ [y = 0 (red squares), 0.65 (orange squares), and 0.91 (purple squares)]. The dashed lines are visual guides. lnρ_{ab} as a function of $T^{-1/4}$ for (g) $LaO_{0.8}F_{0.2}BiS_2$ (red circles) (h) $LaO_{0.8}F_{0.2}BiS_{2-y}Se_y$ [y = 0.24 (blue circles), 0.72 (orange circles), and 1.05 (purple circles)] and (i) $LaO_{0.5}F_{0.5}BiS_{2-y}Se_y$ [y = 0 (red squares), 0.65 (orange squares), and 0.91 (purple squares)]. The dashed lines are visual guides.

16.4.References to the history of superconductors

I have summarized the references to the history of superconductors (see Figs. 1.1 and 3.1) in Table 16.2.

Table 16.2. Reference to the history of superconductors.

Material	year	T_c	B_{c2}/T_c or B_0/T_c (*ab*-plane or *a*-axis direction, or polycrystalline)	B_{c2}/T_c (*b*-axis direction)	B_{c2}/T_c (*c*-axis direction)	Reference
Hg	1911	4.1	0.01			伊原　英雄、戸叶　一正、「超伝導材料」、東京大学出版会、(1987).
Nb	1937	9.25	0.02227027027			伊原　英雄、戸叶　一正、「超伝導材料」、東京大学出版会、(1987).
Nb_3Sn	1954	18	1.611111111			伊原　英雄、戸叶　一正、「超伝導材料」、東京大学出版会、(1987).
NbTi	1983	9.2	1.576086957			M. Lubell, IEEE Trans. Magn., **19**, 754 (1983).
MgB_2	2002	39	0.4722222222		0.09722222222	J. Nagamatsu et al., Nature **410**, 63 (2001). L. Lyard *et al*., Phys. Rev. B **66**, 180502 (2002).
$La_{2-x}Sr_xCuO_4$ (La214)	1986	38	3.289473684		0.6315789474	「高温超伝導体データブック」、応用物理学会　超伝導分科会、(2009).
$YBa_2Cu_3O_{7-\delta}$ (YBCO)	1987	93	3.76344086		0.7741935484	「高温超伝導体データブック」、応用物理学会　超伝導分科会、(2009).
$Bi_2Sr_2CaCu_2O_8$ (BSCCO)	1988	85	6.270588235		0.2588235294	「高温超伝導体データブック」、応用物理学会　超伝導分科会、(2009).
Hg-Ba-Ca-Cu-O	1993	130				A. Schilling *et al*., Nature **363**, 56 (1993).
Sr_2RuO_4	1994	0.93				Y. Maeno *et al*., Nature **372**, 532 (1994).
$LaO_{1-x}F_xFeAs$	2008	26				Y. Kamihara et al., J. Am. Chem. Soc. **130**, 3296 (2008).
$SmO_{1-x}F_xFeAs$	2009	42	2.380952381		1.19047619	H-S. Lee *et al*., Phys. Rev. B **80**, 144512 (2009).
$SmO_{1-x}F_xFeAs$	2008	55				Ren Zhi-An *et al*., Chinese Phys. Lett. **25**, 2215 (2008).
$Gd_{1-x}Th_xOFeAs$	2008	56				C. Wang *et al*., EPL **83**, 67006 (2008).
$Ba_{1-x}K_xFe_2As_2$	2009	38.5	4.805194805		2.311688312	D. L. Sun *et al*., Phys. Rev. B **80**, 144515 (2009).
FeSe	2013	9.9	3.434343434		2.929292929	S. I. Vedeneev *et al*., Phys. Rev. B **87**, 134512 (2013).
MoS_2	2016	6.5	8		0.7692307692	Y. Saito *et al*., Nat. Phys. **12**, 144 (2016).
$NeSe_2$	2016	3	10.5		0.5797101449	X. Xi *et al*., Nat. Phys. **12**, 139 (2016).
UGe_2	2000	0.8	1.75	3	6	D. Aoki and J. Flouquet, J. Phys. Soc. Jpn. **81**, 011003 (2012). D. Aoki et al., J. Phys. Soc. Jpn. **88**, 022001 (2019).
URhGe	2001	0.26	9.615384615	53.84615385	2.692307692	D. Aoki and J. Flouquet, J. Phys. Soc. Jpn. **81**, 011003 (2012).
UCoGe	2007	0.7	42.85714286	25.71428571	0.8571428571	D. Aoki and J. Flouquet, J. Phys. Soc. Jpn. **81**, 011003 (2012).
UTe_2	2019	1.6	4.0625	21.875	6.875	S. Ran *et al*., Science **365**, 684 (2019).
$CePt_3Si$	2004	0.75	4		4	E. Bauer, M. Sigrist, Eds., Non-Centrosymmetric Superconductors: Introduction and Overview, vol. 847 of Lecture Notes in Physics (Springer-Verlag, 2012).
$CeRhSi_3$	2005	1.09	6.880733945		27.52293578	E. Bauer, M. Sigrist, Eds., Non-Centrosymmetric Superconductors: Introduction and Overview, vol. 847 of Lecture Notes in Physics (Springer-Verlag, 2012).
$CeRh_2As_2$	2021	0.26	7.307692308		53.84615385	S. Kim *et al*., Science **373**, 1012 (2021).
H_3S	2015	203	0.4467005076			A. P. Drozdov *et al*., Nature **525**, 73 (2015).
LaH_{10}	2017	250	0.544			A. P. Drozdov *et al*., Nature **569**, 528 (2019).
$Bi_4O_4S_3$	2012	6				Y. Mizuguchi *et al*., Phys. Rev. B **86**, 220510 (2012).
$LaO_{1-x}F_xBiS_2$ (HP)	2012	10.6				Y. Mizuguchi *et al*., J. Phys. Soc. Jpn. **81**, 114725 (2012).
$NdO_{1-x}F_xBiS_2$	2013	5.2				S. Demura *et al*., J. Phys. Soc. Jpn. **82**, 033708 (2013).